ELECTROPHORETIC DEPOSITION OF TiO_2 AND $SrTiO_3$ NANOPARTICLES AS PHOTO-ELECTROCATALYST FOR WATER SPLITTING

PHOON BAO LEE

INSTITUTE OF GRADUATE STUDIES
UNIVERSITY OF MALAYA
KUALA LUMPUR

2018

ELECTROPHORETIC DEPOSITION OF TiO_2 AND $SrTiO_3$ NANOPARTICLES AS PHOTO-ELECTROCATALYST FOR WATER SPLITTING

PHOON BAO LEE

DISSERTATION SUBMITTED IN FULFILMENT OF THE REQUIREMENTS FOR THE DEGREE OF MASTER OF PHILOSOPHY

INSTITUTE OF GRADUATE STUDIES
UNIVERSITY OF MALAYA
KUALA LUMPUR

2018

UNIVERSITY OF MALAYA
ORIGINAL LITERARY WORK DECLARATION

Name of Candidate: PHOON BAO LEE

Matric No: HGA150013

Name of Degree: MASTER OF PHILOSOPHY

Title of Thesis: ELECTROPHORETIC DEPOSITION OF TiO_2 AND $SrTiO_3$ NANOPARTICLES AS PHOTO-ELECTROCATALYST FOR WATER SPLITTING.

Field of Study: CHEMISTRY (Material Chemistry)

I do solemnly and sincerely declare that:

(1) I am the sole author/writer of this Work;
(2) This Work is original;
(3) Any use of any work in which copyright exists was done by way of fair dealing and for permitted purposes and any excerpt or extract from, or reference to or reproduction of any copyright work has been disclosed expressly and sufficiently and the title of the Work and its authorship have been acknowledged in this Work;
(4) I do not have any actual knowledge nor do I ought reasonably to know that the making of this work constitutes an infringement of any copyright work;
(5) I hereby assign all and every rights in the copyright to this Work to the University of Malaya (―UM”), who henceforth shall be owner of the copyright in this Work and that any reproduction or use in any form or by any means whatsoever is prohibited without the written consent of UM having been first had and obtained;
(6) I am fully aware that if in the course of making this Work I have infringed any copyright whether intentionally or otherwise, I may be subject to legal action or any other action as may be determined by UM.

Candidate‘s Signature Date:

Subscribed and solemnly declared before,

Witness‘s Signature Date:

Name:

Designation:

ELECTROPHORETIC DEPOSITION OF TiO_2 AND $SrTiO_3$ NANOPARTICLES AS PHOTO-ELECTROCATALYST FOR WATER SPLITTING

ABSTRACT

Fossil fuels are currently the most economical sources for H_2 production. Nonetheless, these processes would cause greenhouse gases (GHG) emission that may lead to certain environmental issues such as climate change and global warming. Photocatalytic water splitting was commonly used for H_2 production but the efficiency tends to be low. This main issue is the dispersion of powdered photocatalyst during the photocatalysis reaction which will cause (i) lower yield due to backward reaction of the intermediates, (ii) poor optical response due to the light scattering effects, and (iii) poor reusability due to the post-filtration. In this study, the photocatalyst was coated on a thin film for photoelectrochemical (PEC) water splitting under UV light irradiation. The TiO_2 was successfully and uniformly coated on fluorine doped tin oxide (FTO) glass by electrophoretic deposition (EPD) technique. The effect of several parameters such as deposition voltage, time, and post heat treatment temperature have been studied in order to produce a high smoothness TiO_2 layer for better PEC performance. The EPD technique is capable for tuning the smoothness and thickness of TiO_2. From FESEM image, the nanocrystalline TiO_2 with the film thickness of 14.6 µm gives a good uniformity and minimal cracking surface. The optimum condition to form TiO_2 thin film is 30 V, 60 s, and heat treatment at 400 ^{o}C. This film exhibited the highest hydrogen production rate and photoconversion efficiency (PCE) of 0.40 mL cm^{-2} h^{-1} and 2.49%, respectively. This demonstrated that the EPD technique is very promising to be used to coat TiO_2 on FTO glass for PEC water splitting. In the case of perovskite $SrTiO_3$, the morphology of $SrTiO_3$ nanoparticle was significantly influenced by the hydrothermal temperature. The best photocatalytic activity of $SrTiO_3$ in PEC performance was synthesised at 150 ^{o}C. This is due to uniform particle size, shape, and large specific surface area. By fabricating the $SrTiO_3$ on the thin films using EPD technique, the optimum condition was found to be 40 V and 120 s. Based on the FESEM image, $SrTiO_3$ film with the thickness of 18.8 μm exhibited the highest photocurrent density of 1.05 mA/cm^2. The immobilised $SrTiO_3$ is capable for generating 0.25 mL cm^{-2} h^{-1} of H_2 and the PCE was found to be 1.28% under UV light irradiation. It is interesting to observe that the efficiency of TiO_2 was much better than that of $SrTiO_3$. The plausible reasons were as follows, (i) the specific surface area of TiO_2 is 3.3 times larger, and (ii) the particle size of TiO_2 is 2 times smaller as compared to that of $SrTiO_3$.

Keywords: Hydrogen; strontium titanate; titanium dioxide; photoelectrochemical; water splitting

ENAPAN ELEKTROFORESIS ZARAH-NANO TiO_2 DAN $SrTiO_3$ SEBAGAI PEMANGKIN ELEKTRO-FOTO UNTUK PENGASINGAN MOLEKUL AIR

ABSTRAK

Pada masa ini bahan bakar fosil merupakan sumber yang paling ekonomik untuk menghasilkan H_2. Namun begitu, proses ini akan menyebabkan pelepasan gas rumah hijau (GHG) yang akan membawa isu-isu alam sekitar seperti perubahan iklim dan pemanasan global. Pengasingan molekul air fotopemangkin lazim digunakan untuk menghasilkan H_2 tetapi keberkesanan pemangkin masih lagi di tahap yang rendah. Ini adalah berpunca daripada (i) serakan serbuk fotopemangkin ke dalam elektrolit menyebabkan beberapa kekurangan seperti tindak balas balikan perantara yang akan mengeluarkan hasil yang lebih rendah, (ii) kesan penyebaran cahaya yang boleh menurunkan tindak balas optik, dan (iii) penapisan selepas eksperimen juga diperlukan. Dalam kajian ini, pengasingan molekul air fotoelektrokimia (PEC) telah digunakan bagi melumpuhkan fotomangkin pada kaca fluorin terdop timah oksida (FTO) dengan cara enapan elektroforesis (EPD) supaya tipisan nipis yang seragam dapat dihasilkan. Kajian ini bertujuan untuk mengoptimumkan beberapa parameter bagi menghasilkan lapisan salutan TiO_2 dengan kelicinan yang tinggi supaya ianya dapat meningkatkan prestasi PEC di bawah sinaran UV. Dalam kajian ini, cirian tipisan nipis TiO_2 boleh dikawal melalui EPD termasuk kelicinan dan ketebalan. Pencirian melalui FESEM telah menujukkan bahawa tipisan nipis TiO_2 dengan ketebalan 14.6 μm memberikan keseragaman yang baik dan keretakan pada permukaan yang minimum. Tipisan nipis ini juga mempamerkan ketumpatan fotoarus tertinggi (2.12 mA/cm^2). Didapati bahawa keadaan optimum untuk membentuk tipisan nipis TiO_2 ialah 30 V, 60 s dan rawatan haba pada 400 ^oC berdasarkan cirian j_p-V di mana kadar penghasilan H_2 dan kecekapan penukaran foto (PCE) ialah 0.40 $mL\ cm^{-2}\ h^{-1}$ dan 2.49% masing-masing. Zarah nano $SrTiO_3$ disediakan melalui tindak balas hidroterma pada suhu yang berbeza (60 sehingga 180 ^{o}C). Morfologi perovskit $SrTiO_3$ ternyata boleh dipengaruhi oleh suhu tindak balas hidroterma dan $SrTiO_3$ yang telah disintesis pada suhu 150 ^{o}C telah menunjukkan aktiviti fotopemangkin terbaik dalam prestasi PEC disebabkan oleh keseragaman saiz zarah, bentuk dan luas permukaan spesifik BET yang lebih tinggi. Kemudian, zarah nano $SrTiO_3$ telah berjaya dienapkan pada kaca FTO melalui EPD dan pengoptimuman dilakukan dengan mengkaji beberapa parameter. Melalui pembikinan tipisan nipis menggunakan EPD, keadaan optimum yang didapati adalah 40 V dan 120 s berdasarkan cirian j_p-V. Mengikut hasil penilaian dari FESEM, tipisan nipis $SrTiO_3$ dengan ketebalan 18.8 μm menunjukkan kecekapan tertinggi. Dibawah penyinaran UV (100 mW/cm^2), didapati penghasilan H_2 dan PCE ialah 0.25 mL cm^{-2} h^{-1} dan 1.28% masing-masing. Kedua-dua fotoelektrod TiO_2 dan $SrTiO_3$ boleh digunakan semula untuk pengasingan molekul air secara berterusan sebanyak lima kali kitaran. Selain itu, keberkesanan TiO_2 didapati lebih baik berbanding $SrTiO_3$ di dalam kajian ini. Oleh yang demikian, kesimpulan kajian ini yang dicadangkan adalah (i) keluasan permukaan tertentu TiO_2 lebih besar dan (ii) saiz zarah TiO_2 juga lebih kecil jika dibandingkan dengan $SrTiO_3$.

Kata kunci: Hidrogen; strontium titanat; titanium dioksida; fotoelektrokimia; pengasingan molekul air

ACKNOWLEDGEMENTS

First, I would like to thank University of Malaya (UM) and also Nanotechnology and Catalysis Research Centre (NANOCAT) for offering me an opportunity and providing a conducive research environment with sufficient facilities to complete my research project.

Secondly, I would like to express my deep and sincere gratitude to my supervisors, Associate Prof. Dr. Juan Joon Ching and Ir. Dr. Lai Chin Wei for giving precious advice, excellent guidance and provided a good basis for the present thesis to complete for my research project. Their wide knowledge and logical way of thinking also have been of great value for me.

In addition, my appreciation also goes to all the technical staff in various laboratories that aided me throughout my work. They offered me their generosity and technical support whenever I faced difficulties with the using of machines and equipment. In my daily work, I have been blessed with a group of friendly and helpful postgraduate colleagues especially Dr. Pan, Dr. Morris Lee, Rashid, Izazi, Azimah, Kung Shiuh, Henry Soo, Leann Oi, Alex Choo, Foo Wah, You Sing and Tong Shien. With their valuable suggestions, discussions, and helping, I was able to run the experiment smoothly and produce quality works.

Last but not least, I want to thank my family for the love and support given throughout my studies. My mother and father are my mentors, both in work and life. Their endless love is a constant source of encouragement for me to overcome all the difficulties that arises on the road to success.

TABLE OF CONTENTS

LIST OF FIGURES

LIST OF TABLES

LIST OF SYMBOLS AND ABBREVIATIONS

% : Per cent

> : Greater than

≥ : Greater or equal to

^{o} : Degree

Å : Angstrom

α : Alpha

Ag : Silver

AgCl : Silver chloride

Al : Aluminium

aq : Aqueous (state)

Ar : Argon

Au : Gold

β : Beta

BET : Brunauer–Emmett–Teller

C : Carbon

ca. : Circa (approximately)

CB : Conduction band

CdS : Cadmium sulphide

CE : Counter electrode

CH_3OH : Methanol

CH_4 : Methane

cm^{-1} : Wavenumber

cm : Centimetre

cm^2 : Centimetre square

cm^3	:	Centimetre cube
CO	:	Carbon monoxide
CO_2	:	Carbon dioxide
CO_3^{2-}	:	Carbonate (ion)
COS	:	Carbonyl sulphide
Cr	:	Chromium
Cu	:	Copper
^{o}C	:	Degree Celsius
DC	:	Direct current
ΔE	:	Energy difference for the electron transition
e^-	:	Electron
EDX	:	Energy dispersive X-ray
EDL	:	Electrical double layer
e.g.	:	For example
E_g	:	Band gap energy
EIS	:	Electrochemical impedance spectroscopy
EPD	:	Electrophoretic deposition
etc.	:	et cetera
et al.	:	and others
eV	:	Electronvolt
Fe	:	Iron
Fe_2O_3	:	Iron (III) oxide
FESEM	:	Field emission scanning electron microscopy
FF	:	Fossil fuels
FTO	:	Fluorine doped tin oxide
GHG	:	Greenhouse gases

GT : Gigatonnes

g : Gaseous (state)

g : Gram (in mass)

GJ : Gigajoule

ΔH : Heat of enthalpy

H^+ : Proton

H : Hydrogen (atom)

H_2 : Hydrogen (molecule)

h^+ : holes

h : Hour (time)

$h\nu$: Photon

H_2S : Hydrogen sulphide

IPA : Isopropyl alcohol

IR : Infrared

ITO : Indium doped tin oxide

JCPDS : Joint Committee on Powder Diffraction Standards

K : Kelvin

kcal : Kilocalorie

KCl : Potassium chloride

kHz : Kilohertz

kJ : Kilojoule

KOH : Potassium hydroxide

K_{sp} : Solubility product constant

kV : Kilovolts

kX : Magnification

λ : Wavelength

l : Liquid (state)

LSV : Linear sweep voltammetry

M : Molarity

mA : Milliampere

Mg : Magnesium

$Mg(NO_3)_2.6H_2O$: Magnesium nitrate hexahydrate

min : Minute (time)

MJ : Megajoule

mm : Millimetre

mol : Mole

mL : Millilitre

MPa : Megapascal

MSR : Molten state reaction

mV : Millivolt

mW : Milliwatt

n/a : Not available

N_2 : Nitrogen

nA : Nanoampere

NaOH : Sodium hydroxide

Na_2SO_4 : Sodium sulphate

NH_3 : Ammonia

NHE : Normal hydrogen electrode

Ni : Nickel

nm : Nanometres

NO_x : Nitrogen oxides

O : Oxygen (atom)

O_2 : Oxygen (molecule)

OCP : Open circuit potential

ω : Rotational speed

PCE : Photoconversion efficiency

Pd : Palladium

PEC : Photoelectrochemical

PET Polyethylene terephthalate

pH : Potential hydrogen

PL : Photoluminescence

Pt : Platinum

PV : Photovoltaic

RE : Reference electrode

RES : Renewable energy system

RF : Radio frequency

rpm : Revolutions per minute

s^{-1} : Hertz

s : Solid (state)

s : Second (time)

Se : Selenium

SHE : Standard hydrogen electrode

SMR : Steam methane reforming

SnO_2 : Tin oxide

SO_2 : Sulphur dioxide

Sr^{2+} : Strontium (ion)

Sr : Strontium

$SrCO_3$: Strontium carbonate

$Sr(OH)_2.8H_2O$: Strontium hydroxide octahydrate

$SrTiO_3$: Strontium titanate

SSR : Solid state reaction

STE : Self-trapped-electrons

θ : Theta

Ti : Titanium

TiO_2 : Titanium (IV) oxide

μm : Micrometre

US : United States

UV : Ultraviolet

UV-DRS : Ultraviolet-visible diffuse reflectance spectroscopy

V : Voltage

VB : Valence band

vs. : Versus

W : Watt

WE : Working electrode

XRD : X-ray diffraction

ZnO : Zinc oxide

ZnS : Zinc sulphide

ZP : Zeta potential

LIST OF APPENDICES

CHAPTER 1: INTRODUCTION

1.1 Hydrogen market and demand

The worldwide energy consumption is projected to double by mid-century due to the economic growth and population. Fossil fuels, FF (*e.g.* coal, crude oil, and natural gas) are very important in the global energy development, providing all the energy for daily life, transportation, agriculture as well as for industry. Nonetheless, FF are non-renewable energy resources. It must be retrieved from the earth through environmentally questionable drilling and mining practices, and are distributed unevenly across the globe. According to BP statistical review of world energy, the energy consumption is dominated (85.5%) by non-renewable energy in 2015 (Dudley, 2015) such as natural gas, coal, and petroleum as presented in Figure 1.1.

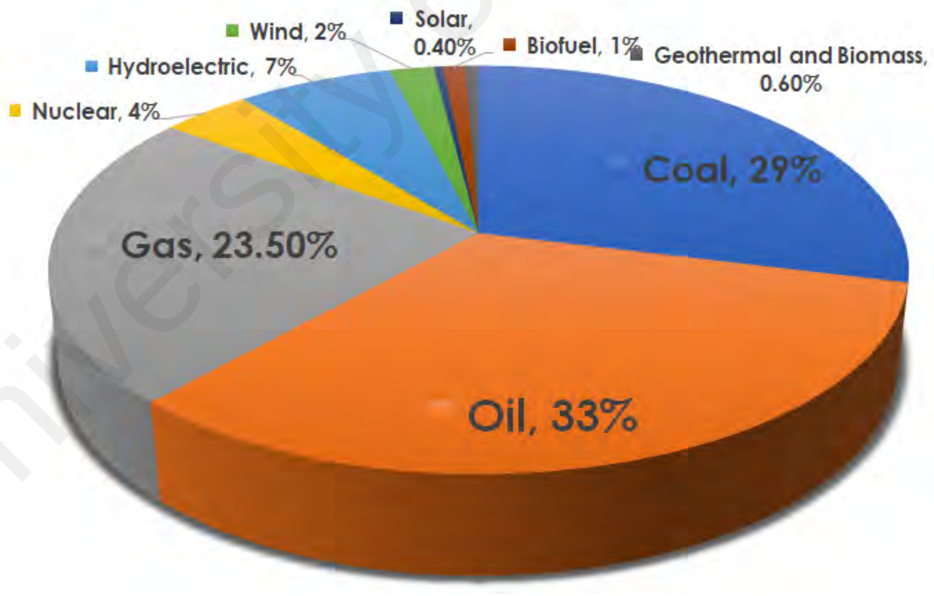

Figure 1.1: The consumption of energy over the world in 2015 (Dudley, 2015).

Overconsumption and excessive exploitation of FF arise from the prompt growth of economy around the world and on-going rise population of the world that will lead to a shortage of energy resources in the near future (Pimentel *et al.*, 1999). It was estimated that the world‘s energy demand will be heightened by 50% in 2030 (Umbach, 2010). By following the current rate of crude oil consumption, the world oil reserves will last only for 40 to 50 years (Olah, 2005), and the global coal output was predicted will reach the peak in about 2042 to 2062 (Maggio & Cacciola, 2012). Therefore, these will require scientists to develop innovative approaches towards creating carbon-neutral fuels. On top of that, the use of FF raises some environmental concerns. The exhaust gases produced (*e.g.* automobile and coal power plant) from the combustion of FF, such as CO_2, SO_2, and NO_x results in acid rain and may lead to global warming. The greenhouse effect resulting in global warming phenomena and thus the atmosphere temperature is rising. Global warming also happens when greenhouse gases (GHG) collect in the atmosphere so that to absorb solar irradiation and sunlight that has reflected to the surface of the earth, especially CO_2. These GHG are able to last up to several centuries on the earth surface and warm the planet by trapping the heat, which known as the greenhouse effect. The greenhouse effect is 2.7 times stronger than past 40 years (Nikolov & Zeller, 2017). It was reported that CO_2 emissions due to the burning of FF are around 29 GT per year (Maggio & Cacciola, 2012). According to Ghicov and Schmuki, environmental destruction such as ozone layer depletion, global warming, and ocean acidification has become a worldwide problem (Ghicov & Schmuki, 2009). All the inhabitants will eventually extinct if the problem prolonged due to the climate and weather changes of the planet. Owing to the long term uncertainties of environmental CO_2 capturing, air pollution, climate change, and risk of energy shortage, some initiatives has been done for researchers to obtain renewable energy system (RES) to replace FF for decades (Momeni & Ghayeb, 2015b; Steinfeld, 2002; Turn, Kinoshita, Zhang, Ishimura, & Zhou, 1998).

The lightest molecule in the universe is hydrogen, H_2 (2.02 g/mol), with the highest combustion of heat (141.8 kJ/g) and attracting technological and scientific interest as a primary energy carrier and potential to use for transportation fuel (Lubitz & Tumas, 2007). The H_2 combustion with supplying of O_2 in air produces water, which is environmental friendly. H_2 can be presented as an alternate energy to the conventional hydrocarbon fuels but only with the realization of an appropriate source (Esswein & Nocera, 2007). Nevertheless, H_2 is not a primary fuel as it does not naturally occur in large amount. Two key components are necessary in order to produce H_2 fuel, which are H atoms and energy.

To date, the major technique for H_2 generation that used in the industry is hydrocarbon feedstock steam reforming (SMR) has been a favoured method used to produce H_2 in a large scale for several decades (Navarro, Pena, & Fierro, 2007; Rostrup-Nielsen, Sehested, & Nørskov, 2002). Nonetheless, H_2 production by SMR method considered as non-renewable sources that the H_2 is meant to replace. The GHG (CO_2) would evolve as a by-product in large amount in this process. It was found that approximately 0.1 GT of H_2 is generated every year for commercial and about 95% is derived from hydrocarbon fuels (Nikolaidis & Poullikkas, 2017). Commercially, renewable energy only contributes 5% of H_2 generation, mainly by electrolysis of water with the electrical power source that is renewable (Ni, Leung, Leung, & Sumathy, 2007). The high production cost of water electrolysis limits its use to the high purity H_2 production. Thus, some other techniques to generate H_2 from the source of renewable energies need to be considered. Besides that, the H atoms are found most often as part of many larger molecules, such as water. A water molecule contains only H and O atoms and thus it is free of carbon. Figure 1.2 shows some methods for H_2 production.

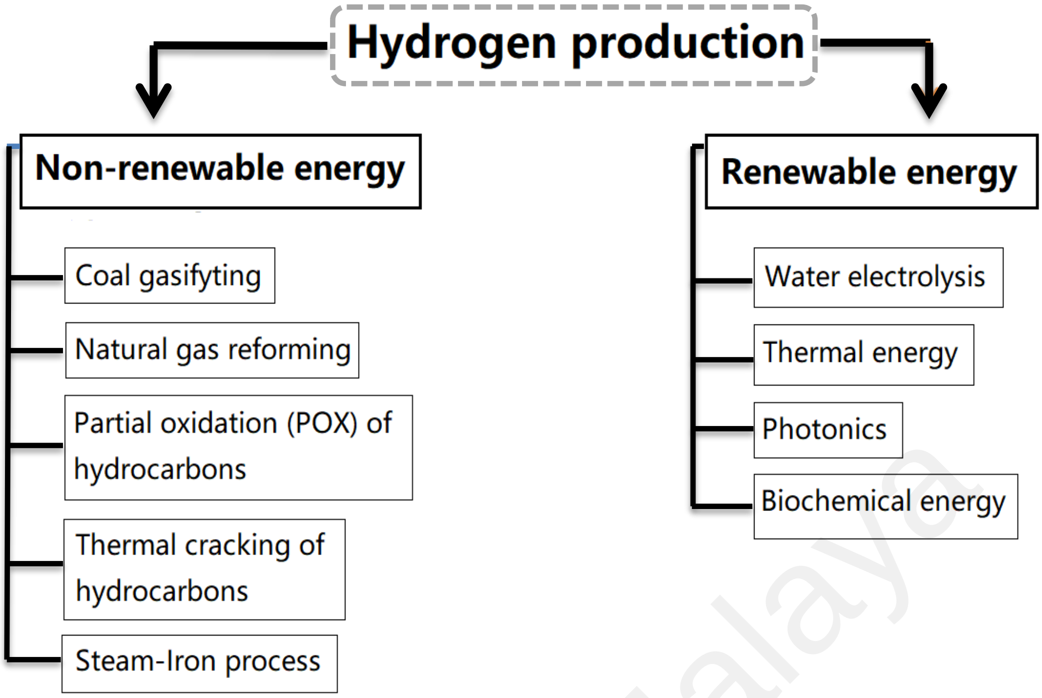

Figure 1.2: Overview of H_2 production methods.

Recently, great interest has focused on H_2 production by photolysis. Generally speaking, photolysis is achieved by two methods, which are photoelectrolysis using photoelectrochemical cells (PEC) (Momeni & Ghayeb, 2015b) and photolysis using colloidal suspensions of powdered catalysts (Liu, Chen, Li, & Zhang, 2006), such as TiO_2 and some other ceramic powders. The most outstanding advantage for PEC cells is the relatively high efficiency because the photogenerated h^+ and e^- are isolated spatially to two different electrodes, which decreases the possibility of charge carrier recombination. Meanwhile, the two yield gases, H_2 and O_2 are also generated at different electrodes that able to minimise the backward reaction of the intermediates and unstable chemical species. As a result, PEC water splitting becomes a promising method for H_2 production because H_2 with its environmental friendliness and high energy capacity could be obtained from renewable and clean energy such as light and water. The general term for the process of PEC water splitting is a chemical reaction of separating water into O_2 and H_2 by utilising a semiconductor photocatalyst to catalyse the reaction. PEC water splitting is a hybrid system that used to produce PV electricity and drives the process of water electrolysis (Phoon *et al.*, 2017). It contains a phase of electrolyte that ions bring along the charge for moving, whereas the interface of electrolyte/electrode for electrochemical reactions to take place. Under light illumination, two phenomena occur: (i) photocatalysis in which optical energy provides activation energy for the reaction to occur (Equation 1.1), and (ii) photoelectrolysis whereby optical energy converted to chemical energy (Equation 1.2 & Equation 1.3) as presented below (Kudo & Miseki, 2009):

$$\text{Semiconductor} \xrightarrow{\text{hv>Eg}} \text{Semiconductor}\ (e^- + h^+) \qquad \text{(Equation 1.1)}$$

$$2\ H_2O\ (l) + 4\ h^+ \rightarrow O_2\ (g) + 4\ H^+ \qquad \text{(Equation 1.2)}$$

$$2\ H^+ + 2\ e^- \rightarrow H_2\ (g) \qquad \text{(Equation 1.3)}$$

The idea of water splitting process by photochemical that using TiO_2 photoelectrode was successfully discovered by Fujishima and Honda in 1972 (Fujishima & Honda, 1972). After that, TiO_2 has been attracted many scientific interests and widespread used as a photoelectrode in PEC water splitting. TiO_2 possess many unique properties that are hardly found in other semiconducting materials such as ZnO, ZnS, and CdS. The advantages include low production cost, exceptional photocorrosion resistance, non-toxic and strong photocatalytic activity with the E_g of 3.00 eV on the rutile phase and 3.20 eV on the anatase phase. $SrTiO_3$ photocatalyst has become great attention recently. It is a typical multi-metal oxide (perovskite type) and the E_g is 3.20 eV. Moreover, $SrTiO_3$ has distinctive physical properties (ferroelectricity, piezoelectricity, as well as high dielectric constants) and chemical property (photocatalysis).

1.2 Problem Statement

Water splitting by photolysis has been broadly studied as one of the promising methods for renewable H_2 production. The reason main attributed to the cost-effective because it only requires abundance sources, light, water, and semiconductor.

Nevertheless, much work has focused on the limitations of powdered photocatalysts, for example, (i) lower yield due to the backward reaction of intermediates, (ii) poor optical response due to the light scattering effects, and (iii) poor reusability due to the post-filtration. It was known that the structuring or coating of the powdered nanoparticles on a solid surface such as film will enhance the horizontal degree of light distribution by scattering of light. The scattering of light is maximum in particle suspensions due to it can take place at both the back and front sides of the nanoparticles. However, by direct reflection from a flat surface, the _trapped‘ light would be lost otherwise (Osterloh, 2013).

Therefore, there is a need to study the effectiveness of powdered photocatalyst such as TiO_2 and $SrTiO_3$ after coated as a thin film on a conductive substrate. Among the coating techniques, electrophoretic deposition (EPD) will be used to coat the photocatalyst on a FTO glass in order to improve the efficiency of PEC water splitting. Due to the simplicity of EPD technique, it is a promising coating technique for powered samples and thus it has been widely used in different applications. Furthermore, it able to form a uniform and high smoothness surface as compared to other methods of coatings such as paste and dip coating. Therefore, EPD technique is expected to be able to minimise the nanoparticles light scattering which will improve electrons transferring ability.

1.3 Objectives of Research

In this study, the objectives are stated as follow:

- To synthesise and characterise the physicochemical properties of $SrTiO_3$ via hydrothermal synthesis.
- To study the effect of TiO_2 and $SrTiO_3$ after coated on FTO glass via EPD technique under different parameter such as deposition voltage, time and to understand the efficiency of PEC water splitting.

1.4 Outline of Research Work

In this research study, four sections were divided. **Stage I** involves photocatalyst preparation via the hydrothermal method to synthesise $SrTiO_3$ nanoparticles. The $SrTiO_3$ will was synthesised at different reaction temperatures to optimise the best condition for $SrTiO_3$ nanoparticles formation. **Stage II** involves photocatalyst coating as PEC water splitting photoelectrode. The TiO_2 and $SrTiO_3$ were coated on FTO glass by EPD technique. The TiO_2 and $SrTiO_3$ coating quality will be optimised by several parameters. In order to evaluate and examine the physicochemical properties, **Stage III** involves photocatalyst characterisation. The characterisation process was conducted and analysed with Field emission scanning electron microscope (FESEM) that incorporated with Electron diffractive X-ray (EDX), X-ray diffraction (XRD), Raman spectroscopy, Zeta potential (ZP), Brunner-Emmet-Teller (BET), Diffuse reflectance-ultraviolet visible spectroscopy (UV-DRS) and Photoluminescence (PL) spectroscopy. **Stage IV** involves PEC water splitting performance evaluation under UV illumination. The properties of the sample for PEC water splitting was characterised by a tri-electrodes configuration PEC water splitting cell. The performance was tested with linear sweep voltammetry (LSV), photoconversion efficiency (PCE), H_2 production rate, electrochemical impedance spectroscopy (EIS) and photocurrent response.

1.5 Thesis Overview

This thesis consisted of five (5) chapters accordingly. **Chapter 1** presents some brief motivations, problem statements, research objectives, an outline of the research work and finally thesis overview. **Chapter 2** involve background and information on PEC water splitting, comprehensive review on the synthesis methods of $SrTiO_3$ nanoparticles and finally the applications of TiO_2 and $SrTiO_3$ are presented. **Chapter 2** also highlights powdered photocatalyst coating methods with its advantages and disadvantages. **Chapter 3** contains the raw materials selection and specification, the method of preparing $SrTiO_3$ nanoparticles, the method of photocatalyst coating and its characterisation, and optimisation analysis employed in this research. The performance testing procedure and instruments used for PEC water splitting were discussed. **Chapter 4** discussed the experimental outcome and the discussions on the studies. This chapter was divided into two sections, the first sub-chapter of **Chapter 4** is regarding the formation TiO_2 photoelectrode by EPD method for PEC water splitting performance and its properties whereas another part of **Chapter 4** is to discuss the formations of $SrTiO_3$ nanoparticles by hydrothermal reaction, the formation of $SrTiO_3$ photoelectrode by EPD method for PEC water splitting performance and its properties. **Chapter 5** summaries the conclusion of this research included with some recommendation and suggestion for further research.

CHAPTER 2: LITERATURE REVIEW

2.1 Physicochemical Properties of Hydrogen

Hydrogen atom (chemical symbol H) is the simplest elements in the periodic table that located at group 1 and period 1. In the universe, H is the most plentiful element that indicating 75 mass percentage among all the matter (Iida & Krische, 2007). H_2 is a colourless gas with the lightest molecules in the universe (2.02 g/mol), with the supreme combustion of heat that around 141.8 kJ/g. The legendary Swiss alchemist Paracelsus (1493–1541) was the first person who described the hydrogen atom, however, it was not recognised as a discrete substance, and later by Robert Boyle in 1671. Hydrogen was identified as a distinct species about a century later. Until 1776, Henry Cavendish was reported in a paper entitled *"On factitious airs"*. Seven years later, Antoine Lavoisier, a scientist who proved that water was composed of O and H, was given the name of *"water maker"* to hydrogen. In 1783, Lavoisier was given a name from the ancient Greek words *hydro* ―water" and *genes* ―forming" to this new element. At the same time, the H_2 was first used in balloon ascents.

Chemically, H_2 is capable to undergo reaction with most of the elements in periodic table. H_2 is also a highly flammable element when O_2 is supplied. Besides that, the H_2 is relatively high in mass-related energy density. In fact, about 132.5 MJ of energy contains in a kg of H_2 that is approximately 2.5 times higher than the energy consisted in a kg of CH_4. To date, it was reported that approximately 0.1 GT of H_2 is produced commercially every year (Nikolaidis & Poullikkas, 2017). Most of the H_2 is used for industrial applications. Basically, the uses of H_2 can be divided into four categories (Ramachandran & Menon, 1998), which are (i) as a reactant in hydrogenation process, (ii) as an O_2 scavenger, (iii) as a cooling agent for electrical generators, and (iv) as a spacecraft engines fuel. H_2 can be reacted with hydrocarbons catalytically in various pathway in the petroleum industry (*e.g.* hydrocarbon cracking produces a high ratio of H/C and refined fuels with shorter chain). Besides that, the production of ammonia (Equation 2.1) by the Haber-Bosch process (Travis, 1993) and methyl alcohol (Equation 2.2) requires H_2 and others precursor to undergo reaction with provided catalyst at high temperatures and pressures. Moreover, H_2 can also use for oil and fat hydrogenation, fertiliser production, metallurgical application as well as for electronic industry.

$$\mathrm{CO + 2H_2 \overset{Cu}{\rightarrow} CH_3OH} \qquad \Delta \mathrm{H_{298\,K}} = -21.7\ \mathrm{kcal/mol} \qquad \text{(Equation 2.1)}$$

$$\mathrm{N_2 + 3H_2 \overset{Fe}{\rightarrow} 2NH_3} \qquad \text{(Equation 2.2)}$$

The flexible energy carrier, H_2, can be transported over long distances with minimal cost of transportation and stored in a variety of ways. In terms of smog reduction, H_2 is an ideal fuel when used electrochemically in a fuel cell rather than combusted. H_2 is a good efficient energy carrier with low polluting fuel, in which potentially to be used for generating the power in places that are facing difficulties to supply and consume electricity as well as for heating and transportation purposes. On top of that, H_2 in a fuel cell produces zero harmful emission, thus, it could be one of the most promising energy carriers in near future. From hand-held devices to portable generators, most of the portable application that typically uses batteries can also be power up by fuel cells. Furthermore, the personal vehicles, buses, trucks, and marine vessels can be power up by fuel cells as well as provide auxiliary power to traditional transportation technologies. As a result, in terms replacing the imported petroleum that currently use in personal transportation like cars and also trucks, H_2 can play a particularly important role in the future.

2.2 Hydrogen Production Method

H_2 is an element that widespread in the earth. It can be obtained from diverse resources. Until today, the global H_2 production is dominated by hydrocarbon fuels and SMR is the most significant contemporary technologies. Nevertheless, it was suggested that a feasible way to generate H_2 should approach the low-cost production of electricity from solar, wind or water resources (Bicakova & Straka, 2010). It is necessary to look for promising technologies, resources, and to assess the effectiveness of the H_2 production methods along with their impact on the environment. In general, the method of H_2 productions can be divided into two major categories, which are non-renewable energy and renewable energy. This section will further discuss its advantages, and disadvantages of those methods.

2.2.1 Non-renewable Energy

Basically, non-renewable energy refers to the fossil fuel (FF). Carbon is the main element in FF, namely, crude oil, natural gas, and coal that may take up to thousands of years to form naturally and it cannot be replaced as fast as they are being consumed. The production of H_2 by using FF may produce some carbon residue in the final product, especially CO_2. These by-product can give some environmental impact due to it is a kind of GHG emission. Therefore, to produce H_2 by FF should be associated with carbon capture system (CCS).

One of the most common methods for H_2 production by FF is SMR (Ogden, Steinbugler, & Kreutz, 1999). CH_4 reforming or natural gas is a mature production and advanced process that constructs upon the existing pipeline of natural gas delivery infrastructure. Currently, more than 90% of the H_2 was generated by SMR in large central plants in the US. For near-term production of H_2, SMR is a significant technology route and it involves two steps in production (Rostrup-Nielsen, 2001), which are (i) the raw material of hydrocarbon is fed in a tubular of the catalytic reactor by mixing with steam, to produce H_2 and CO by reaction of steam with methane (Equation 2.3), (ii) shifting of water-gas, a reaction of CO with steam to produce more H_2 and leave the CO_2 as by-product (Equation 2.4). Under this method of production, it was reported that the GHG emission rate was found to be 55 kg CO_2/GJ of natural gas fuel energy (Møller, Boldrin, & Christensen, 2009).

$CH_4\ (g) + H_2O\ (l) \rightarrow CO\ (g) + 3\ H_2O\ (l)$ (Equation 2.3)

$CO\ (g) + H_2O\ (l) \rightarrow CO_2\ (g) + H_2\ (g)$ (Equation 2.4)

For some commercial applications like automobile fuel cells, it was suggested the partial oxidation (POX) as well as the catalytic partial oxidation (CPOX) of hydrocarbons process for the production of H_2. The raw materials for gasification can be biogas and natural gas whose difficult for further utilisation and treatment that primarily heavy in oil fractions. POX is a process without using a catalyst, in which the raw material was gasify under supply of O_2 (Equation 2.5 and 2.6) or steam (Equation 2.7) at high temperatures (> 1000 ^{o}C) and pressures (3-8 MPa) whereas CPOX is an oxidation process that require catalyst such as Ni and the reaction temperatures (*ca.* 700 to 900 ^{o}C) is lower than POX. In comparison with SMR, more CO_2 is generated as by-product in POX (Bicakova & Straka, 2010). The gaseous mixture generated by POX contains H_2, CO_2, CO, water, CH_4, H_2S, and COS.

$CH_4\ (g) + O_2\ (g) \rightarrow CO\ (g) + 2\ H_2\ (g)$ (Equation 2.8)

$CH_4\ (g) + 2\ O_2\ (g) \rightarrow CO_2\ (g) + 2\ H_2O\ (l)$ (Equation 2.9)

$CH_4\ (g) + H_2O\ (l) \rightarrow CO\ (g) + 3\ H_2\ (g)$ (Equation 2.10)

In 2016, the countries that hold the largest proved reserves of the coal in the world was found to be US (26.6%), Russia (17.6%), and China (12.8%) (Hosseini & Wahid, 2016). Coal is a highly variable and complex substance that able to be transformed into a variety of products chemically. A considerable amount of electricity and H_2 could produce via coal gasification, this merely due to the huge size of coal deposits are available (Turner, 2004). Economically, to produce large quantities of H_2, coal gasification is a relatively inexpensive and often cited as one of the promising resources. Nonetheless, the energy required for the necessary sequestration of CO_2 would increase the rate at which coal reserves are depleted. The process of H_2 production is by reacting the coal with steam under the condition of O_2 supply, as well as high temperatures and pressures for the syngas formation (Equation 2.8), which is a mixture that consisting majority of H_2 yield, CO and a certain volume of the CO_2.

$$CH_{0.8}\,(s) + O_2\,(g) + H_2O\,(l) \rightarrow CO\,(g) + CO_2\,(g) + H_2\,(g) + \text{other species} \qquad \text{(Equation 2.8)}$$

2.2.2 Renewable Energy

Renewable energy is derived from natural processes that are replenished constantly. It derives directly from heat generated deep within the earth or from the sun such as the electricity and heat generated from hydropower, ocean, wind, solar, biofuels, biomass as well as geothermal resources, and also the derivation of H_2 from renewable sources. On top of that, renewable energy generates only a little or zero waste as by-products (*e.g.* chemical pollutants like CO_2). Therefore, renewable energy has a minimal environmental impact. Overall, it was found that four sustainable pathways to produce H_2, namely, electricity (Zeng & Zhang, 2010), thermal energy (Steinfeld, 2002), photonic energy (Momeni & Ghayeb, 2015b), and biochemical energy (Turn *et al.*, 1998) and Figure 2.1 shows the various energy driven water splitting routes.

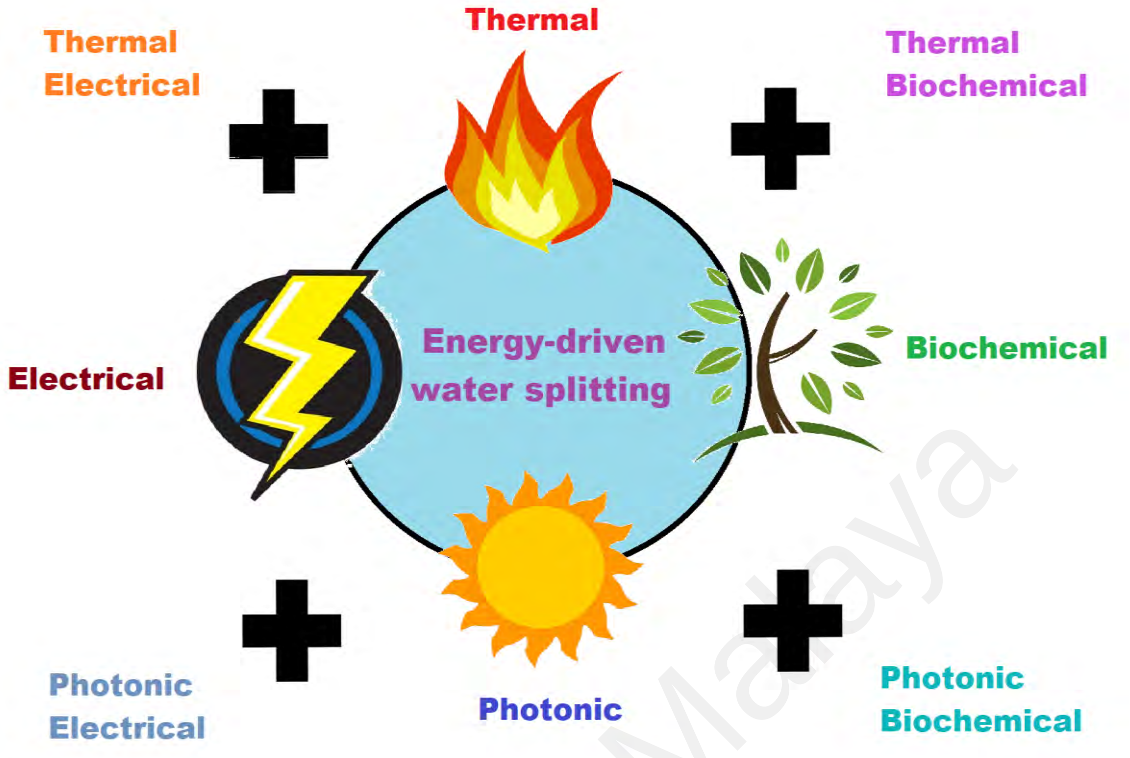

Figure 2.1: The routes of water splitting by using different renewable energy.

The electrolysis unit consisting dual-electrodes (a cathode and anode) that dipped in an electrolyte and connected through an external power supply. Water electrolysis technology has been introduced more than 200 years (Levie, 1999). The history of water electrolysis started as early as the first industrial revolution, in the year 1800, when Nicholson and Carlisle were the first to discover the ability of electrolytic water decomposition (Trasatti, 1999). Until today, several methods of water electrolysis were developed such as alkaline electrolysis (Nikolic *et al.*, 2010), proton exchange membrane water electrolysis (Linkous, Anderson, Kopitzke, & Nelson, 1998), as well as steam electrolysis (Mingyi, Bo, Jingming, & Jing, 2008). The electron flows from the anode of the DC power source to the positive terminal when the DC is applied to the electrolysis set up, where they consumed by H^+ to form H. For the process of water electrolysis, theoretically, the H^+ move towards the positive terminal, whereas the OH^-

move towards the negative terminal. Equation 2.9 shows the overall water electrolysis chemical reactions. The standard potential of the water decomposition is -1.229 V, which indicates that this process needs a potential difference of 1.229 V to decompose the water. Besides that, the electrolysis of water process requires only some simple equipment such as water, which is a negligible cost. However, the cost of electricity might be significant to the water electrolysis process (Hosseini & Wahid, 2016).

Cathode: $2\ H^+\ (aq) + 2\ e^- \rightarrow H_2\ (g)$ $(E^0 = 0.000\ V\ vs.\ SHE)$

Anode: $H_2O\ (l) \rightarrow 1/2\ O_2\ (g) + 2\ H^+\ (aq) + 2\ e^-$ $(E^0 = 1.229\ V\ vs.\ SHE)$

Overall: $H_2O\ (l) \rightarrow H_2\ (g) + 1/2\ O_2\ (g)$ $(E^0 = -1.229\ V\ vs.\ SHE)$

(Equation 2.9)

Thermal energy water splitting can be known as thermochemical processes. Thermochemical water splitting uses relatively high temperatures (500 to 2000 ^oC) and to activate a sort of chemical reactions that produce O_2 and H_2 from water. The thermal energy for decomposition of water was explored extensively in the 1970s due to the *"Energy Depot"* project was carried out in 1960s, which had as an objective the production of a fuel from earth, air, and water (Funk, 2001). Provided that the water dissociation process is reversible, the O_2 and H_2 are necessary to be separated effectively in order to minimise the possibility of O_2 and H_2 recombination. As the water thermolysis occurs at high temperature, catalysts are used in the thermochemical cycle to reduce the temperature (> 1200 K) for dissociation of water into O_2 and H_2 (Acar & Dincer, 2014). In general, the thermochemical water splitting process will be coupled with solar (Abanades & Flamant, 2006; Rao & Dey, 2017) or nuclear heat sources (Orhan, Dincer, & Rosen, 2008; Wu & Onuki, 2005). The highest temperature of the nuclear reactor was found to be approximately 1573 K (Perkins & Weimer, 2004).

Studies show that the molten salt cooled reactors (MSR), heavy metal cooled reactors (HMR), and high-temperature gas cooled reactors (HTGR) are the most suitable candidates to produce H_2 by thermochemical technology (Yildiz & Kazimi, 2006). Nuclear energy able to produce both electricity and H_2 and it can shift the production between the two. However, public antipathy towards nuclear power is still a significant political obstacle to increase the usage, especially in Europe countries (Carbonnier, 2016). For thermochemical water splitting that corporate with solar energy, the high temperature of solar is still challenging due to the installations of solar concentrators are in practice limited to the sun-belt regions or desert and it also needs a large space. Moreover, there are still facing some problems that need further discussions such as the continuous recovery of the intermediates and great complexity of kinetics of the reactions for the practical thermochemical cycle development for water decomposition process (Tee *et al.*, 2017).

To current, approximately 12% of the world energy supply is contributing by biomass (Smestad, 2009). Generally, municipal, industrial, animal and forestry wastes, aquatic crops, agricultural crops, industrial crops, woody energy crops, and herbaceous energy crops are potentially be used for the energy production (Ni, Leung, Leung, & Sumathy, 2006). For biochemical H_2 production, a fermentative conversion from carbohydrates can take place in a dark condition with assisted by a diverse group of the anaerobic bacterial. In the absence of O_2, the H_2 can be produced through an anaerobic process via dark fermentation as shown in the Equation 2.10. The fermentative production basically can be explained by the hydrolysis of organics enzymatically that in high molecular mass to a organics compound which is water soluble and followed by the H_2 production, as well as with the fatty acids and CO_2 as by-products (Azwar, Hussain, & Abdul-Wahab, 2014).

$C_6H_{12}O_6 + 2\ H_2O \rightarrow 2\ CH_3COOH + 2\ CO_2 + 4\ H_2$ (Equation 2.10)

To date, the H_2 production by biological methods is still at the research level. The method that uses microorganisms such as cyanobacteria and green microalgae to produce H_2 with combined the photonic and biochemical methods are known as a photobiological process. Photobiological H_2 production basically can be the direct and indirect pathway. The microorganisms break water molecules to become O_2 and H_2 under sunlight condition, and this the process of biophotolysis in direct pathway. By assisting with hydrogenase enzyme, H^+ that generated in the biophotolysis process will then further changed into H_2. Meanwhile, the microorganisms will capture the sunlight by photosynthesis and stored the carbohydrate in some form as the Equation 2.11 for an indirect pathway of biophotolysis. These stored carbohydrates will then later used to produce H_2 as Equation 2.12. Besides that, photofermentation is another kind of biophotolytic process which involved the solar energy capture and conversion and to degrade the carbohydrate into H_2 and CO_2 using photosynthetic bacteria.

$6\ CO_2 + 12\ H_2O + \text{solar} \rightarrow C_6H_{12}O_6 + 6\ O_2$ (Equation 2.11)

$C_6H_{12}O_6 + 12\ H_2O + \text{solar} \rightarrow 12\ H_2 + 6\ CO_2$ (Equation 2.12)

Photolysis of water involves to breakdown the water molecules to become O_2 and H_2 chemically using photonic energy. The water splitting process was known that it must require a potential difference of 1.229 eV, which is corresponding $\lambda = 1008$ nm. Theoretically, this indicates that the dissociation of water molecules can take place under IR region. In the other words, approximately 70% of the photons that solar-irradiated are allowed to drive the water decomposition process. To date, the low frequency of light radiation for photocatalytic water splitting gains attention and becomes important for improving its cost-effectiveness and efficiencies. Generally, photolysis process is achieved primarily by two methods, (i) photoelectrolysis using the PEC cells (Bard, 1982) and (ii) photolysis using colloidal suspensions of powdered catalysts, such as TiO_2 (Kraeutler & Bard, 1978; Schrauzer & Guth, 1977) and other ceramics powders (Reber & Meier, 1984). The most outstanding advantage for PEC cell is the relatively high efficiency because the photogenerated h^+ and e^- are isolated spatially into dual-electrodes, which decreases the possibility of charge carrier recombination. Meanwhile, the two gases, O_2 and H_2 are also produced in the different locations so that the back reaction of intermediate species can be diminished. Photolysis using powdered catalysts is considered a potential method to achieve water splitting in a scalable fashion. However, the most significant factor constraining their use is their low efficiency (Meda & Abbondanza, 2013).

2.3 PEC Water Splitting

Based on the H_2 production technologies that reviewed in the previous section, due to the simplicity and low-cost consideration, PEC water splitting system has been chosen to generate H_2 in this research. PEC water splitting is a method that can produce the H_2 directly without any emission of carbons. On top of that, this process requires only abundant resources such as water and light. Also, the efficiency increased for light-to-H_2 can reduce the intrinsic cost.

2.3.1 Historical Overview

The first work on semiconductor photocatalysis was reported by Becquerel in 1839 (Becquerel, 1839). Beccquerel was designed an AgCl electrode as the cathode and the setup was able to generate the electric fields and current under light irradiation. This breakthrough attracted researchers on the light energy capturing and converting the electrical energy as an alternative energy source. Then, Charles Fritts has demonstrated a photoelectric effect about half century later with approximately 1% efficiency through a developed material Se and Au for *pn* junction device (Fritts, 1883). In 1955, the ―Becquerel effect", was understood and the modern era of PEC was born with the pioneering work of Brattain and Garret of this PV phenomenon (Brattain & Garrett, 1955).

The new generation of PEC water splitting cell has emerged to challenge this dominance where the PV system is integrated with an electrolyser to produce a clean and portable H_2 energy carrier. This has led in essential while facing operation issue of PV system during night time and the period of bad weather as chemical fuel in the H_2 form by the storage of energy (Barreca *et al.*, 2011).

H_2 fuel stored within a fuel cell can be utilised as clean energy. It is available at all times and it can be converted into electrical energy efficiently. This cell is basically composed of a cheap and facile fabrication nanocrystalline material and together with other attractive properties like high flexibility and chemical stability in aqueous solution. In a PEC water splitting cell, these materials are expected to have high solar light irradiation to current response (Centi & Perathoner, 2009). The idea of PEC water splitting was first successfully reported by Fujishima and Honda in 1972 by using the photoelectrode for the system (Fujishima & Honda, 1972). It has dragged the subsequent interests in photocatalysis research by scientists and researchers from all over the world on TiO_2 and made TiO_2 as an important component in many practical applications. In 1973, such work arose a substantial research effort into PEC cells for water splitting and it was given a greater impetus with the oil crisis.

2.3.2 Basic Principle

In the past decade, so far, the water splitting technology only meets 3.9% of the world‘s H_2 demand (Ewan & Allen, 2005). PEC water splitting is a hybrid system that used to generate electricity by PV and drives the process of water electrolysis that only needs simple equipment such as semiconductor, light, and water. PEC cell consists of a phase of electrolyte that the moving charge is carried by ions whereas electrochemical reactions occur at the interface of electrolyte/electrode (Archer, 2002). PEC cell also requires a semiconductor, which acts as a photocatalyst that irradiated light (*e.g.* sunlight, visible or UV) with the energy equivalent or larger to the semiconductor band gap. The illustrated the process of PEC water splitting was shown in Figure 2.2. The conversion of the solar energy to chemical energy is a thermodynamically reversible process. It was known that the potential (E^o) to split the water molecules to H_2 and O_2 is -1.229 V. Based on the Equation 2.13, by substituting the values, the Gibbs free energy is positive (237.178 kJ/mol) at standard ambient pressure and temperature. As a result, water splitting is a non-spontaneous process. In order to drive the water splitting reaction to take place, the electrical and light energy equivalents with the change in Gibbs free energy.

$$\Delta G^o = -\mathrm{nF}\Delta E^o_{cell} \qquad \text{(Equation 2.13)}$$

where ΔG^o and ΔE^o_{cell} are the standard change of Gibbs free energy and standard electric potential of the reaction, F is Faraday constant (96500 C/mol), and n represents the moles of electrons transferred in the reaction.

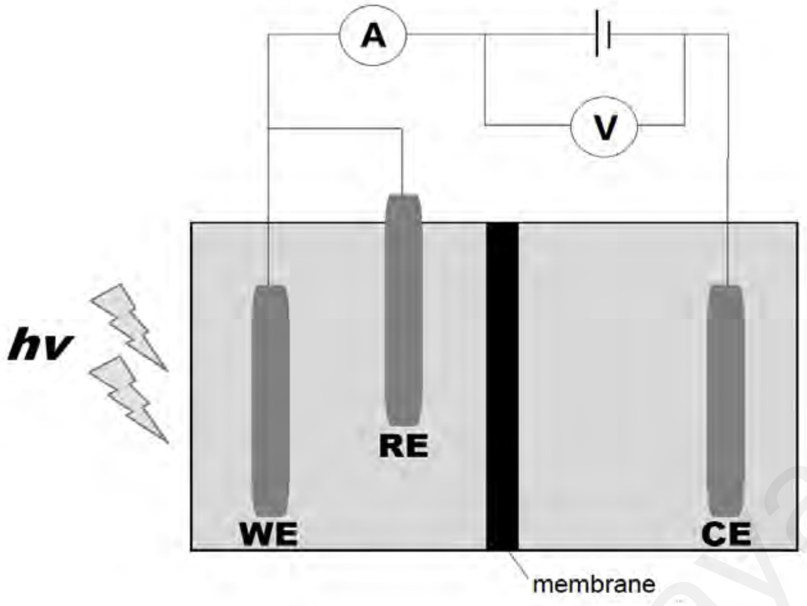

Figure 2.2: Schematic diagram of PEC water splitting process.

The PEC water splitting is a redox process. Under the light penetration, the photocatalyst of PEC cell will absorb the light energy and the charge separation occurs at the VB and CB (Equation 2.14). The h^+ are produced at the VB whereas the photoexcited e^- are located in the CB. The h^+ that located at VB trigger the oxidation process of water molecules (Equation 2.15) while the e^- that photoexcited at CB will undergo reduction process by reducing the protons to H_2 (Equation 2.16) (Kudo & Miseki, 2009).

Semiconductor + 2 $hv \rightarrow$ Semiconductor + 2 h^+ + 2 e^- (Equation 2.14)

$2\ H_2O\ (l) + 4\ h^+ \rightarrow O_2\ (g) + 4\ H^+$ (Equation 2.15)

$2\ H^+ + 2\ e^- \rightarrow H_2\ (g)$ (Equation 2.16)

The process of PEC water splitting usually proceeds by addition of acids or alkaline in the electrolyte phase due to the water itself does not have a good ionic conductivity. The additive in the aqueous medium offers a high mobility and concentration of H^+ and

OH^- that gives a lower electrical resistance. In this case, NaOH and KOH are the preferred electrolytes due to both of these alkaline gives better conductivities (Grimes, Varghese, & Ranjan, 2008). Due to the electrode corrosion issue, the acid electrolyte was usually seldom considered (Grimes *et al.*, 2008).

The semiconductor photoelectrode must be immersed in the electrolyte, which contains a couple of redox process. Depends on the PEC cell reaction and setting, the semiconductors can be applied as a photoanode as well as the photocathode. The overall reaction of PEC water splitting takes place at two different electrodes simultaneously, which are the WE and CE. The potential that required for breaking the water molecules is being provided by illuminating the electrode, either the WE or CE (Ikeda, Itani, Nango, & Matsumura, 2004). For RE, it plays a role to measure the potential of the WE without passing the current through. Semiconductor generally can be differentiating as p-type or n-type, depending on the electrons in the lattice structure. Figure 2.3 shows the principle of PEC water decomposition of an n-type semiconductor. For p-types semiconductors, CE undergo oxidation process to produce O_2 and WE undergoes reduction process to produce H_2. However, for n-type semiconductors, it is vice versa (Equation 2.17) (Grimes *et al.*, 2008).

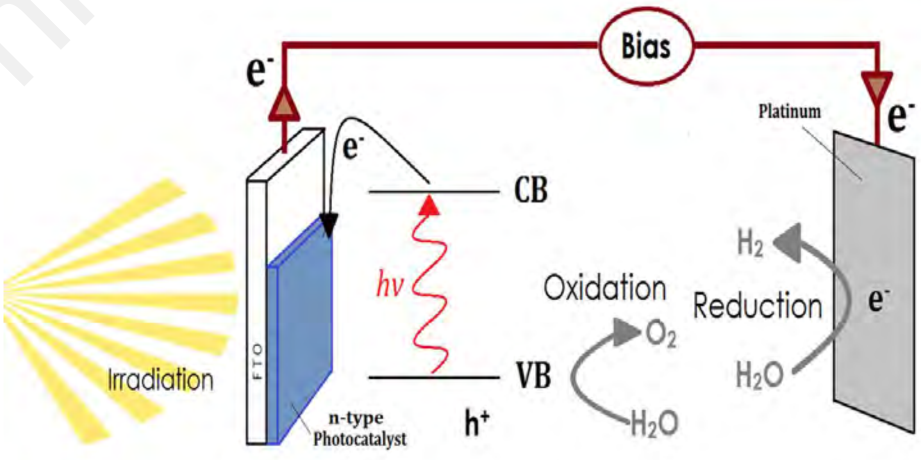

Figure 2.3: The principle of PEC water splitting n-type semiconductor.

Semiconductor that is n-type,

WE: $H_2O + h^+ \rightarrow 2\,H^+ + 1/2\,O_2$

CE: $2\,H^+ + 2\,e^- \rightarrow H_2$ (Equation 2.17)

2.4 Materials selection for PEC Water Splitting

In order to make the water splitting process function well, a suitable semiconductor should have a band gap of at least 1.229 eV with no photocorrosion (Jafari *et al.*, 2016). A small particle size and high crystallinity are desired to reduce the possibility of photogenerated h^+ and e^- recombination. A few decades ago, metal oxides have been applied as the photocatalyst for water splitting. Perovskite materials gaining attention to apply for PEC water splitting as a catalyst nowadays. The VB is lying at a more positive position than the water oxidation potential to form O_2, whereas for the CB is more negative than the water reduction potential to form H_2 when a semiconductor photocatalyst is applied for water splitting process. Figure 2.4 summarise the band structure of different types of photocatalyst with respect to the water splitting redox potentials.

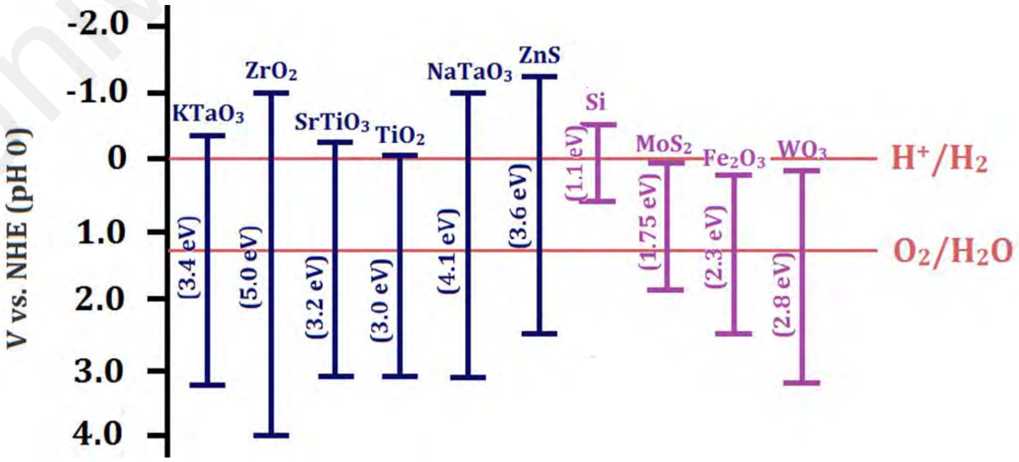

Figure 2.4: The band structure of different type of semiconductor.

Furthermore, Table 2.1 lists the value of VB, CB, E_g and λ of different semiconductors. To be a sustainable candidate as a photocatalyst for H_2 production, it must have the following two basic criteria, namely, (i) stability against photocorrosion in aqueous (Moniz, Shevlin, Martin, Guo, & Tang, 2015), (ii) sensitivity towards the light (Misra & Raja, 2010), and (iii) migration of photoexcited charge carrier with minimal recombination within the materials or losses when transferring from photoanode to the CE for high efficient H_2 generation (Grimes *et al.*, 2008).

Table 2.1: The VB and CB values of different semiconductors.

Semiconductor	Band energy with respect to NHE (eV)			λ (nm)	Reference
	VB	CB	E_g		
TiO_2 (Anatase)	2.95	-0.25	3.20	387.50	(Burnside, Moser, Brooks, Grätzel, & Cahen, 1999)
TiO_2 (Rutile)	2.95	-0.05	3.00	413.33	
$SrTiO_3$	2.59	-0.61	3.20	387.50	
ZnS	2.44	-0.91	3.35	370.15	(Zhang, Yu, Zhang, Li, & Gong, 2011)
SiC	2.34	-0.46	2.80	442.86	(Chiu & Li, 2009)
GaP	1.23	-0.97	2.20	563.64	(Kudo & Miseki, 2009)
CdSe	1.16	-0.54	1.70	729.41	(Kudo & Miseki, 2009)
GaN	3.00	0.50	3.50	354.29	(Gorczyca, Suski, Christensen, & Svane, 2010)
$BaTiO_3$	3.85	0.55	3.30	375.75	(Xu & Schoonen, 2000)
$FeTiO_3$	2.90	0.10	2.80	442.86	
$CuTiO_3$	3.18	0.19	3.00	413.33	
$KTaO_3$	3.02	-0.48	3.50	354.29	
$CdFe_2O_4$	2.85	0.55	2.30	539.14	
ZrO_2	4.25	-0.75	5.00	248.00	
Cu_2O	2.36	0.16	2.20	563.64	
SnO_2	3.69	0.19	3.50	354.29	
MoS_2	1.40	0.23	1.20	1033.33	
Fe_2O_3	2.93	0.73	2.20	563.64	
CdO	2.94	0.74	2.20	563.64	
CdS	1.88	-0.52	2.40	516.67	
WO_3	3.41	0.71	2.70	459.26	
Ta_2O_5	3.94	-0.06	4.00	310.00	
In_2O_3	2.63	-0.17	2.80	442.86	
CuO	2.66	0.96	1.70	729.41	

2.4.1 Titanium Dioxide (TiO_2)

2.4.1.1 Properties

A naturally occurring oxide of titanium was known as titanium (IV) oxide, TiO_2, (also known as titania or titanium dioxide). Due to its tuneable electronic energy band gap, environmentally friendly nature, low-cost, and chemical stability consideration, TiO_2 has been widely studied in many applications such as photocatalytic since the previous century.

As listed in Table 2.2, TiO_2 exhibited in three main forms of crystal that are anatase, rutile, and brookite. Both brookite and anatase are metastable and are readily transformed to rutile by annealing whereas rutile is a stable polymorph. The structure of brookite is composed of octahedral, each with corners located with O atoms and a Ti atom located at its centre. Brookite type TiO_2 has an orthorhombic crystal structure and the photocatalytic properties seldom studied by researchers due to difficult to synthesise in the laboratory (Deng *et al.*, 2008). Nonetheless, the pure brookite has demonstrated to be an interesting compound in photocatalytic applications and therefore the interest to study brookite has increased in recent years (Bellardita, Di Paola, Megna, & Palmisano, 2017; Vequizo *et al.*, 2017).

Table 2.2: The polymorph of TiO_2.

Properties	Anatase	Rutile	Brookite
Unit cell	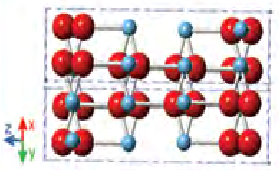	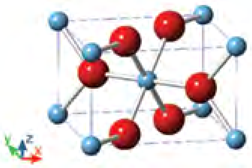	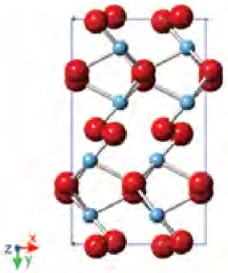
Crystal structure	Tetragonal	Tetragonal	Orthorhombic
Lattice constant (Å)	$a = b = 3.784$ $c = 9.515$	$a = b = 4.594$ $c = 2.959$	$a = 9.184$ $b = 5.447$ $c = 5.154$
Space group	$I4_1/amd$	$P4_2/mnm$	$Pbca$
Density (g/cm^3)	3.79	4.13	3.99
Band gap (eV)	3.20	3.00	3.26
Wavelength (nm)	387.50	413.33	380.37
Reference	(Zhang, Zhou, Liu, & Yu, 2014)	(Park, Van de Lagemaat, & Frank, 2000)	(Paola, Bellardita, & Palmisano, 2013)

Anatase TiO_2 is usually applied as a photocatalyst under UV illumination. It corresponds to the crystalline structure of the tetragonal system. The transformation of anatase does not have a certain temperature because the methods and processes that are involved in the transformation to promote or inhibit this phase transformation have not been reviewed and discuss thoroughly. The anatase transformation is irreversible to rutile at elevated temperatures (> 700 ^{o}C). Usually, the pore structure, specific surface areas, crystallite size, and phase structure is strongly influenced the photocatalytic activity of TiO_2 (Zhang *et al.*, 2014). Due to the anatase having a lower rate of recombination and higher capacity of surface adsorption to OH^- compared to rutile, the photocatalytic activity of anatase is actually superior to the rutile phase (Luttrell *et al.*, 2014). However, the absorbance ability of anatase is weaker towards the light compared to rutile due to the greater band gap than that rutile phase. Besides that, it was reported that the photogenerated h^+ and e^- lifetime in anatase is about an order of magnitude larger than that of photogenerated h^+ and e^- in rutile, and thus this greatly improving the chance of photoexcited h^+ and e^- in anatase taking part in surface chemical reactions (Xu *et al.*, 2011).

Rutile is one of the TiO_2 polymorph with the crystal structure of tetragonal. Rutile primarily is one of the components in paint as the white pigment due to its excellent light scattering ability with virtually chemically inert, nontoxic, and no absorption. In the paint industry, due to the chemical stability of rutile is better than anatase at all temperatures and it more efficiently to scatters white light, thus, rutile is favoured over anatase. Nonetheless, anatase is favoured for its higher photocatalytic activity due to higher energy of CB for photocatalytic applications and its surface chemistry. In the thermodynamic aspect, the transformation of anatase to rutile is irreversible because negative pressures are required for anatase to stay in a condition that more stable than rutile. Rutile is potentially lower cost to synthesis and has superior characteristics in light scattering, which is a beneficial property for light harvesting. Despite this, rutile should not be overlooked as a potential material for photocatalytic applications.

2.4.1.2 Applications

TiO_2 nanomaterial was used in a wide range of applications (*e.g.* dye-sensitised solar cell, paints, sensor devices, separations, as well as photocatalysis). Due to its many potential applications, recently, the nanostructures of TiO_2 have become the interesting topic for many scientists around the world. Table 2.3 lists the uses of TiO_2 in various field of study. The unique chemical and physical properties of TiO_2 crystal structures are affected not only by the surface properties, organisation, shape, and size, but also the intrinsic electronic structure (Suttiponparnit *et al.*, 2011). To be specific, some physicochemical properties such as selectivity, catalytic reactivity as well as adsorption are majority depending on the configuration of the atomic surface (Zhang *et al.*, 2014).

Since a promising TiO_2 photoanode for UV driven photochemical water splitting was first demonstrated Fujishima and Honda (Fujishima & Honda, 1972), TiO_2 was gain attention for PEC water splitting. In recent years, TiO_2 nanomaterial was studied in different kind of shapes such as nanotubes and nanowires. Table 2.4 lists the water splitting performance of PEC by applying TiO_2 as the photocatalyst.

Table 2.3: The applications of TiO_2 in various field of study.

Application study	Year	Reference
Dye-sensitised solar cell (DSSC)	2005	(Yum, Kim, Kim, & Sung, 2005)
Biomedical	2007	(Evans & Sheel, 2007)
Superhydrophilic surfaces	2012	(Joung & Buie, 2012)
Photoreduction of nitric oxide	2012	(Wu & Van De Krol, 2012)
Degradation of NO_x	2012	(de Melo & Trichês, 2012)
Gas sensing	2013	(Jiang *et al.*, 2013)
Corrosion protection of stainless steel	2013	(Park, Kim, & Park, 2013)
Solid-phase microextraction (SPME)	2013	(Banitaba, Davarani, & Pourahadi, 2013)
Cladding	2013	(Firouzdor, Brechtl, Hauch, Sridharan, & Allen, 2013)
Dye-sensitised solar cell (DSSC)	2014	(Abdullah, Razali, Shaari, & Taha, 2014)
Gas sensing	2014	(Esmaeilzadeh *et al.*, 2014)
Photodegradation of triclosan	2015	(Constantin *et al.*, 2015)
Photocatalytic water splitting	2015	(Han *et al.*, 2015)
Bio-implant	2016	(Clavijo, Membrives, Quiroga, Boccaccini, & Santillán, 2016)
Metallic filters	2016	(Noberi, Kaya, & Kaya, 2016)
Photodegradation of rhodamine B and orange II	2017	(Molla *et al.*, 2017)
Photodegradation of n-propanol	2017	(Zeng *et al.*, 2017)
CO oxidation	2017	(Chong & Yang, 2017)

Table 2.4: The performance PEC water splitting by using TiO_2 as the photocatalyst.

Sample	Electrolyte	Photocurrent density	Year	Reference
TiO_2 thin film	KOH	j_p-V: 0.57 mA/cm^2	2014	(Fakhouri *et al.*, 2014)
Cr-doped TiO_2	KOH	j_p-V: 0.36 mA/cm^2	2015	(Momeni & Ghayeb, 2015b)
Fe-doped TiO_2	KOH	j_p-V: 1.32 mA/cm^2	2015	(Momeni & Ghayeb, 2015a)
Black TiO_2	KOH	j_p-V: 0.99 mA/cm^2	2015	(Binetti, El Koura, Patel, Dashora, & Miotello, 2015)
TiO_2 nanorod	n/a	j_p-V: 1.24 mA/cm^2	2016	(Wang *et al.*, 2016)
TiO_2 nanotubes	water	j_p-V: 0.23 mA/cm^2	2016	(Wu, Xu, & Yan, 2016)
	Na_2SO_4	j_p-V: 0.40 mA/cm^2		

2.4.2 Strontium Titanate ($SrTiO_3$)

2.4.2.1 Properties

The strontium titanate ($SrTiO_3$) belongs to a *"perovskite"* material class, it is a ternary oxides of a structure ABO_3. ABO_3 denotes a class of binary metal oxides. In 1839, a mineral was discovered ($CaTiO_3$) and it is a ternary compound of formula ABO_3 that A and B cations differ in size. After this discovery, the ABO_3 structure was named as *"perovskite"*. $SrTiO_3$ is a typical ABO_3 perovskite type multi-metal oxide. At room temperature, $SrTiO_3$ exists in cubic form, but it transforms into the tetragonal structure at temperature less than 105 K. The $SrTiO_3$ structure can be described and viewed in different ways, but the most common view is as a ―corner-shared network" of TiO_6 octahedral in which Sr metals are filled in all interstitial 12 coordinate sites (Table 2.5).

For the band structure, $SrTiO_3$ is a semiconductor in nature with indirect and direct E_g of 3.20 and 3.75 eV, respectively. The electronic structure of $SrTiO_3$ near the Fermi level is dominated by the orbitals of the O 2p and Ti 3d hybridisation (Van Benthem, Elsässer, & French, 2001). The bottom of the CB consists predominantly of the Ti 3d orbital whereas the top of the VB is mainly formed by the O 2p orbitals. Due to a wide band gap, the $SrTiO_3$ is only responsive in the UV region. The VB electrons can jump to the CB by excitation, which can lead to an e^--h^+ pair generation when the $SrTiO_3$ is exposed to UV illumination and this caused the $SrTiO_3$ be used for a wide range of photocatalytic applications (Townsend, Browning, & Osterloh, 2012; Wei *et al.*, 2010; Zou *et al.*, 2012). Besides that, $SrTiO_3$ has distinctive physical properties (*e.g.* ferroelectricity, piezoelectricity, as well as high dielectric constants).

Table 2.5: The properties of $SrTiO_3$.

Properties	$SrTiO_3$
Unit cell	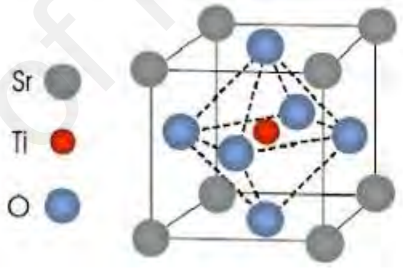
Crystal structure	Cubic
Lattice constant (Å)	$a = b = c = 3.905$
Space group	*Pm3m*
Density (g/cm^3)	5.12
Band gap (eV)	3.20
Wavelength (nm)	387.50
Reference	(Trainer, 2001)

2.4.2.2 Applications

The long lifetime on the e^--h^+ pairs, high stability from thermal and chemical, and strong catalytic activity become the advantages of $SrTiO_3$. Based on those properties stated above, $SrTiO_3$ has extensive applications such as photocatalysis, microwave devices, capacitors and some electronic functional ceramic materials. $SrTiO_3$ is applicable for many applications in the different area for industries because of its wide extraordinary transport and dielectric properties. Table 2.6 listed the uses of $SrTiO_3$ in various fields of study.

The $SrTiO_3$ nanostructures fabrications and uses are highly interesting in the research field. It was reported that the Sr^{2+} from the structure is able to accept electrons in the conduction band of photocatalyst to form Sr^+ (Yousefi *et al.*, 2015). Then the as-formed Sr^+ may also transport an electron to produce superoxide radical anions, which inhibit the recombination of photoinduced e^- and h^+. As listed in Table 2.7, recently, $SrTiO_3$ gain attention in water decomposition study due to it offers favourable energy for photocatalysis as its CB is 200 mV more negative compared TiO_2.

Table 2.6: The applications of $SrTiO_3$ in the different field of study.

Application study	Year	Reference
Dynamic random access memory (DRAM)	2008	(Lee, Kwon, Han, & Hwang, 2008)
Photocatalytic water splitting	2008	(Liu *et al.*, 2008)
Photodegradation of methyl orange	2009	(He, 2009)
Degradation of NO_x	2009	(Chen, Zhang, Wang, Xue, & Yin, 2009)
Degradation of NO_x	2010	(Sulaeman, Yin, & Sato, 2010)
Dye-sensitised solar cell (DSSC)	2010	(Yang, Kou, Wang, Xue, & Han, 2010)
Crystal growth and mechanism study	2012	(Kalyani *et al.*, 2012)
CO_2 conversion to CH_3OH	2012	(Sui *et al.*, 2012)
PL study	2012	(Souza *et al.*, 2012)
Photocatalytic water splitting	2012	(Yu, Yan, Li, Yu, & Zou, 2012)
Gas sensing (H_2S)	2012	(Kajale *et al.*, 2012)
Photodegradation of crystal violet	2014	(Huang *et al.*, 2014)
Magnetic properties study	2014	(Karaphun, Hunpratub, & Swatsitang, 2014)
Dye-sensitised solar cell (DSSC)	2014	(Jayabal, Sasirekha, Mayandi, Jeganathan, & Ramakrishnan, 2014)

Table 2.6 continued

H_2 production and decomposition of CH_3COOH	2014	(Kimijima, Kanie, Nakaya, & Muramatsu, 2014)
Photodegradation of rhodamine B	2014	(Hao, Wang, & Li, 2014)
Solid oxide cells	2014	(Sudireddy & Agersted, 2014)
Photodegradation of acid orange 7 and NO_x	2015	(Hou, Hu, Ho, Hu, & Huang, 2015)
Photodegradation of tetracycline	2015	(Wu *et al.*, 2015)
Photodegradation of methylene blue and rhodamine B	2015	(Mourão, Lopes, Ribeiro, & Mastelaro, 2015)
Electric double layer transistor	2015	(Tsuchiya, Ochi, Higuchi, Terabe, & Aono, 2015)
Electrical properties study	2016	(Lee *et al.*, 2016)
Photocatalytic water splitting	2016	(Ham *et al.*, 2016)
Memristor for neuromorphic systems	2017	(Jang *et al.*, 2017)

Table 2.7: The performance of PEC water splitting by using $SrTiO_3$ as the photocatalyst.

Sample	Photocurrent density	Year	Reference
Nb-doped $TiO_2/SrTiO_3$ nanotubular	j_p-V: 0.300 mA/cm^2	2012	(Yang, Lee, Kado, & Schmuki, 2012)
$SrTiO_3/Cu_2O$ heterojunction thin film	j_p-V: 0.530 mA/cm^2	2014	(Sharma, Verma, Satsangi, Shrivastav, & Dass, 2014)
$SrTiO_3$ nanoparticles	j_p-V: 0.003 mA/cm^2	2016	(He *et al.*, 2016)
$SrTiO_3$-rGO composites	j_p-V: 0.005 mA/cm^2	2016	
Cr/Ta-codoped $SrTiO_3$	j_p-V: 0.001 mA/cm^2	2016	(Chen *et al.*, 2016)

2.5 Synthesis of $SrTiO_3$ nanoparticles

ABO_3 compounds can be prepared by using different starting materials and synthesis conditions. Basically, the activity of the heterogeneous catalysts is affected by crystallinity, surface area, size, as well as crystal phase. The short diffusion distance of photoexcited electrons to the surface and large surface area could be the advantages of nano-particulate photocatalysts. Besides that, the outer surface and morphology of photocatalyst also influence their activity of photocatalysis. In this regard, the precise control of the shape and size of the $SrTiO_3$ is crucial for assessing the shape-dependent photoreactivity and developing high performance photocatalyst.

In addition, it was noticed that the E_g values if $SrTiO_3$ particles could be slightly different when different processing details and sample preparation method was used. The band gap of $SrTiO_3$ nanoparticles was found to be nearly 3.10 eV by conventional SSR (Liu *et al.*, 2008) and hydrothermal synthesis (Huang *et al.*, 2014). Also, it was reported by a researcher that $SrTiO_3$ nanoparticle was synthesised by SSR with ball milling assisted, the band gap is about 2.00 eV, which is photoactive in the visible region (Liu *et al.*, 2008). It was noticed metal impurities were found in $SrTiO_3$ lattice structure and this impurity was suspected alter the E_g value of the sample (Liu *et al.*, 2008). The $SrTiO_3$ nanoparticle was estimated to be 3.35 eV when co-precipitation synthesis was used (Chen & Chen, 2011) and about some researchers was synthesised $SrTiO_3$ nanoparticles with E_g value of 3.40 to 3.60 eV (Souza *et al.*, 2012).

A lot of scientists have reported producing $SrTiO_3$ in the variety of methods such as conventional SSR, sol-gel method, and hydrothermal reaction as listed in Table 2.8. Different synthesise pathway would lead to different morphology, crystallinity, uniformity, size, and shape of $SrTiO_3$ particles (Huang *et al.*, 2014).

Table 2.8: The preparation methods of $SrTiO_3$ nanomaterial.

Preparation method	Year	Reference
Ball milling assisted SSR	2001	(Berbenni, Marini, & Bruni, 2001)
Ultrasound irradiation synthesis	2006	(Xu, Lu, Liu, Shi, & Fang, 2006)
Polymerised complex synthesis	2008	(Liu *et al.*, 2008)
SSR		
Ball milling assisted solid-state reaction		

Table 2.8 continued

Sol-gel combustion	2008	(Liu *et al.*, 2008)
Sol-gel synthesis	2009	(Chen *et al.*, 2009; He, 2009)
Molten salt synthesis	2010	(Li, Du, Wang, & Zhang, 2010)
Microwave assisted synthesis	2010	(Malghe, 2010)
Solvothermal synthesis	2010	(Sulaeman *et al.*, 2010)
Molten salt synthesis	2011	(Wang, Liu, & Chen, 2011)
Microwave assisted hydrothermal synthesis (MAH)	2012	(Moreira *et al.*, 2012; Souza *et al.*, 2012)
Hydrothermal synthesis	2012	(Kalyani *et al.*, 2012)
Sol-gel hydrothermal synthesis	2012	(Yu *et al.*, 2012)
Solvothermal synthesis	2013	(Nakashima, Kera, Fujii, & Wada, 2013)
Sol-gel combustion	2013	(Klaytae, Panthong, & Thountom, 2013)
Hydrothermal synthesis	2014	(Huang *et al.*, 2014; Jayabal *et al.*, 2014; Karaphun *et al.*, 2014)
Solvothermal synthesis	2014	(Kimijima *et al.*, 2014)
Rapid sol-precipitation synthesis	2014	(Hao *et al.*, 2014)
Hydrothermal synthesis	2015	(Mourão *et al.*, 2015; Wu *et al.*, 2015; Zhang, Zhong, & Duan, 2015; Zhao *et al.*, 2015)
MSR	2015	(Zhang, Huang, Yanagisawa, & Yao, 2015)
Electrospinning method	2015	(Hou *et al.*, 2015)
Ultrasound assisted wet chemical method	2015	(Ashiri, Ajami, & Moghtada, 2015)
Solid-state crystal growth (SSCG) technique	2016	(Lee *et al.*, 2016)
Flux-mediated method (MSR)	2016	(Ham *et al.*, 2016)

2.5.1 Hydrothermal Method

In the ceramics industry, the hydrothermal reaction is a widespread method for the production small particles nowadays. The process of hydrothermal reaction is conducted in a steel pressure vessel called autoclave under a certain temperature and/or pressure with the reactions taking place in reaching the vapour saturation pressure. The amount of precursor added to the autoclave and the temperature largely determines the pressure produced during the synthesising process. It was known that the hydrothermal reaction normally has better control of the shape and size distributions as well as the crystallinity compared to others synthesis technique. It has been used to synthesise $SrTiO_3$ nanoparticles with or without the aid of surfactants.

It was proposed that the hydrothermal reaction to synthesise $SrTiO_3$ is a dissolution-precipitation process (Huang *et al.*, 2014; Zhang *et al.*, 2015). Some researchers were done the $SrTiO_3$ synthesis by different hydrothermal parameters (Table 2.9). It was found that different synthesis condition (*e.g.* temperature, pH, time and *etc.*) makes possible tuning the shapes of $SrTiO_3$ ranging from nanoparticles during hydrothermal reaction. A regular hydrothermal reaction would require the precursors mixing with the desired solvent as the medium, and is treated in an autoclave at high temperatures. Besides that, hydrothermal synthesis can also synthesise metal doped $SrTiO_3$ with a uniform nanoparticle sizes (Karaphun *et al.*, 2014; Wu *et al.*, 2015). The obtained precipitate is washed with distilled water to adjust the pH to become neutral (pH 6 to 7) before undergoing the drying and calcination process.

Table 2.9: The hydrothermal parameters studied by researchers.

Hydrothermal parameters	Year	Reference
Precursors for synthesis	2000	(Chen, Jiao, & Zhang, 2000)
Reaction time (0-370 min)	2004	(Zhang, Liu, Han, Chen, & Li, 2004)
Reaction time (1-120 h)	2010	(Tsumura, Matsuoka, & Toyoda, 2010)
Reaction time (0-160 min)	2012	(Souza *et al.*, 2012)
Amount of dopant (Cr/N codoping)	2012	(Yu *et al.*, 2012)
Amount of dopant (Fe)	2014	(Karaphun *et al.*, 2014)
Molarity of alkaline medium (1-10 M)	2014	(Huang *et al.*, 2014)
Reaction time (12-96 h)		
Reaction temperature (100-180 °C)		
Reaction time	2015	(Zhang *et al.*, 2015)
Mole ratio of Sr/Ti		
Amount of dopant (Mn)	2015	(Wu *et al.*, 2015)
Reaction time (0-480 min)	2015	(Mourão *et al.*, 2015)
Mechanical stirring		

In 2014, Huang *et al.* was reported a hydrothermal synthesised $SrTiO_3$ at different synthesis conditions. Based on the thermodynamic calculations of stability diagrams for the hydrothermal Sr-Ti system, high pH and mole ratio of Sr/Ti larger than 1 were required in order to produce a high purity of $SrTiO_3$ nanocrystals (Huang *et al.*, 2014). At the same time, Huang *et al.* reported the synthesis time could affects the $SrTiO_3$ nanoparticles size that would relate to process of Ostwald ripening where it was depended by both thermodynamic and kinetic effects (Huang *et al.*, 2014). The $SrTiO_3$ nanoparticle size would grow larger when the reaction time prolonged. This is due at the early stage of the reaction, nucleation occurs and formed smaller particles but the crystal growth process would occur at the prolonged time. In 2015, Mourão *et al.* reported a hydrothermal reaction of synthesis $SrTiO_3$ nanoparticles by study the mechanical stirring parameter (Mourão *et al.*, 2015). Based on Mourão *et al.*, mechanical stirring is a significant parameter for the hydrothermal process (Mourão *et al.*, 2015). During the hydrothermal reaction, the stirring process could increase the particle collision which would affect the properties of the final product. However, conventional hydrothermal synthesis produced a high roughness of $SrTiO_3$ nanoparticles and aggregation was found. Besides that, the $SrTiO_3$ nanoparticles sample that undergoes stirring during the hydrothermal reactions shows a better photocatalytic activity compared to the final product without stirring (Mourão *et al.*, 2015). In the same year of 2015, it was reported by researchers that during the hydrothermal reaction, the alkaline medium is a critically important role to dissolve the crystalline anatase TiO_2 powders (Zhang *et al.*, 2015). Moreover, the Sr/Ti mole fraction could directly influence the specific surface area and particle size in nucleation and crystal growth process. The short synthesis period and high mole fraction of Sr/Ti were helpful to synthesis large specific surface area and small particles of $SrTiO_3$. Meanwhile, long reaction time and lower mole fraction of

Sr/Ti were beneficial for large particles with small specific surface area formation (Zhang *et al.*, 2015).

2.5.2 Solvothermal Method

Besides that a various solvents other than water can be employed for this solvothermal process, this method is similar to the hydrothermal synthesis. The organic solvent such as carboxylic acids, ketones, toluene, and alcohols can be applied as the solvent medium (Wang, He, Lai, & Fan, 2014). Solvothermal synthesis has been determined to be a versatile route for the production of a wide variety of nanoparticles with uniform particle size, particularly when organic solvents with high boiling points are chosen.

In 2013, Nakashima *et al.* was reported to synthesis $SrTiO_3$ nanoparticles by using a mixture of 2-methoxy ethanol and absolute alcohol as the solvent (Nakashima *et al.*, 2013). The solvothermal technique is enabled for efficient particle shape and size control in the particular study. However, a secondary phase ($SrCO_3$) was observed by analysing the final product using XRD (Nakashima *et al.*, 2013). Besides that, Kimijima *et al.* was successfully synthesised $SrTiO_3$ particles in cubic, spherical, as well as flake-like shaped by using H_2O/polyols mixture solutions (*e.g.* H_2O/EG, H_2O/DEG, and H_2O/TMG) as the medium for solvothermal reaction in the same year (Kimijima *et al.*, 2014). It was found that, the solvent effect of glycols is the competitive factor for the control of final particle size and shape.

2.5.3 Solid State Method (SSR)

In a normal synthesis reaction to take place, the precursors are placed in a solvent initially. Researchers are able to remove the yield from the solvent after the synthesis was done. For SSR, however, it enables the precursors to react chemically in the absence of the solvent. The elimination of solvents indicates that it will cost lesser for production, therefore, SSR gains attention in industries. In addition, eliminating the solvent also indicates that a SSR yields more final product than others synthesis method. Since there is a ―solventless" reaction, there is no waste to remove at the final stage of the synthesis, thus, SSR also known as an environmentally friendly synthesis method. SSR can take place in several conditions. For example, oven method required higher temperatures to drive reactions without solvents whereas for melt method, the precursors are melted together. The melted precursors interact in the molten state and become a paste which then hardens into a solid. In order to form a homogenous product, SSR usually incorporates with ball miller.

There are many advantages to develop the SSR. Generally, $SrTiO_3$ powders for the industrial applications are produced by SSR of TiO_2 and $SrCO_3$ because of the inexpensive of the precursors and simplicity of the production. Nonetheless, there are also some disadvantages such as the ideal process should produce a uniform or homogeneous yield but some SSR do not. A high calcination temperature (> 900 ^{o}C) is required in this process causing many drawbacks of the final product (*e.g.* high degree of particle agglomeration and large particle size with lacking of uniformity). In addition, the particles produced by this technique is not small enough, the efficiency is too low and costs much energy also the drawbacks of SSR. Thus, to develop an environmental friendly and practical route for the scale-up production of monodisperse $SrTiO_3$ nanoparticles at lower cost and temperature is important.

In 2001, Berbenni and Burni were synthesised $SrTiO_3$ nanoparticles by using conventional SSR, however, the particles were found to be large and non-uniform (Berbenni *et al.*, 2001). In 2008, Liu *et al.* have done a comparison by synthesising $SrTiO_3$ nanoparticles by using conventional SSR and ball milling assisted reaction (Liu *et al.*, 2008). For conventional SSR, the average nanoparticles diameter of $SrTiO_3$ was found to be about 140 to 150 nm (Liu *et al.*, 2008). For ball milling assisted SSR, it formed a smaller $SrTiO_3$ nanoparticle size (*ca.* 50 nm), however, the $SrTiO_3$ nanoparticles sample was found to be contaminated with metal during the synthesis process and the photocatalytic activity is affected (Liu *et al.*, 2008). Recently, researchers were tried to reduce the temperature for SSR. In 2015, Zhang *et al.* was synthesis the $SrTiO_3$ by using low SSR temperature by using NaCl-H_2O assisted strategy (Zhang *et al.*, 2015). It was found that the NaCl-H_2O system can promote the diffusivity of Sr precursor and TiO_2. By assisted of NaCl-H_2O, the reaction temperature was managed to reduce from 900 ^oC to 750 ^oC. This method was also known as molten state synthesis (MSR). As a result, the NaCl-H_2O system can provide a favourable environment for the formation of $SrTiO_3$ nanoparticles at a lower temperature (Zhang *et al.*, 2015). In many cases, eutectic mixture of salts is used to lower the liquid formation temperature. For example, the melting points of NaCl and KCl are 801 ^oC and 770 ^oC, respectively, and that of mixture of half NaCl and KCl (eutectic composition) is 650 ^oC. However, it was reported that the downside of this method is the incorporation of impurities into the target material, a commonly observed phenomenon during the flux treatment (Muller & Ostrogorsky, 1994).

2.5.4 Sonochemical Method

In a sonochemical method, the chemical reaction of the starting materials proceeds in the presence of high-frequency ultrasonic waves. The sonochemical method usually used to control and improve the properties of the prepared photocatalyst, particularly its morphology and size, by generating ultrasonic waves. This method widely applied for materials including alloys, oxides, colloids, and carbides (Wang *et al.*, 2014).

In 2003, Yu *et al.* reported that the size control of the resulting $SrTiO_3$ is probably due to the change in the viscosity of the solvent systems. During the formation of $SrTiO_3$, the competition between the crystal growth and the nucleation is partially controlled by diffusion. The diffusion of particles is more difficult in solutions of high viscosity (Yu *et al.*, 2003). This favours the formation and crystallization of new nuclei, resulting in smaller crystal size. In 2006, Xu *et al.* reported to synthesise $SrTiO_3$ nanoparticles using sonochemical method (Xu *et al.*, 2006). The nanoparticle size of $SrTiO_3$ was in a ranging of 86 to 500 nm due to the nanoparticle size could be varied in different synthesis conditions such as the concentration of reactants, time, and sonication power (Xu *et al.*, 2006). Besides that, it was found the $SrTiO_3$ nanoparticle shape was in spherical, cubic, as well as star-like. A similar finding was reported by others researcher in 2015 (Ashiri *et al.*, 2015). Ashiri and Ajami have successfully synthesised $SrTiO_3$ nanoparticles in the low temperature of sonochemical synthesis. However, agglomeration was found based on the FESEM analysis.

Although sonochemical method enables fine tuning of $SrTiO_3$ nanoparticle size, the temperature of the sonicator during the synthesis step requires monitoring as any changes in the temperature can cause the gas cavitation and it might change the physical, chemical behaviour of the chemical reaction, as well as the photocatalyst properties.

2.5.5 Sol-gel Method

The sol-gel method is a versatile process used for producing a variety of oxide compounds. Generally, the sol-gel synthetic technique enables to control of the morphology, chemical properties, and the texture of the final products. This method also has a few merits over other synthesis techniques (*e.g.* enabling impregnation of co-precipitation, which can be applied to introduce dopants). The sol-gel process involves the metal alkoxide hydrolysis, condensation and followed by annealing at high temperatures to induce the polymerisation and producing a network of metal oxide (Verma, Samanta, Bakhshi, & Agnihotry, 2005). Sol-gel synthesis technique governs many benefits as discussed in previous.

Although sol-gel is a popular pathway for nanomaterial synthesis, however, the metal alkoxides precursor might be expensive. Also, a high temperature of calcination is always required for the post-treatment in order to get the final product in crystalline form. A low temperature of calcination might lead to the final yields with defects, low crystallinity and finally affects the photocatalytic activity. Furthermore, in the experimental condition, a slight change would produce different catalyst properties of yield. As a result, the sol-gel process should be taken accurately and carefully when producing $SrTiO_3$ using this method.

In 2001, a publication was successfully prepared $SrTiO_3$ by using sol-gel method (Bao, Yao, Wakiya, Shinozaki, & Mizutani, 2001). It was found that the crystallinity of the final product directly affected the E_g of $SrTiO_3$. High crystallinity of final product gives lower E_g that can relate to the photocatalytic activity. Meanwhile, for the poor crystallinity final product, it gives larger E_g compared to those single crystals. It was suspected that due to the quantum size effect and existence of amorphous phase in $SrTiO_3$ (Bao *et al.*, 2001).

2.6 Limitation of Powdered Photocatalyst for Water Splitting

Generally speaking, water splitting by photolysis is achieved primarily by two methods, which are (i) photolysis using colloidal suspensions of powdered photocatalysts (photocatalytic water splitting) such as TiO_2, and (ii) photoelectrolysis using PEC cells.

Figure 2.5 illustrates a simple schematic of the powdered photocatalyst for water splitting. Recently, much work has focused on a few important limitations of photocatalytic water splitting, such as the back reaction of unstable chemical species such as intermediates and this may affect the yield of H_2. The recombination of photogenerated charge carriers and light scattering of nanoparticles are potential to weaken the optical response of the powdered photocatalyst. Furthermore, it was known that the structuring of the surface on nanoscale and microscale potential to enhance the horizontal degree of light distribution by scattering of light. The scattering of light is maximum in particle suspensions due to it can take place at both the back and front sides of the nanoparticles. However, by direct reflection from a flat surface, the _trapped‘ light would be lost otherwise (Osterloh, 2013).

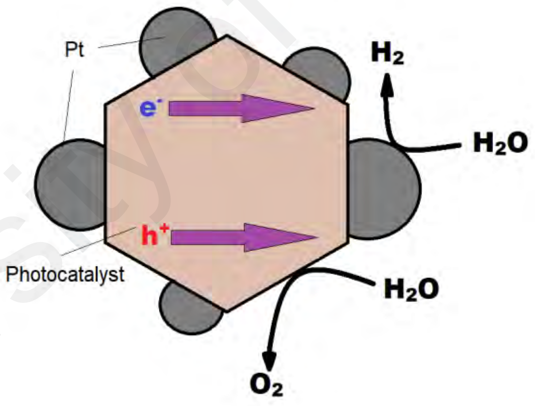

Figure 2.5: Simple schematic of the powdered photocatalyst for water splitting (n-type semiconductor).

As a result, this study is to improve the water splitting efficiency by fabricating the photocatalyst in the form of thin film. This thin film of the photocatalyst is applied to the PEC cell as photoelectrode. The thin film of photocatalyst gains many advantages compared to the photocatalyst those in powder form such as no post-filtration is required and decreases the possibility of charge carrier recombination due to the photogenerated e^- and h^+ are separated spatially to two different electrodes.

2.7 Thin Film Coatings as Photoelectrode

The photocatalyst coating is common for some certain application such as for dye-sensitised solar cell, wastewater treatment, anti-microbial, oxidation/corrosion protection as well as semiconductor industry in order to fabricate a thin layer of film on a substrate. Thin film is a layer of material ranging from fractions of nanometre to several micrometres in thickness.

The techniques of deposition can be divided into two major categories, which are physical and chemical deposition. The technique that uses thermodynamic, electrochemical as well as mechanical to produce a thin film of solid is known as physical deposition (*e.g.* physical vapour deposition, paste coating, and sputtering). Meanwhile, for chemical deposition, it consists of a liquid precursor that undergoes a chemical reaction at a surface of solid and leaving a solid layer (*e.g.* electroplating, chemical bath deposition, and chemical vapour deposition).

Nowadays, there are a lot coating method that available and widely studied by the scientist. Nevertheless, each of these methods has its own advantages and disadvantages (Table 2.10). Thus, this section will further discuss the principle of some coating technique, as well as its pros and cons.

Table 2.10: The photocatalyst coating technique.

Method	Advantages	Disadvantages	Reference
Electrophoretic deposition (EPD)	• Coating can be done on both large, small-scale and complex shape. • High versatility when used with different materials and their combinations. • The photocatalyst suspension can be reused.	✧ Coating can only be done on conductive surface (*e.g.* metal, and conductive glass)	(Chang *et al.*, 2010; Liou, Hsiao, Chen, Chu, & Teng, 2011; Yum *et al.*, 2005)
Paste coating	• Low production cost.	✧ Difficulty in control thickness and uniformity.	(Liou *et al.*, 2011; Xu & Wang, 2013)
Spin coating	• Relatively ease to handle.	✧ The material successfully coated is less, the rest being flung off the side and wasted. ✧ Hardly to apply for large-scale production.	(Hall, Underhill, & Torkelson, 1998; Yuan *et al.*, 2014)
Sputter deposition	• Able to produce good thin film quality. • Suitable for the variety of substrate (*e.g.* alloy, insulator, and metal).	✧ Ion bombardment or UV generated by plasma may cause substrate damage and material degradation (*e.g.* organic sample).	(Low, Lai, & Hamid, 2017)
Chemical vapour deposition (CVD)	• Produced high uniformity of the thin film. • Wide variety materials can be deposited with high purity.	✧ Conduct at high temperature and pressure are required. ✧ Precursors are required and it may produce hazardous by-product.	(Morosanu, 2016; Stassen *et al.*, 2016)
Chemical bath deposition (CBD)	• Required lower deposition temperature and good reproducibility.	✧ The coating process may take longer time, up to few hours. ✧ The coating solution unable to reuse after every deposition.	(Momeni & Nazari, 2016)

2.7.1 Electrophoretic Deposition (EPD)

EPD has been subjected to numerous experimental research and theoretical studies. EPD is a process that contains electrophoresis and deposition. Generally, Reuss, a Russian scientist discovered EPD in 1808 when he noticed the clay particles were moving in the water by applying electric field (Reuss, 1809). Then, in the 1980s, Hamaker was the first to study the EPD of ceramics (Hamaker, 1940).

Figure 2.6 illustrates the EPD process. EPD is a particulate forming process. It begins with a dispersed colloidal substance in a solvent and applies an electric field to move the colloidal particles into the desired arrangement on the surface of the electrode. There are four defining characteristics of EPD as it is used here (Van Tassel & Randall, 2006), which are (i) it begins with particles which are well dispersed and able to move independently in a solvent suspension, (ii) due to electrochemical equilibrium with the solvent, the particles must have a surface charge (iii) there is electrophoretic motion of the particles in the bulk of the suspension, and (iv) a rigid deposition of the particles is formed on the deposition electrode. At present, a high smoothness and uniform thin film can be prepared by using the EPD method efficiently due to the layer of nanoparticles was formed layer by layer.

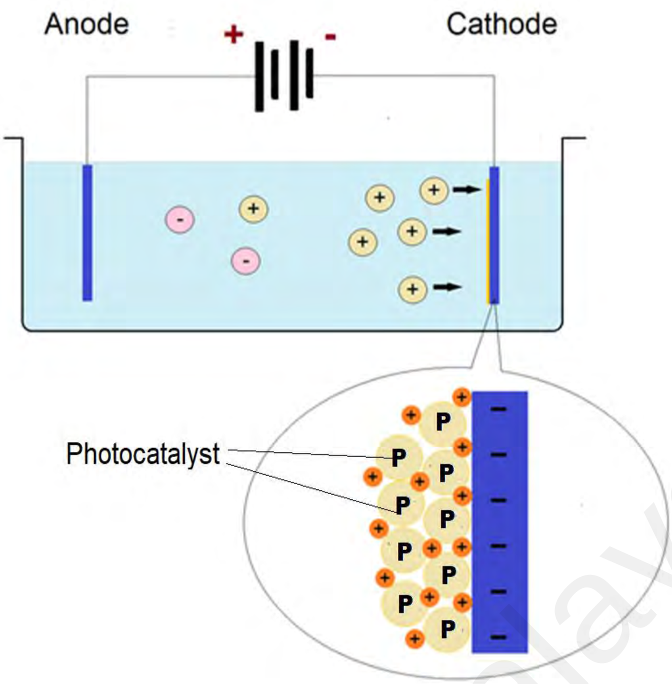

Figure 2.6: The principle of EPD process.

For material processing, the application of EPD was widespread as listed in Table 2.11. It was reported that the packing density of photocatalyst thin film could affect the interconnection between photocatalyst particles (Yum *et al.*, 2005). Therefore, the optimisation of deposition is required in order to fabricate a high smoothness and good uniformity of the thin film. It was reported that the EPD process could be optimised by several parameters such as deposition voltage, deposition time, distance of the electrodes, amount of photocatalyst suspension and the pH of the suspension (Besra & Liu, 2007). After this, some researchers had done a similar research in dye-sensitised solar cell application and it was found that the photocatalyst nanoparticles arrangement in the thin film is important due to it can affect the electron transport (Hsiao, Tung, & Teng, 2010; Hsiao & Teng, 2009). A rough thin film surface was generated a lower efficiency for the application due to numerous of voids and fissures appear in the thin film that can affect the compactness of thin film (Chang *et al.*, 2010).

Table 2.11: The use of EPD in different applications studies.

Deposits	Substrate	Application	Reference
TiO_2	ITO-PET	DSSC	(Chang *et al.*, 2010)
TiO_2	ITO	DSSC	(Yum *et al.*, 2005)
CdS	Al plates	Photodegradation	(Vázquez, Hernández-Uresti, & Obregón, 2016)
Fe_2O_3	Carbon plate	Tap water purification	(Sharif, Bakar, & Naim, 2015)
Alumina and TiO_2	Carbon fibre tows	Corrosion and oxidation protection	(Amiri, Mohammadi, & Afshar, 2016)
TiO_2	Stainless steel	Antimicrobial	(Höhn, Braem, Neirinck, & Virtanen, 2017)
TiO_2	FTO	PEC water splitting	(Phoon *et al.*, 2017)

2.7.2 Dip Coating

Dip coating method can be accounted as a coating process where a clean, wettable substrate is vertically dipped into the dilute suspension of colloidal particles and then withdrawn with a slow and precisely controlled lifting speed. When a substrate is immersed into the particle suspension, a meniscus region is formed on the substrate due to wetting, evaporation of the water from this meniscus leads to a constant suspension flux which brings the particles into the meniscus. The lifting speed of the substrate is one of the two crucial parameters in this method which we can change easily (particle concentration is another parameter), and it has strong effects in both crystallisation quality and thickness of the film. There may not be sufficient time for the particles to reach the substrate from the bulk suspension if the lifting speed is too high, whereas a very low lifting speed might produce a thick and disordered structure. Figure 2.7 shows the principle of dip coating. Although dip coating method is fast and easy to handle, however, the costly equipment (dip coater) might be the drawbacks of this method.

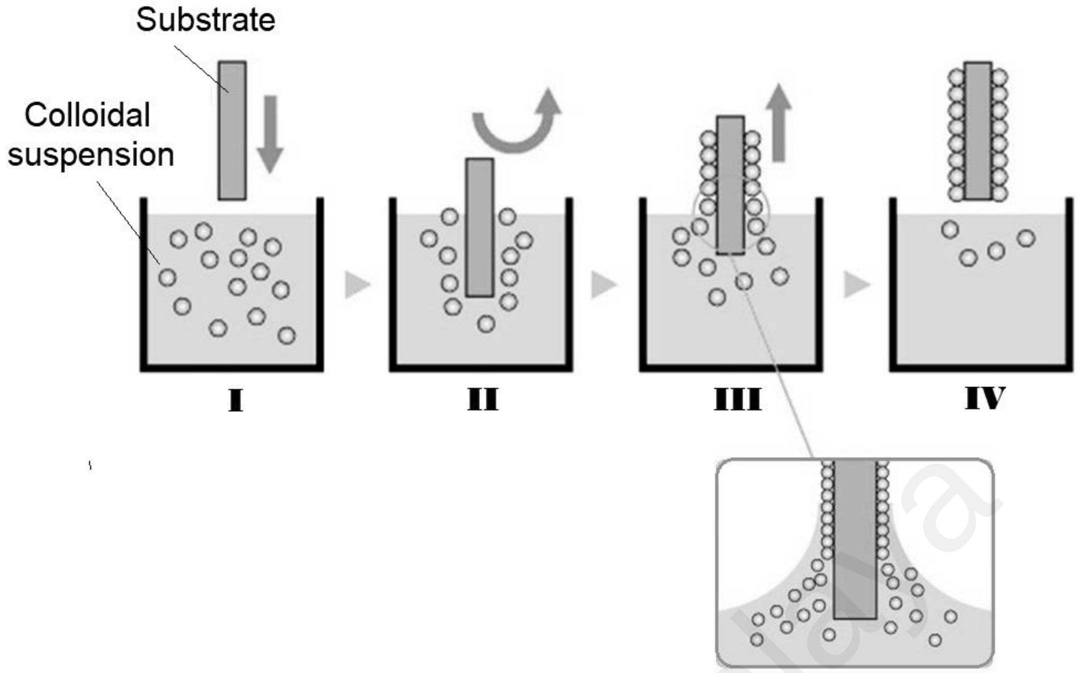

Figure 2.7: The principle of dip coating.

In 2013, Lee *et al.* was reported a research regarding to photocatalyst coating on a glass plate by using dip coating method (Lee, Ong, Hung, & Lee, 2013). According to the author, the efficiency of the application could be directly affected by the dip coating parameters (*e.g.* the number of coating cycle and the concentration of suspension) (Lee *et al.*, 2013). Although dip coating is a cost-effective method for coating, however, it has some drawbacks (*e.g.* the viscosity of colloidal suspension must be controlled and the dip withdrawal rate must be controlled for even coating thickness) (Lokensgard, 2016). In order to produce a uniform and reproducible thin film, dip coating equipment is commonly used in both laboratory and industry but the cost to install a dip coater might be expensive.

2.7.3 Spin Coating

Spin coating is a common method to produce uniform thin films of organic materials on flat substrates. This technique also can be used for fabricating of the colloidal sphere arrays by spin coating the colloidal dispersions on substrates. Evaporation of the solvent in the dispersion can be accelerated by spin coating so when the liquid becomes almost as thick as the diameter of the spheres, a strong immersion capillary attraction arises between the particles and assists the self-organisation of the particles. In the process, an excessive amount of suspension is placed on the wafer and then rotated at a high speed around the axis perpendicular to the substrate plane in order to spread the paste by centrifugal force. Due to the centripetal acceleration, most of the suspension is flung off the edge of the substrate, leaving a thin film of the particles after evaporation of the liquid on the wafer surface. Usually, the process of the spin coating has been separated into four distinct stages so that the physics of the spin coating process can be well modeled. Figure 2.8 shows the principle of spin coating. The four stages are (i) deposition, (ii) spin-up, (iii) spin-off, and (iv) evaporation of the solvent. Spin coating is a mature technique has been used very widely in many fields of industry (Patil, Nimbalkar, & Patil, 2018). Spin coating method has many advantages but it also has some disadvantages (*e.g.* lack of material efficiency because usually only 2-5% of the material is really used).

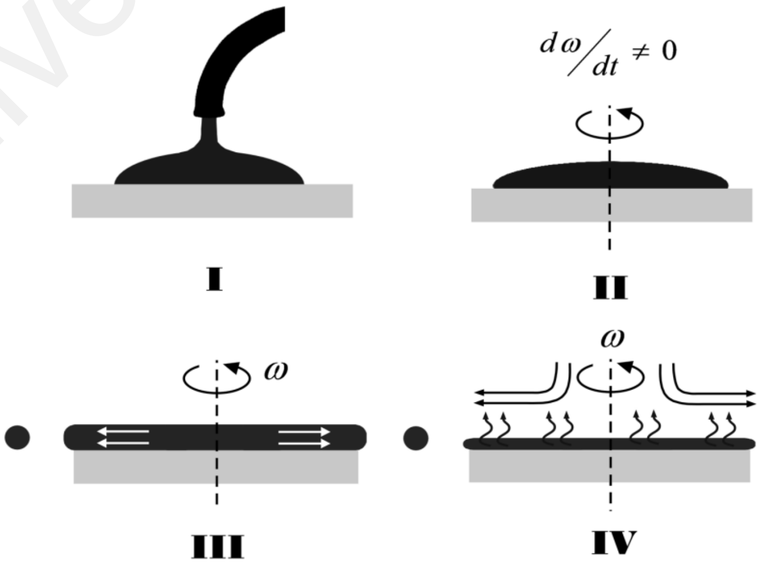

Figure 2.8: The principle spin coating.

2.7.4 Magnetron Sputtering

Magnetron sputtering is a coating technique widespread in both industrial and laboratory applications. In the process of conventional sputtering, a target (or cathode) is bombarded by ions of working gas generated in glow discharge plasma which is situated in front of the target. The sputtering ions are accelerated by a negative voltage applied to the cathode. The bombardment process causes eliminate of target atoms, which then condense on a substrate as a thin film (Sproul & Legg, 1995). The conventional sputtering process usually gives low deposition rates and need very high cathode voltage and working gas pressure to sustain the plasma. Figure 2.9 shows the cross-sectional scheme of RF-magnetron sputtering process. Basically, there are two types of sputtering depending on a working gas used in magnetrons. In non-reactive magnetron sputtering an inert gas (typically Ar) is used, whilst in reactive magnetron sputtering a chemically reactive gas (O_2 and N_2) is inserted to the system.

Although magnetron sputtering deposition can produce better film quality and able to deposit a wide variety of substrates, however, it consists of some disadvantages (*e.g.* some materials like organic compounds might be degraded due to the ionic bombardment). Moreover, the possibility of substrate damage can occur due to ion bombardment or UV generated by plasma and most of the incident energy on the target will become heat, which must be removed.

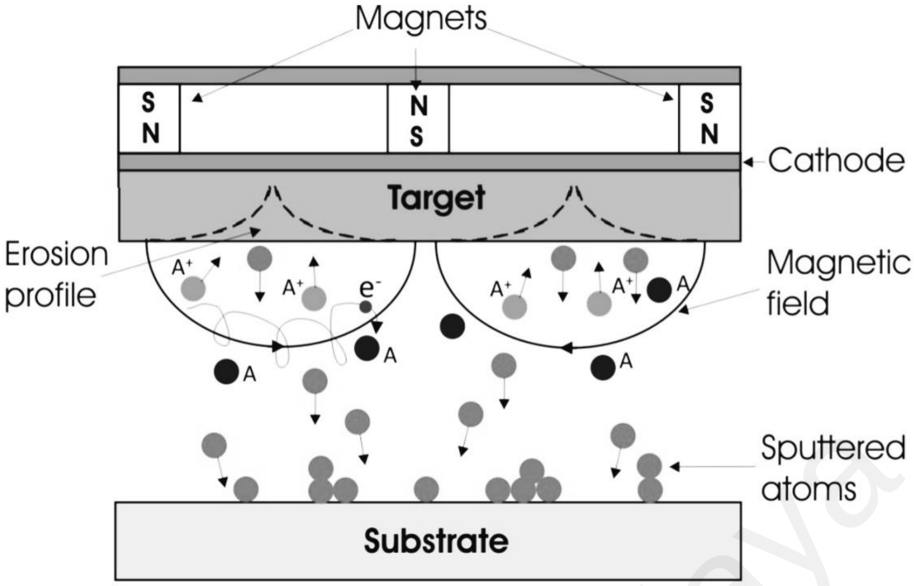

Figure 2.9: Cross-sectional scheme of RF-magnetron sputtering process.

2.8 Summary of Literature Review

In summary, H_2 is an ideal fuel of the future. In order to prevent GHG emission, some initiative was done by researchers to generate H_2 by RES. Due to its simplicity and cost-effectiveness, PEC water splitting has been chosen to generate H_2 in this research. There are some requirements for materials section in PEC water splitting. For example, the VB must lying at a more positive position than the water oxidation and the CB must lying at more negative than the water reduction potential level. Thus, based on the literature review, TiO_2 and $SrTiO_3$ are good candidate as photocatalyst in this study. In order to synthesise $SrTiO_3$, there are variety of methods are available. Hydrothermal reaction was chosen in this studies due to it can control the particle size, shape, crystallinity and morphology better without using extreme temperature. There were a lot of research studies on powdered photocatalyst water splitting previously. However, it has some limitation which would lower down the efficiency such as light scattering effect and backward reaction. Some invention was done by some researchers to coat the photocatalyst on conductive glass by using dip coating or paste coating. However, these methods could not produce a high smoothness of thin film. It was found that the smoothness and thickness of thin film would affect the efficiency. EPD is a coating method that able to control the thin film thickness and smoothness well. As a result, this research was to study the efficiency of PEC water splitting with TiO_2 and $SrTiO_3$ coated FTO glass by EPD method as photoelectrode.

CHAPTER 3: METHODOLOGY

The procedures that applied to synthesise the $SrTiO_3$ nanoparticles, the photocatalysts deposition method, the characterisation techniques, and the PEC water splitting performance test are described in detail in this chapter. In this study, $SrTiO_3$ nanoparticles were synthesised via hydrothermal reaction technique. The overview of the research methodology is displayed in Figure 3.1.

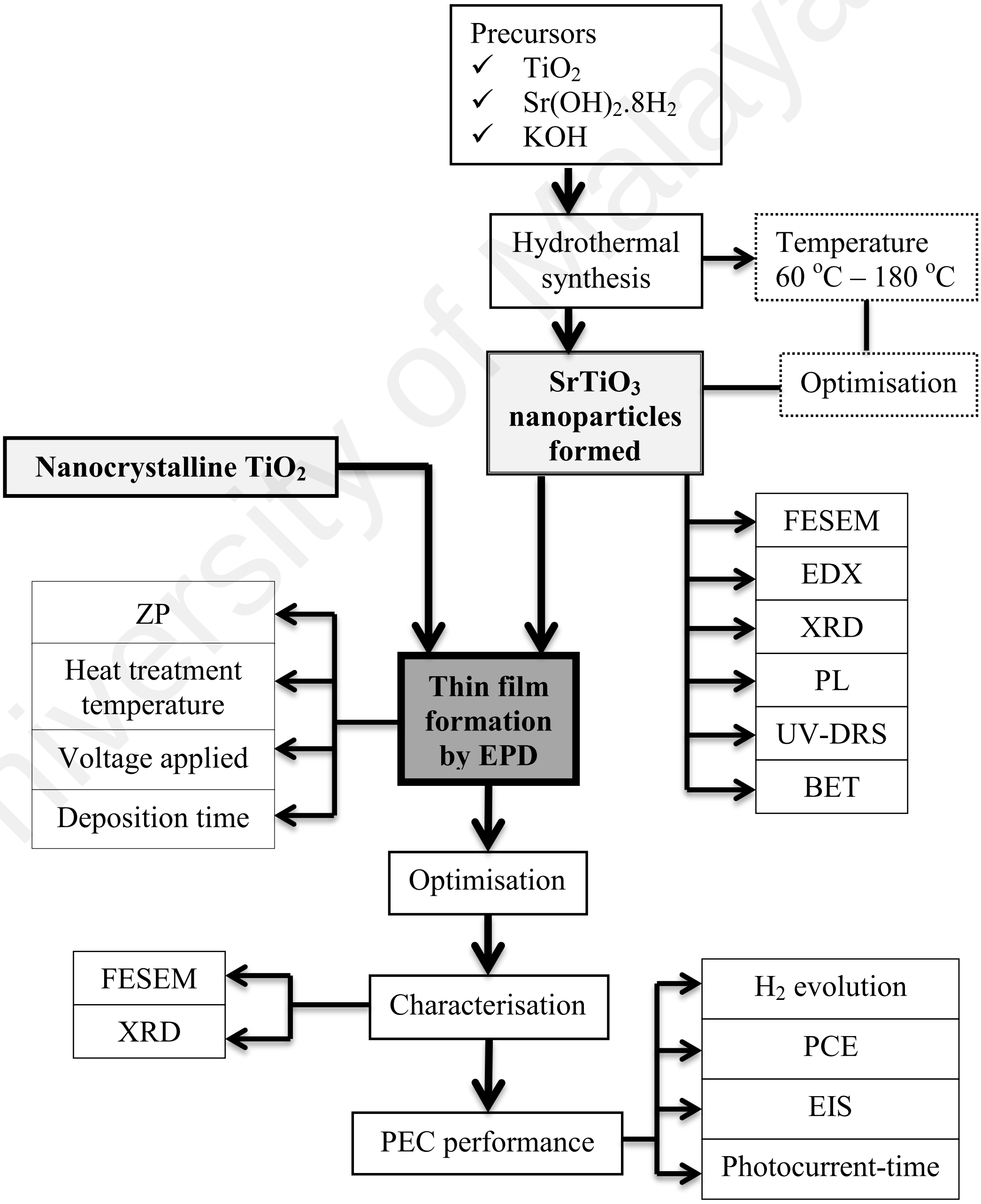

Figure 3.1: The overview of research methodology.

3.1 Materials Synthesis

3.1.1 Raw Materials

To synthesise $SrTiO_3$ nanoparticles via hydrothermal reaction, TiO_2 nanopowder, $Sr(OH)_2.8H_2O$, and KOH were used as precursors. Meanwhile, the materials and chemicals used in photocatalyst coating via EPD technique were acetone, IPA, $Mg(NO_3)_2.6H_2O$ and FTO glass. Besides, KOH is an alkaline inorganic compound that employed as an electrolyte in the PEC cell. The properties and some general information about the chemicals and raw materials that used in this study are listed detail in Table 3.1.

Table 3.1: The chemicals and raw materials used for the synthesis of $SrTiO_3$ nanoparticles and coating on FTO glass.

Material	Function	Manufacturer	Properties
Titanium dioxide (P-25)	Precursor	Sigma Aldrich	Chemical formula: TiO_2 Molar mass: 79.87 g/mol Purity: 99.9%
Strontium hydroxide octahydrate	Precursor	Sigma Aldrich	Chemical formula: $Sr(OH)_2.8H_2O$ Molar mass: 121.63 g/mol Purity: 95.0%
Potassium hydroxide	Precursor & electrolyte	Merck	Chemical formula: KOH Molar mass: 56.11 g/mol Purity: 85.0%
Acetone	Cleaning agent	Merck	Chemical formula: $CO(CH_3)_2$ Molar mass: 58.08 g/mol Density: 0.79 g/cm^3
Isopropanol	Electrolyte	Merck	Chemical formula: $(CH_3)_2CHOH$ Molar mass: 60.10 g/mol Density: 0.79 g/cm^3
Magnesium nitrate hexahydrate	Electrolyte	Sigma Aldrich	Chemical formula: $Mg(NO_3)_2.6H_2O$ Molar mass: 256.41 g/mol Purity: 99.0%
Fluorine doped tin oxide coated glass	Substrate	Sigma Aldrich	Thickness: 2.30 mm

3.2 Sample Preparation

3.2.1 $SrTiO_3$ Preparation

To produce $SrTiO_3$ nanoparticles, P-25 TiO_2 and $Sr(OH)_2.8H_2O$ was dissolved in 25 mL KOH aqueous solution. The mole fraction of TiO_2 and $Sr(OH)_2.8H_2O$ was set as ≥ 1. The mixture was stirred vigorously for 30 min. Thereafter, the above mixture was transferred into a stainless steel Teflon-lined autoclave of 50 mL capacity and the hydrothermal route was conducted in an oven. After convective cooling to room temperature, the solid precipitate was collected by centrifugation using centrifuge (TG16-WS) at the speed of 4000 rpm for 10 min and thoroughly washed with distilled water for several times until the pH value of the centrifugation liquid reached 7. The solid precipitate was dried in an oven for 12 h at 60 ^{o}C. In this work, different reaction temperatures were employed being prepared such as 60, 90, 120, 150 and 180 ^{o}C for 72 h.

3.2.2 FTO Glass Preparation

To ensure better deposition quality of $SrTiO_3$ nanoparticles as a thin film, cleanliness and purity of initial FTO glass are very important. Hence, any form of contaminations such as debris, grease, oil, and fingerprints must be eliminated prior to the deposition process. FTO glass with a thickness of 2.30 mm from Sigma Aldrich was used as the substrate in this study. FTO glass was cut into the desired dimension (20 mm x 10 mm) then degreased by sonication in acetone for 10 min using Thermo-6D Ultrasonic Cleaner (40 kHz, 180 W). FTO glass was then rinsed in distilled water and dried at ambient temperature.

3.2.3 Electrolyte Preparation

Electrolyte composition act as a crucial role in the deposition process. Structural morphology of the resulting deposits formed is highly depending on its composition. In the present study, IPA used as an electrolyte with dissolved $Mg(NO_3)_2.6H_2O$ and $SrTiO_3$ nanoparticles. This mixture was undergoing sonication for 10 min using Thermo-6D Ultrasonic Cleaner (40 kHz, 180 W). The purpose was to make sure $Mg(NO_3)_2.6H_2O$ dissolve into the IPA and $SrTiO_3$ nanoparticles dispersed homogeneously.

3.2.4 EPD Procedure

To perform deposition, FTO glass was connected to the anode of CBS Scientific EPS-200X DC power supply as the positive terminal in dual-electrode configuration. Another FTO glass, which acted as the CE was connected to the cathode, which acted as the negative terminal. Subsequently, both of the FTO glass from positive and negative terminal exposed into prepared IPA electrolyte. The distance between the positive terminal and negative terminal was fixed at 70 mm. The deposition was carried out through manually switched on and off to monitor the exposure time and desired potential. The EPD set up is as illustrated in Figure 3.2.

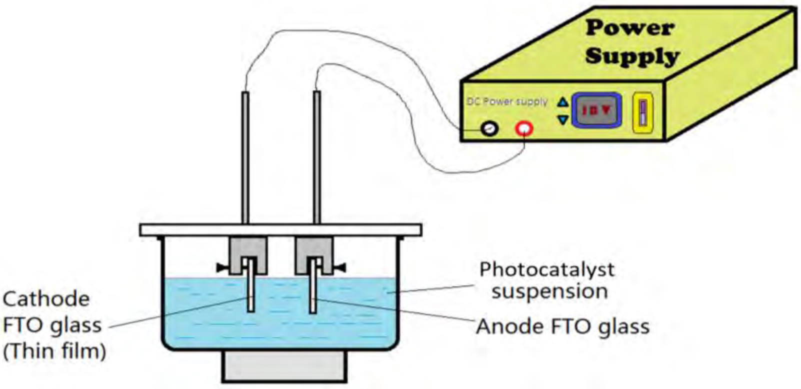

Figure 3.2: The EPD experimental setup.

3.3 Characterisation Techniques

3.3.1 X-ray Diffraction (XRD)

XRD is a sensitive analytical tool that provides crystallographic structure information, crystallite size, chemical composition, crystallite orientation, interface properties, and homogeneity of samples. It is a useful technique of characterisation that able to qualify and qualify the phases of crystalline in a solid.

All powders were characterised using an X-ray diffractometer (Bruker AXS D8 Advance, Germany) equipped with a high-intensity CuKα radiation source. The wavelength of CuKα radiation is 1.5406 Å. The patterns of diffraction were recorded from 20° and 80° at a scanning rate of 0.02° s^{-1}. The accelerating voltage was set to be 40 kV and the operating bean current was 30 mA.

The XRD basic principle is according to monochromatic X-ray beam that is directed onto a crystalline material which will get diffracted to generate the patterns of diffraction (Figure 3.3). The reflections are collected by a detector and observed at different angles with respect to the primary beam by exposing the material to radiation. These patterns will be indexed to get information on the phase of the material. The d-spacing can be calculated and generated by an X-ray scan, which provides a unique fingerprint of the materials present in the sample based on the Bragg‘s law (Equation 3.1),. The generated XRD patterns can be compared with the reference spectrum from the International Centre of Diffraction Data (ICDD) database, the sample phases can be identified and evaluated.

$$n\lambda = 2d \sin \theta \qquad \text{(Equation 3.1)}$$

where n is an integer, λ is wavelength, d is interatomic spacing, and θ is the diffraction angle in degrees.

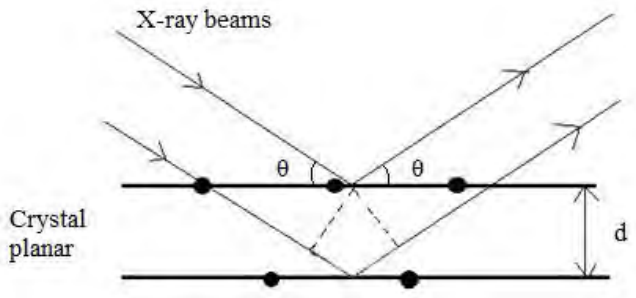

Figure 3.3: The Bragg's Law.

3.3.2 Field Emission Scanning Electron Microscopy (FESEM)

A FESEM is used to visualise tiny topographic details on the surface or entire or fractioned objects. Scientist in chemistry, biology, and physics apply this method to observe the structures that may be as small as 1 nm. Instead of light, a FESEM is a microscope that works with electrons. These electrons are liberated by a source of field emission. The interaction between the electron beam and the solid sample produces different types of emission as shown in Figure 3.4. These electrons near the surface can be knocked out of the solid sample. Those electrons that can be detected by FESEM to analyse surface morphologies are called secondary electrons. FESEM is advantageous to characterise powder morphology and size because of its ease of operation, simple preparation, large depth of field and nanoscale resolution.

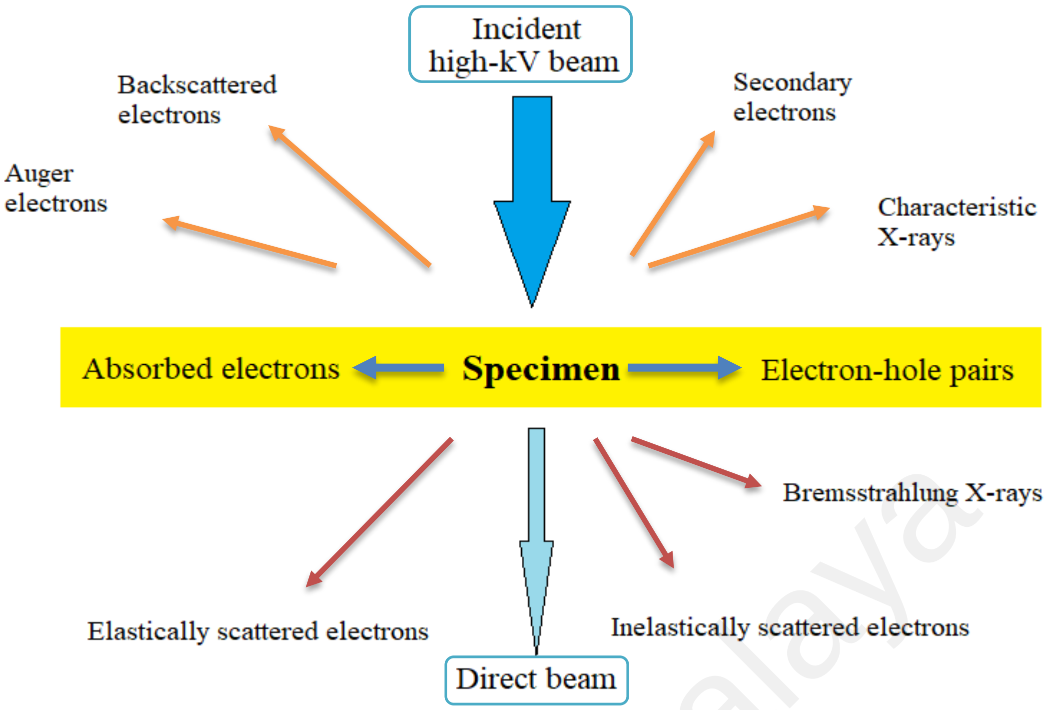

Figure 3.4: The Emission produced by the interaction of an electron beam with a solid sample.

The morphologies of powders were investigated using a FESEM (JEOL JSM 7600-F) that operated at 5 kV and 10 kV and magnification of 30, 50, 100 and 150 kX were normally used for characterisation in detail. Specifically, the powders for analysis were dispersed on carbon tape attached SEM stub. The excess powder was tapped off from the stub.

The Image-J software was applied to the measurement of the number of pixels in the scale bar of the FESEM images which was obtained and used to measure the diameter of the nanoparticles and the voids or holes and the film thickness of the sample.

3.3.3 Energy Dispersive X-ray (EDX)

EDX is known as an elemental composition analysis that applied together with FESEM. It has the same concept as FESEM by investigating the emitted X-rays from the sample during an electron beam bombardment and to analyse the elemental composition. A hole in an inner shell of the specimen atom is generated by an incident high-energy electron that loses the corresponding energy transferred to the ejected electron. The hole in the K shell is subsequently filled by an electron from an outer shell. The superfluous energy is emitted as a characteristic X-ray quantum. As shown in Figure 3.5, if the initial vacancy occurs in the K shell and the vacancy filling electron drops from the adjacent (L) shell, a Kα X-ray is emitted. If the electron drops from the M shell, which is two shells away, the emitted X-ray is Kβ. Similarly, if the L-shell electron is ejected and an electron from the M-shell fills the vacancy, Lα radiation will be emitted.

Features or phases as small as 1 μm or less can be analysed by EDX. The sample preparation is same with SEM analysis, where non-conductive materials need to be coated with Au or Pd layer. Analysis of compositions of elements of $SrTiO_3$ nanoparticles sample was determined by EDX.

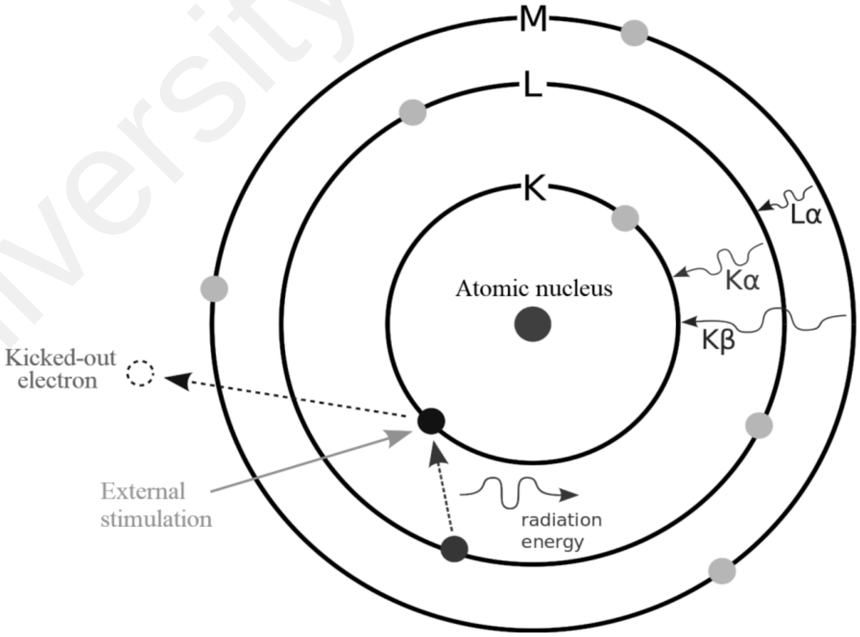

Figure 3.5: Schematic diagram of inner atomic electron shells.

3.3.4 Zeta Potential (ZP)

ZP is a physical property which is exhibited by any particle in suspension. The particles in a colloidal suspension or emulsion usually carry an electrical charge. In solution, the presence of a net charge on a particle affects the distribution of ions surrounding it, resulting in an increase in the concentration of counter-ions. The region over which this influence extends is called the electrical double layer (EDL). When all the particles have a large positive they will repel each other, and so the suspension will be stable. If the ZP is low the tendency for flocculation is increased. ZP is defined as the difference in potential between the surface of the tightly bound layer (shear plane) and the electro-neutral region of the solution (Figure 3.6). However, the value of ZP cannot be measured directly. By directly measuring the electrophoretic mobility of a particle, the ZP may then be determined using Henry‘s Equation (Equation 3.2). In this research work, the value of ZP was measured by Malvern Zetasizer (ZS90). The photocatalyst sample was dispersed in IPA and it was undergoing sonication for 5 min before transferring into a liquid cuvette. The technique for electrophoresis uses a combination of Laser Doppler Velocimetry (LDV) and phase analysis light scattering (PALS) to track the motion of particles in suspension.

$$U_E = \frac{2\varepsilon z f(Ka)}{3\eta} \qquad \text{(Equation 3.2)}$$

where U_E is the electrophoretic mobility, ε is the dielectric constant, z is the zeta potential, $f(Ka)$ is Henry‘s function, and η is the viscosity.

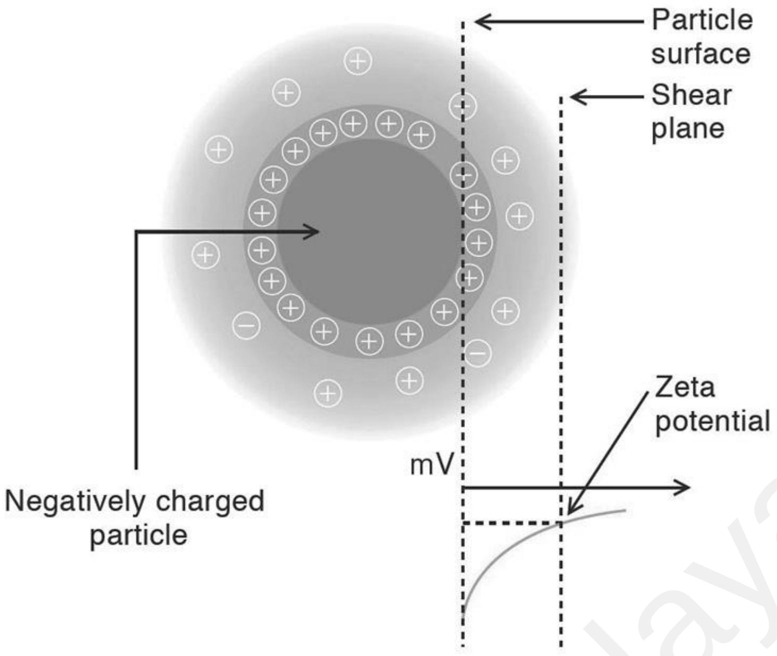

Figure 3.6: The principle of zeta potential.

3.3.5 Raman Spectroscopy

Raman spectroscopy is frequently used to study low-frequency modes of atomic and molecular systems of a sample, and such low frequencies fall mainly in the range associated with the rotational, vibrational and electronic level transitions involved in these systems. There are two types of Raman scattering, namely Stokes scattering and anti-Stokes scattering (Figure 3.7). Relying on the principle of Raman scattering, the Raman spectroscopy typically makes use of laser in the visible-near IR or near UV range. Incident photons from the laser interact with atoms and molecules in the sample, giving rise to a change in wavelength such as energy shift of the inelastically scattered photons, which will then give information about the various low-frequency modes of the systems in the sample by Raman spectrum. Basically, a Raman spectrum is to record the frequency and intensity of the inelastically scattered photons. Since every atom and molecules have its own Raman spectrum (fingerprint), this can be used to determine its atomic or molecular structure which can be used for identifying elements and/or compounds that are present in the sample being studied. Raman spectrum is typically plotted in terms of the energy shift with respect to the exciting line rather than by absolute wavelength since it is the energy of this shift which is significant. In this research, the crystal structures of the specimens were identified by using a Renishaw inVia Raman spectrometer over the range of 100 cm^{-1} to 1000 cm^{-1}, at an excitation wavelength of 532 nm (5 mW) generated by an Ar ion laser focused onto the micro-sized spot (1 µm).

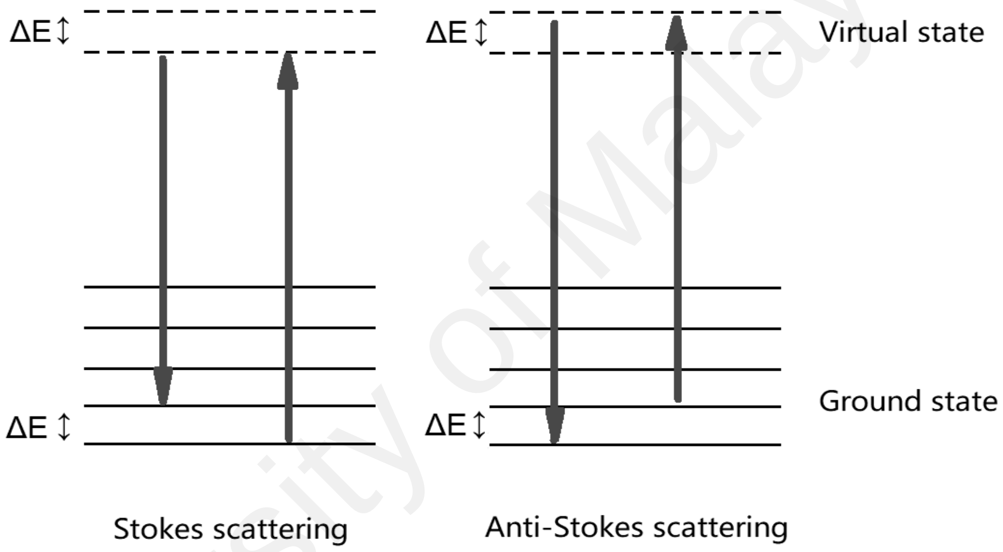

Figure 3.7: The Stokes, and anti-Stokes scattering.

3.3.6 Diffuse Reflectance-Ultraviolet Visible Spectroscopy (UV-DRS)

UV-Vis spectrophotometers were developed to determine the absorption values of liquid samples by measuring the relative change of transmittance of light as it passes through the solution. If the material has electronic energy levels that are separated by energy in the wavelength of light, then it may absorb the light energy to move electrons from the filled energy level (VB) into this empty level (CB) that causes a relative decrease in the amount of light at that particular energy. The spectrophotometer then measures this relative decrease in light transmission or increase in light absorbance. It is then possible to compute the energy E_g value of the material based on the UV-Vis spectrum, which shows the interaction of the material with light of various wavelengths resulting from excitation of the electrons from the VB into the CB.

The absorption and reflectance measurements of solid samples are done using UV-DRS spectrophotometers. Since light cannot penetrate opaque solid samples, it is reflected on the surface of the samples and UV-DRS measures the relative change in the amount of reflected light off of the surface of the samples. This will produce a UV-DRS spectrum which shows the interaction of the samples with a light of various wavelengths resulting from excitation of the electrons from the VB into the CB, similar to the spectrum of transmission/absorbance UV-Vis.

In this research, the optical properties of the $SrTiO_3$ nanoparticles were investigated using a Shimadu UV-2700 UV-Vis Spectrophotometer and UV-DRS measurements were done in the wavelength range of 200 to 800 nm using an integrating sphere. The connection between absorption coefficient (α) and the E_g can be expressed as Equation 3.3.

$$(\alpha h v)^n \propto \sim hv - E_g \qquad \text{(Equation 3.3)}$$

where α is the frequency, h is Planck's constant, and n is either 2 for an indirect transition or ½ for a direct transition.

3.3.7 Photoluminescence Spectroscopy (PL)

PL spectroscopy is a non-destructive and non-contact method for observing the electronic structure and recombination mechanism of materials. In essence, it is similar to Raman spectroscopy which initiates by photoexcitation, a UV or visible photo irradiate onto a material. The substrate absorbs photons further excite electrons from the equilibrium states to excitation states and emit photons as it relaxes and releases energy and returns back to equilibrium states. The emission of photons through this process is known as PL. The emitted photon energy relates to the transition energy level between equilibrium states and excites states. In photocatalysts, these two electron states (VB and CB) involved in the PL whereas the transition energy is known as E_g. Dissipation of electron energy to equilibrium stated is known as recombination. The quantity of PL emitted from a material is directly related to the relative amount of recombination rates. Recombination rates are typically associated with the level of photoexcitation, impurities surface defects and temperature. Thus, analysis of PL can qualitatively monitor changes in material quality as a function of growth and processing conditions and help understand the underlying physics of the recombination mechanism. In this research, recombination in the samples was characterised using a Photo Technology International Model Quantamaster-QM4m spectrofluorometer equipped with a 75 W lamp and dual excitation monochromatic beam with 325 nm wavelength at room temperature. The PL was recorded in the range of 350 nm to 750 nm.

3.3.8 Brunner-Emmet-Teller (BET)

Adsorption is defined as the adhesion of atoms or molecules of gas to a surface. It should be noted that adsorption is not confused with absorption, in which a fluid permeates a liquid or solid. The amount of gas adsorbed depends on the exposed surface are but also on the temperature, gas pressure and strength of interaction between the gas and solid.

BET is used to analyse the textural properties such as surface area, pore size, pore shape and pore volume of the sample. In BET surface area analysis, N_2 is usually used because of its availability in high purity and its strong interaction with most solids. The interaction between gaseous and solid phases is usually poor, the surface is cooled using liquid N_2 to obtain detectable amounts of adsorption. Known amounts of non-corrosive gases (*e.g.* N_2, CO_2 or Ar) are then released stepwise into the sample cell. Relative pressures (P/P_o) less than atmospheric pressure are achieved by creating conditions of a partial vacuum. After the saturation pressure, no more adsorption occurs regardless of any further increase in pressure. Highly precise and accurate pressure transducers monitor the pressure changes due to the adsorption process.

After the adsorption layers are formed, the sample is removed from the N_2 atmosphere and through pressure manipulation to cause the adsorbed N_2 to be released from the material and quantified. The data collected is displayed in the form of a BET isotherm, which plots the amount of gas adsorbed as a function of the relative pressure. Adsorption isotherms basically can be categorised to be 5 types which are Type I, II, III, IV and V (Hwang & Barron, 2011).

The photocatalyst samples were analysed using N_2 adsorption-desorption analyser TriStar II 3020 Surface Area and Porosity analyser at 77 K in this research. The dried sample was degassed at 300 ^{o}C for 4 h before measurement and the sample was measured using relative pressure in the range of 0.01 to 0.90 of P/P_o.

3.4 Photoelectrochemical (PEC) Measurement

The PEC properties of the samples were characterised using a tri-electrodes PEC cell under UV irradiation. Specimen was served as the WE, Pt rod served as the CE and Ag/AgCl in saturated KCl served as the RE. These electrodes consequently dipped in electrolyte used for PEC cell consisted of 1 M KOH aqueous solution. All three electrodes were connected to the potentiostat (Autolab PGSTAT 204, Netherlands) by using a control software NOVA for photoelectrochemical measurements. The current range is fixed from 10 mA to 10 nA.

All $SrTiO_3$ nanoparticles on FTO glass samples (photoelectrodes) were characterised through linear sweep potential as PEC performance. A 100 W UV lamp (Sylvania) was used as the light source, with intensity 100 mW/cm^2 light beam was focused on the immersed portion of WE. Graphically illustration of the photocurrent (mA^{-1}) vs. applied bias potential (V) was generated over the -1.5 V to 1.0 V range scan rate of 5 mV/s under light illumination and also in dark.

Among all $SrTiO_3$ nanoparticles on FTO glass samples, the best PEC performance used in H_2 evolution measurement. The H_2 evolution measurement was subsequently performed under bias potential 0.6 V for 1 h. The H_2 gas generated at Pt rod was collected with a reverted burette using the water displacement technique. As the H_2 gas is produced at CE in the PEC cell, it will bubble up into inverted burette (Figure 3.8). The volume of gas is determined by reading the gas level on the side of burette.

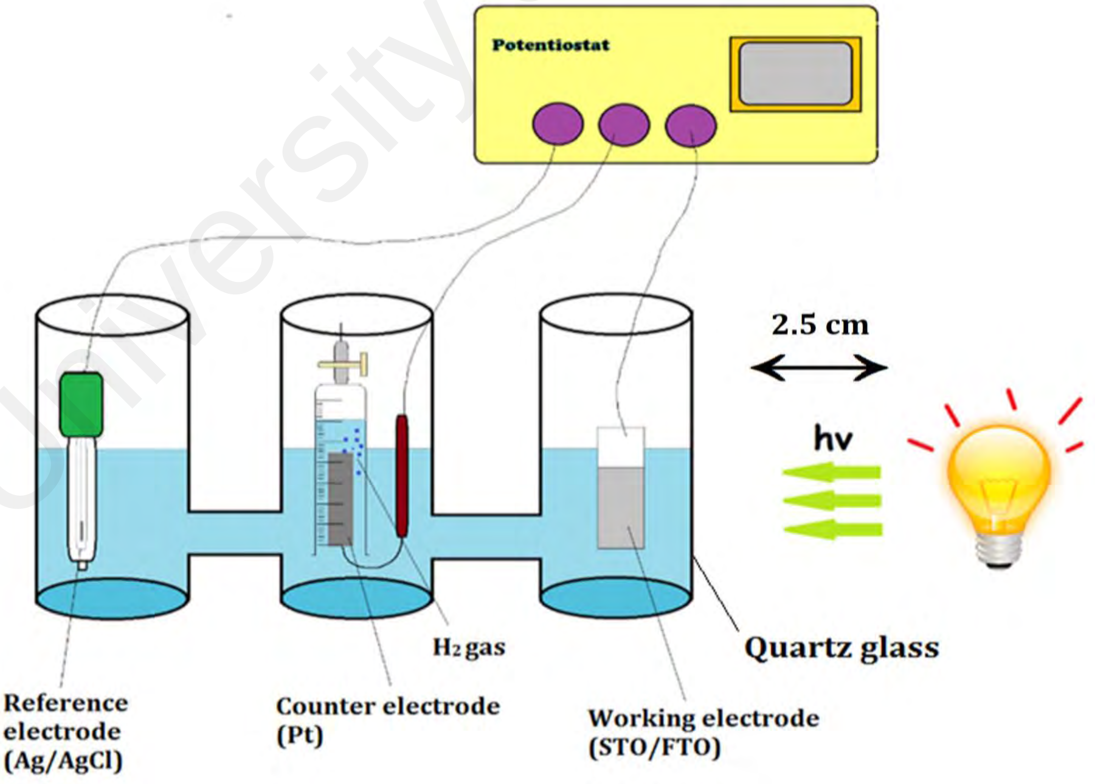

Figure 3.8: The PEC water splitting experimental set-up.

3.5 Calculations

3.5.1 Scherrer's Equation

The crystallite size of the $SrTiO_3$ nanoparticles were calculated using the Scherrer‘s equation (Equation 3.4) (Cullity, Cullity, & Stock, 2001).

$$d = \frac{k\lambda}{\beta \cos\theta} \qquad \text{(Equation 3.4)}$$

where d is the mean size of the crystallite domains, which may be smaller or equal to the grain size, k is the shape factor which has a typical value of about 0.9 and varies with the actual shape of the crystallite, λ is the wavelength, θ is the Bragg‘s angle, and β is the line broadening at half the maximum intensity which is termed full-width at half maximum (FWHM).

3.5.2 Kubelka-Munk's (KM) Equation

Kulbelka-Munk‘s theory was used to estimate the band gap of synthesised $SrTiO_3$ nanoparticles in this research (Murphy, 2007). By plotting $[F(R)h\nu]^{1/r}$ vs. $h\nu$, the intercept between the linear extrapolation of the graph and the baseline results to the E_g value.

$$F(R) = \frac{k}{s} = \frac{(1-R)^2}{2R} \qquad \text{(Equation 3.5)}$$

where k and s are absorption and scattering coefficients, respectively, R is the reflectance at the front face. $F(R)$ is the KM function and is an indicator of light absorption ability, with higher $F(R)$ values representing stronger photoabsorption capability. The value of R used was 2 for indirect allowed transition. Other r values include 1/2 (direct allowed transition), 3/2 (direct forbidden transition) and 3 (indirect forbidden transition).

3.5.3 Photoconversion Efficiency (PCE)

The overall photoconversion efficiency (η) is used to define the highest energy output that able to be generated from a product from energy supplies in the form of light. The conversion efficiency defined as the ratio of its electric power output to the incoming light intensity that strikes the cell as shown in Equation 3.6.

$$(\eta) = \frac{Total\ power\ output - Electrical\ power\ output}{Light\ power\ input}\ x\ 100\%$$

$$= \frac{j_p(E^o rev - |E_{app}|)}{I_o}\ x\ 100\% \qquad \text{(Equation 3.6)}$$

where j_p stand for photocurrent density (mA/cm^2), both $j_pE^o{}_{rev}$ and $j_p|E_{app}|$ are total power output and electrical power input respectively, I_o is the incident light power density (mW/cm^2), $E^o{}_{rev}$ is the standard reversible potential (1.229 V/SHE) and $E_{app} = E_{mean} - E_{voc}$. E_{mean} is the WE potential (vs. Ag/AgCl electrode) under illumination and E_{voc} is the OCP (vs. Ag/AgCl electrode) of the WE.

3.5.4 Hydrogen Production Rate

The H_2 production rate as shown in Equation 3.7 was used to calculate the amount of H_2 produced per hour.

$$H_2\ generation\ rate = \frac{Volume\ of\ hydrogen\ gas\ generated\ (mL)}{Area\ of\ sample\ (cm^2) \times Time\ (h)} \qquad \text{(Equation 3.7)}$$

CHAPTER 4: RESULT AND DISCUSSION

The outcome of the experiment conducted and the discussion on the experiment results are presented in this chapter. There are two major sections in this chapter. **Section 4.1** discusses the formation of the TiO_2 thin film by EPD method. Colloidal stability of the nanoparticles suspension, the effect of heat treatment temperature, electric field applied, and deposition time on resultant TiO_2 thin film formation are examined and evaluated in detail. Meanwhile, **Section 4.2** of presents the formation of $SrTiO_3$ nanoparticles by hydrothermal synthesis at different reaction temperatures. The physicochemical properties such as morphology, crystallinity, particle size distribution, optical response and specific surface area were determined. The formation of $SrTiO_3$ thin film by EPD method will be discussed in **section 4.2.2** and several parameters will be optimised such as colloidal stability, electric field applied, and deposition time. Finally, **section 4.3** discusses the efficiencies between TiO_2 and $SrTiO_3$ for PEC water splitting.

4.1 Formation of nanocrystalline TiO_2 Thin Film Coatings by EPD

This section will discuss the formation nanocrystalline TiO_2 thin film by EPD method. Basically, there are two categories of parameters determine the EPD characteristics, which are (i) parameters that related to the suspension, and (ii) parameters that related to the process of deposition such as physical parameters. In this section, the colloidal stability of TiO_2 suspension, the effect of post-annealing, the effect of deposition voltage and the effect of deposition time will further discuss and determine the optimum condition to deposition nanocrystalline TiO_2 thin film as PEC water splitting cell photoelectrode.

4.1.1 Colloidal Stability Analysis by ZP

ZP play three major roles in EPD, which are (i) to stabilise the suspension by defining the intensity of repulsive interaction between particles, (ii) to find out the migration velocity and direction of the particles during EPD, and (iii) to determine the green density of the deposits (Besra & Liu, 2007). The purpose of ZP measurement is to indicate the stability of nanocrystalline TiO_2 as a suspension in IPA. Basically, the ZP value could be affected by two factors, which are pH, ion species and ionic strength (Carneiro-da-Cunha, Cerqueira, Souza, Teixeira, & Vicente, 2011). It was suggested by researchers (Zarbov, Schuster, & Gal-Or, 2004), additives such as $Mg(NO_3)_2.6H_2O$ can influence the ionic conductivity of the suspension that able to become a driving force and transfer particles to the electrode. Therefore, in order to make sure a high surface charge of the suspended particles, ZP measurement is necessary for EPD process.

Figure 4.1 presented the ZP value of TiO_2 suspension by adding the different amount of $Mg(NO_3)_2.6H_2O$. The ZP value increased when the amount of Mg salts increased from 10^{-6} to 10^{-4} M. The value of ZP reached the maximum when 10^{-4} M of Mg salt was added to the suspension, which is 32.2 mV. However, further increase the Mg salt did not increase the ZP value, but the value was shifted to less positive value instead. This phenomenon due to the $MgNO_3^+$ stick on the surface of TiO_2 nanoparticles and lead to the suspension to have excess positive chargers and therefore cause a higher stability of the colloidal suspension. However, the further increment of Mg salt concentrations would lower down the value of ZP due to the surface of TiO_2 nanoparticles are saturated for ion adsorptions and produce correspondingly much more counter ions in diffuse layer (Shane *et al.*, 1994). Meanwhile, the van der Waals force to become predominant due to the EDL from the structure of TiO_2 nanoparticles is compressed. In this time, the net force of nanoparticles is attractive and this is explained that TiO_2 nanoparticles undergo sedimentation (Jeon, Hong, Yoo, & Whang, 2000).

The finding is consistent with the earlier publication (Chang *et al.*, 2010; Yum *et al.*, 2005). The ionic strength shows a great influence on ZP values and it would affect the deposition rate and coagulation. ZP energy can reveal whether the colloidal nanoparticles are maintained in stable suspension. Therefore, it can be used to enhance the colloidal stability of the TiO_2 nanoparticles.

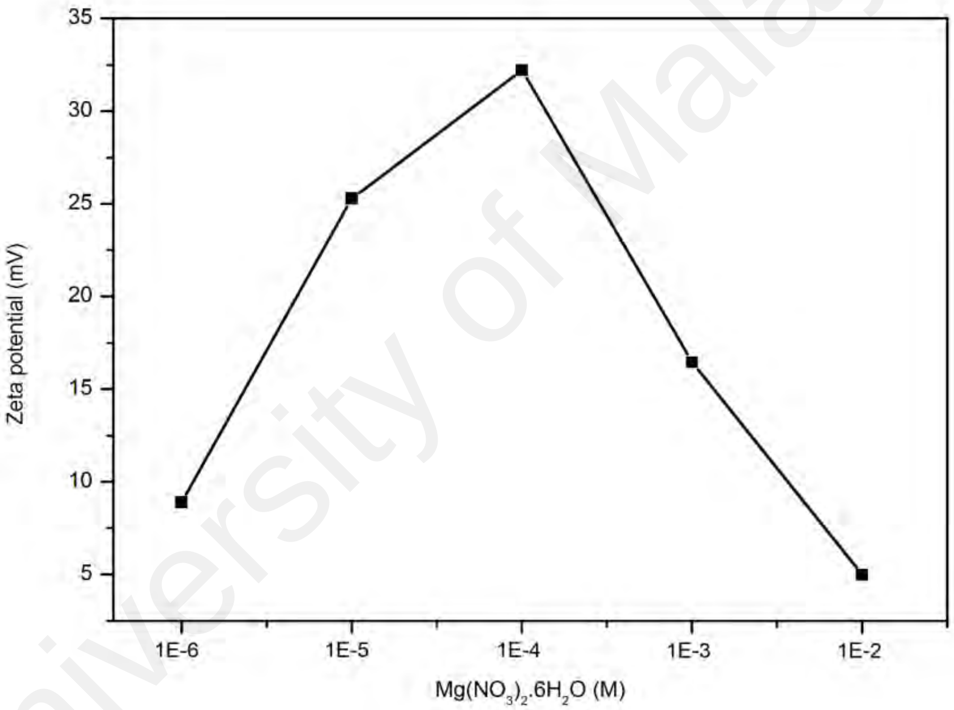

Figure 4.1: The ZP of nanocrystalline TiO_2 as a function of the concentration of Mg salt in the IPA.

4.1.2 Effect of Heat Treatment Temperature

The electrophoretic deposited thin film was undergoing heat treatment by calcination under air. The purpose to study heat treatment temperature parameter is to maintain the quality of thin film after the coating by EPD conducted.

The coated thin film was conducted in four different heat treatment temperatures, which are the as-annealing sample (without calcination), 200 °C, 400 °C and 600 °C of calcination. Figure 4.2 presents the j_p-V curves of nanocrystalline TiO_2 thin films that undergo heat treatment in various temperatures, as-annealed TiO_2 sample exhibits a weak photocurrent density among samples, which only generated 0.20 mA/cm^2 of photocurrent. Nanocrystalline TiO_2 thin film sample that underwent heat treatment at 400 °C has generated the best photocurrent density, which is 2.12 mA/cm^2. Nevertheless, the reading was slightly dropped to 1.60 mA/cm^2 when further increase the heat treatment temperature to 600 °C.

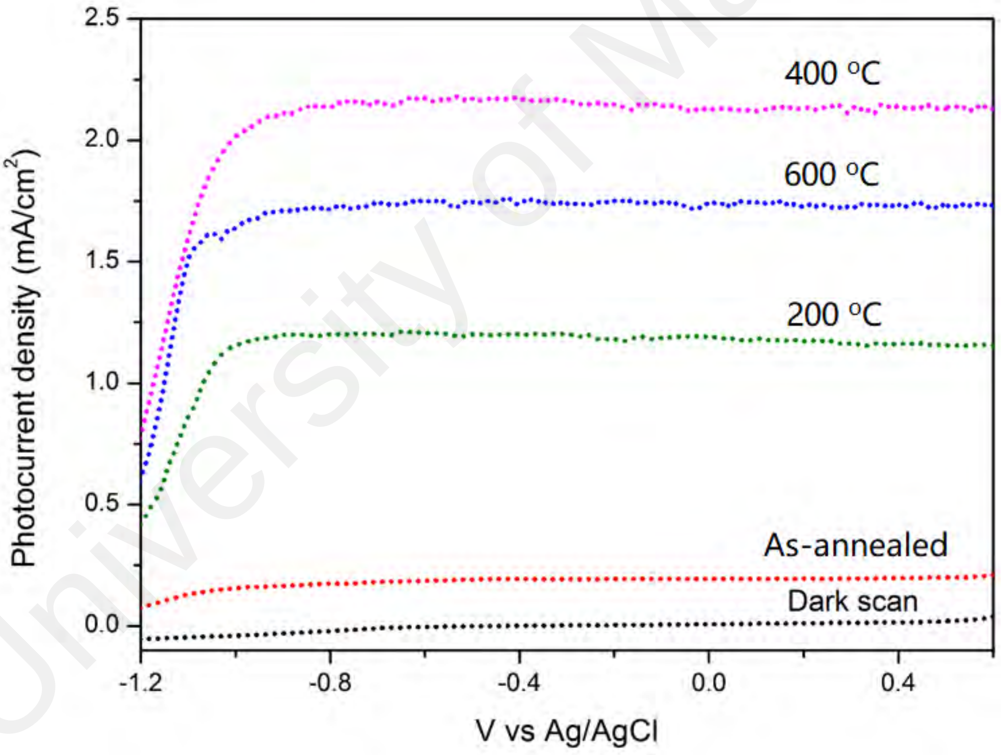

Figure 4.2: The j_p-V curves of nanocrystalline TiO_2 thin films that underwent heat treatment at different temperatures.

This finding can be explained by post heat treatment could enhance the attachment between TiO_2 nanoparticles and the FTO substrate. The result is consistent with earlier reports (Chang *et al.*, 2010). Also, Hsiao and Teng found that the purpose of thin film heat treatment is to enhance the necking of nanoparticles and this could influence the electron conveying ability of the nanoparticles (Hsiao & Teng, 2009). By referring to Raman spectrum that displayed in Figure 4.3, as-annealed nanocrystalline TiO_2 and nanocrystalline TiO_2 that underwent heat treatment at 200 °C and 400 °C show signals at 197, 394, 516 and 637 cm^{-1}, which represents the anatase phase. Yet, nanocrystalline TiO_2 that was heat-treated at 600 °C shows rutile peak at 446 and 612 cm^{-1} as well. This demonstrates that nanocrystalline TiO_2 was undergoing phase transformation at 600 °C. It was known that anatase can be better photocatalytic activity because it possesses an indirect band gap while the rutile has a direct band gap (Luttrell *et al.*, 2014). Due to the minimum in the CB is away from the maximum VB, this allows the excited electron to stabilise at the lower level in the CB, therefore, photocatalysts that exhibit indirect band gap would have longer charge carrier life (Odling & Robertson, 2015).

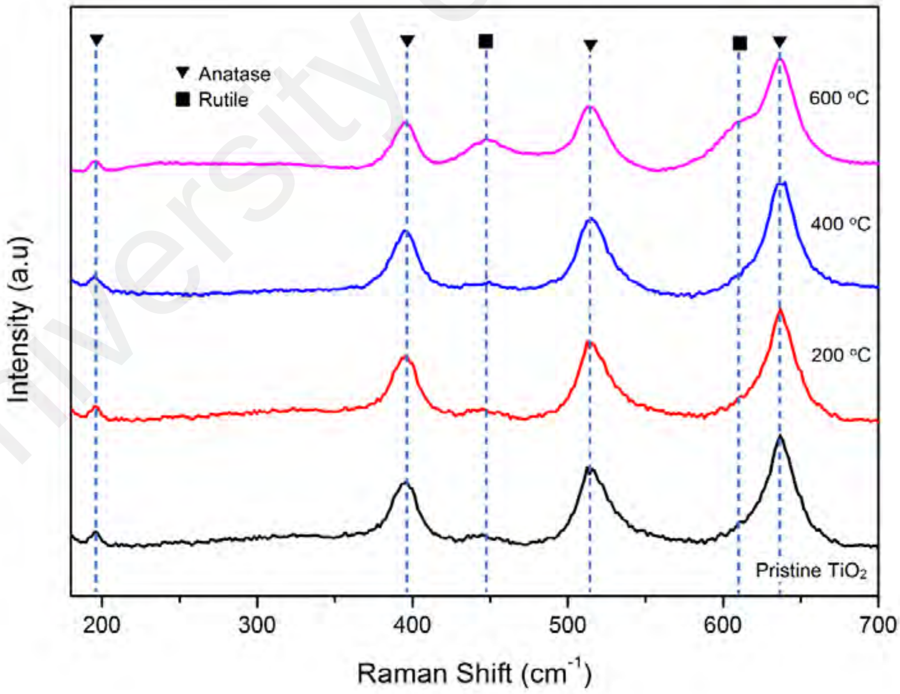

Figure 4.3: Raman spectrum of electrophoretically deposited nanocrystalline TiO_2 on FTO glass that undergoes at different temperature of heat treatment in the range of 190-700 cm^{-1}.

4.1.3 Effect of Electric Field Applied

The influence of electric field applied to the nanocrystalline TiO_2 deposition is discussed in this part of studies. Hamaker's equation (Equation 4.1) states that several factors could affect the deposition yield, including electric field and deposition time (Hamaker, 1940).

$$\frac{dY}{dt} = f \mu c E S \qquad \text{(Equation 4.1)}$$

where f is a dimensionless factor which takes into account will be eventually deposited ($f \leq 1$), μ is the electrophoretic mobility ($m^2/V/s$), c is the concentration of the powder in suspension (g/L), E is the electric field, S is the electrode surface area (m^2), t is the time (s), and Y is the yield in (g).

Figure 4.4 shows a graph of deposition mass against voltage applied. The amount of deposits increases in mass by increasing applied voltage from 10 to 50 V. Obviously, TiO_2 nanoparticles would deposit faster when a higher voltage is supplied and a directly proportional relation is formed. This is because much negative charge is allowed to attract nanoparticles towards cathode by electrostatic force when higher electric field is applied (Abdullah & Sorrell, 2008). Basically, two steps are involved in the process of EPD, which are (i) charge nanoparticles in the suspension migrate towards electrode under influence of electric field, and (ii) nanoparticles deposit on the electrode and thin film is formed (Kaya, Kaya, Su, Thomas, & Boccaccini, 2005).

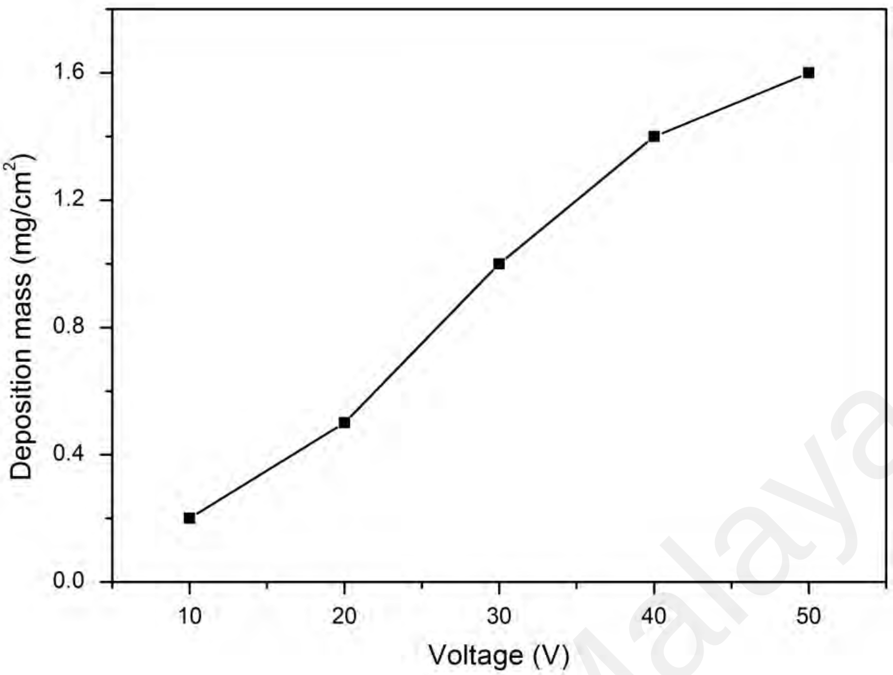

Figure 4.4: The deposition mass of nanocrystalline TiO_2 by EPD method at different electric field applied.

For their PEC water splitting performance evaluation, in order to gain insight into the correlation between the surface morphology of the nanocrystalline TiO_2 thin film and the properties of PEC water splitting, all samples were tested and used as the photoelectrode. Figure 4.5 shows the j_p-V curves of nanocrystalline TiO_2 deposited by using DC power supply in five different voltages, which are 10, 20, 30, 40 and 50 V. The photocurrent density reading was increased from 10 V to 20 V, which are 0.17 mA/cm^2 and 1.25 mA/cm^2 respectively. The photocurrent density peaked when 30 V is applied for EPD (2.12 mA/cm^2). Nonetheless, the further increment of deposition voltage makes the photocurrent density dropped.

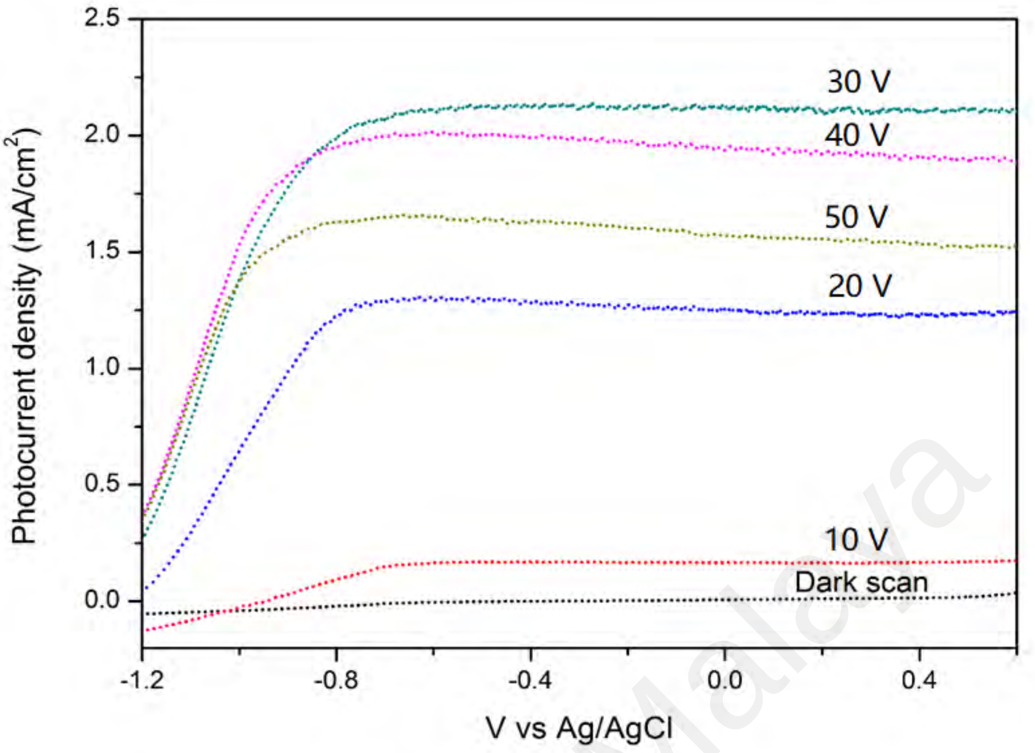

Figure 4.5: The j_p-V curves of nanocrystalline TiO_2 deposited at different electric field applied.

Formation of thin films on an electrode is a kinetic phenomenon and the packing behavior in the coating can be influenced by the deposition rate of nanoparticles (Basu, Randall, & Mayo, 2001). The photocurrent density trend in Figure 4.5 can be explained by when higher electric field applied, the rapid moving nanoparticles may have insufficient time to attach in a good position to form a thin film compactly. So, when 40 or 50 V was applied for deposition, which would cause the TiO_2 nanoparticles formed a thin film with loose packing structure as presented in Figure 4.6. Meanwhile, when a lower electric field is applied, TiO_2 nanoparticles able to form a closely packed thin film structure.

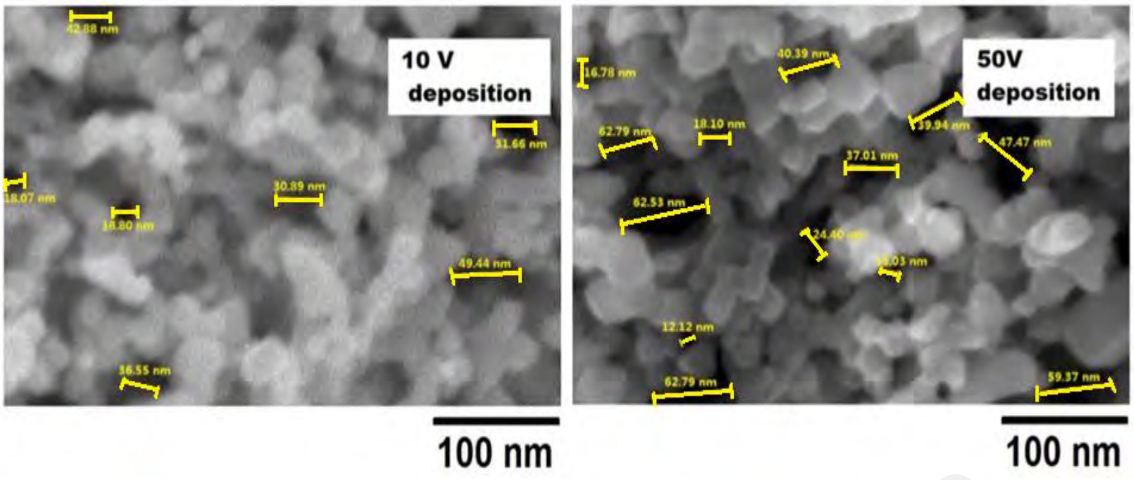

Figure 4.6: The TiO_2 nanoparticles arrangement at different electric field applied (FESEM analysis).

Figure 4.7 is a schematic diagram shows the electron flows pattern in both closely packed and loosely packed thin film structure. The voids and holes found in loosely packed structure gradually block the pathway of electron transport and it may lead to many electrons diffusion directions whereas closely packed structure gives a shorter average pathway before collection for photogenerated electrons (Liou *et al.*, 2011). This justifies the drop in the photocurrent density when 40 and 50 V of electric fields is used for TiO_2 nanoparticles deposition. Moreover, higher electric field applied can cause the turbulence in TiO_2 nanoparticles suspension and the coating might be interrupted by flows in the surrounding medium (Basu *et al.*, 2001). It was suggested that deposition by minimal voltage could improve the adherence and much denser packing as well (Kaya *et al.*, 2005) and maximal voltage (*e.g.* > 100 V) would result in rough thin films surface (Negishi, Yanagishita, & Yokokawa, 2002).

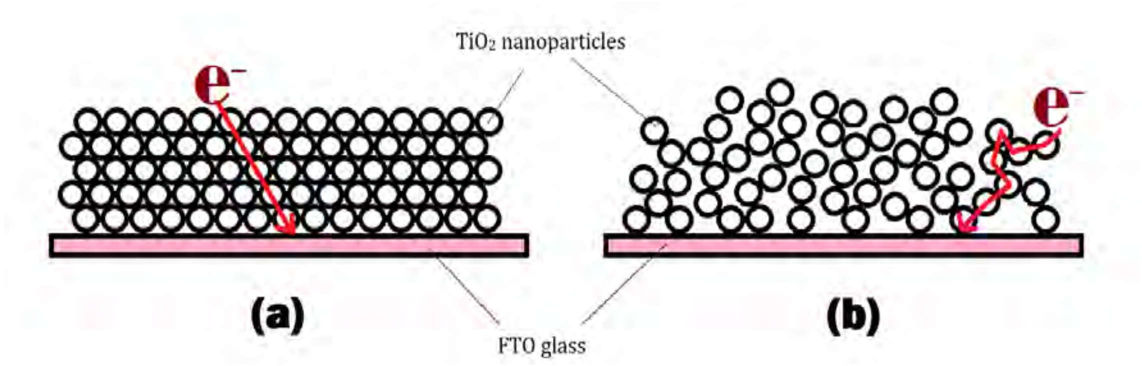

Figure 4.7: Schematic drawing the electron pathway of nanocrystalline TiO_2 on FTO glass in different packing density of the thin film, (a) closely packed structure, and (b) loosely packed structure.

4.1.4 Effect of Deposition Time

The effect deposition time of TiO_2 nanoparticles is discussed in this part of studies. In this manner, deposition time could significantly control the thickness of deposits. This study was investigated in four different deposition times, which are 30, 60, 120 and 180 s in a constant voltage of 30 V and 400 ^oC of heat treatment.

The thin film cross-section was analysed by FESEM. The thickness of nanocrystalline TiO_2 thin film becomes thicker according to the deposition time increase and formed a directly proportional relation as displayed in Figure 4.8. The figure 4.9 shows a graph of the thickness of the nanocrystalline TiO_2 thin film also and the photocurrent density in different time of deposition, respectively. Nanocrystalline TiO_2 thin film that deposited by 30 s with the thin film thickness of 6.7 µm produced only 0.45 mA/cm^2 of photocurrent density whereas thin film deposited by 60 s generated the best photocurrent density, which is 2.10 mA/cm^2 with the film thickness of 14.7 µm and this outcome is consistent with published data (Liou *et al.*, 2011). Meanwhile, the photocurrent density was dropped when the further increment of the film thickness in extended deposition time.

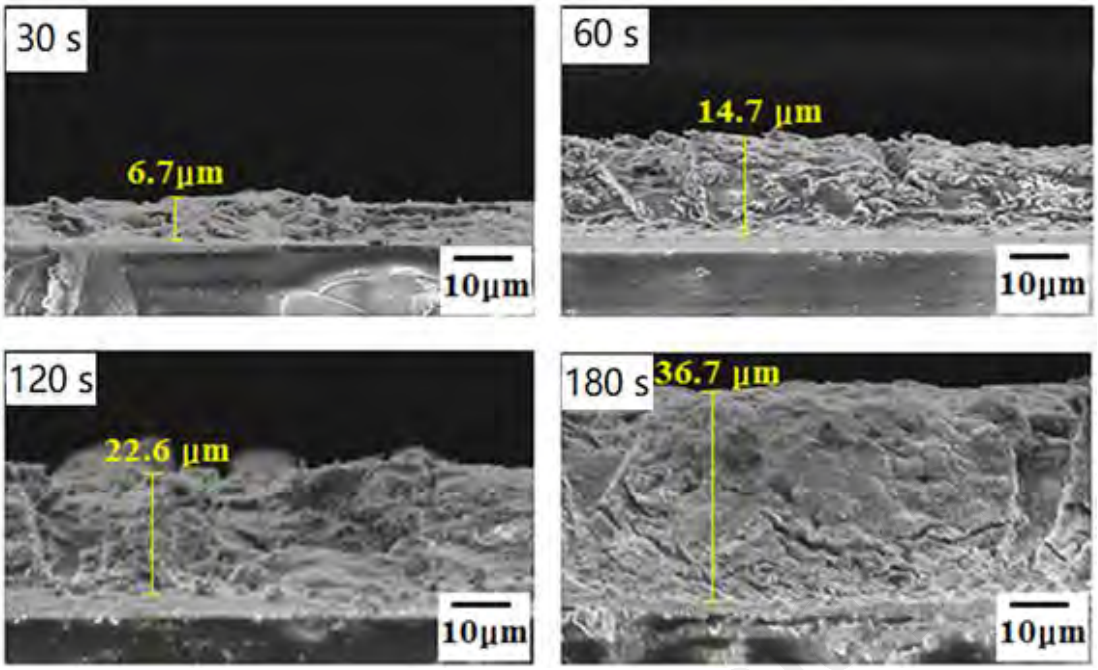

Figure 4.8: FESEM micrographs of electrophoretically deposited nanocrystalline TiO_2 on FTO glass in cross-section view.

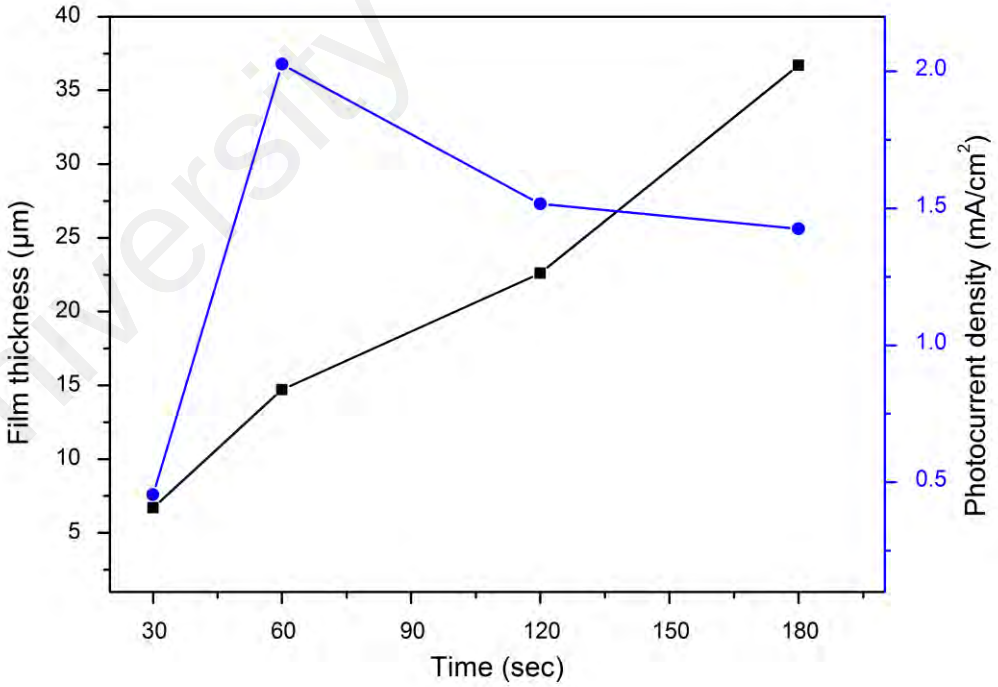

Figure 4.9: The nanocrystalline TiO_2 film thickness and photocurrent density produced at different deposition time.

Figure 4.10 displays the FESEM image of nanocrystalline TiO_2 thin film surface. The efficiency was dropped when the deposition was done by 120 s and 180 s, possibly because of the relatively weak interconnection of TiO_2 nanoparticles, such as cracks and voids which could bring effects to the electron transferring (Hsiao *et al.*, 2010). Based on Figure 4.10, more cracks were found on the surface of thin film when the thin film is getting thicker. Apart from that, solvent selection for electrophoretic suspension can be another factor of cracks formation. In this situation, IPA is an organic solvent that has high evaporation rate at room temperature and low boiling point. Thus, it could be vaporised easily under room temperature condition. Normally, cracks formed before heat treatment process, and these cracks could not be recovered by heat treatment process. On top of that, these cracks would influence the nanocrystalline TiO_2 thin film and FTO substrate adherence (Chang *et al.*, 2010). Therefore, it is not surprising that thin film deposited by 180 s has the most visible cracks and comes with a non-uniform surface. Since cracks affects the adhesion between the nanocrystalline TiO_2 thin film and FTO substrate, photocurrent density decreases when the deposition was done by 120 s and 180 s.

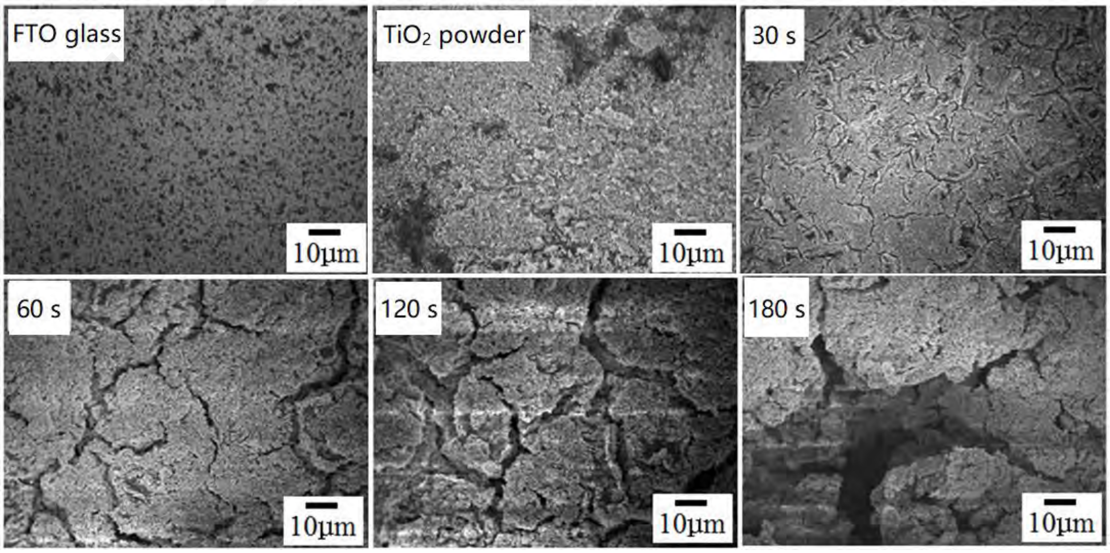

Figure 4.10: FESEM micrographs of electrophoretically deposited nanocrystalline TiO_2 thin film on FTO glass.

In addition, the nanocrystalline TiO_2 thin films that deposited at different time were analysed by XRD and the XRD diffractogram is shown in Figure 4.11. The conductive FTO glass with peaks at 2θ = 26.49, 33.74, and 51.56^{o} matched with JCDPS 01-077-0452 (SnO_2 structure). Based on XRD pattern of nanocrystalline TiO_2 thin films that deposited by 30, 60, 120, and 180 s, TiO_2 anatase peaks were found at 2θ = 25.31, 37.79, and 48.05^{o}, that is fitted well with JCPDS 01-071-1166. At the same time, rutile peaks were found at 2θ = 27.44, 54.32, and 69.01^{o}, that is fitted well with JCDPS 00-012-2176. According to these XRD patterns, there were no secondary phases determined and this indicates that nanocrystalline TiO_2 thin films were successfully formed on FTO glass.

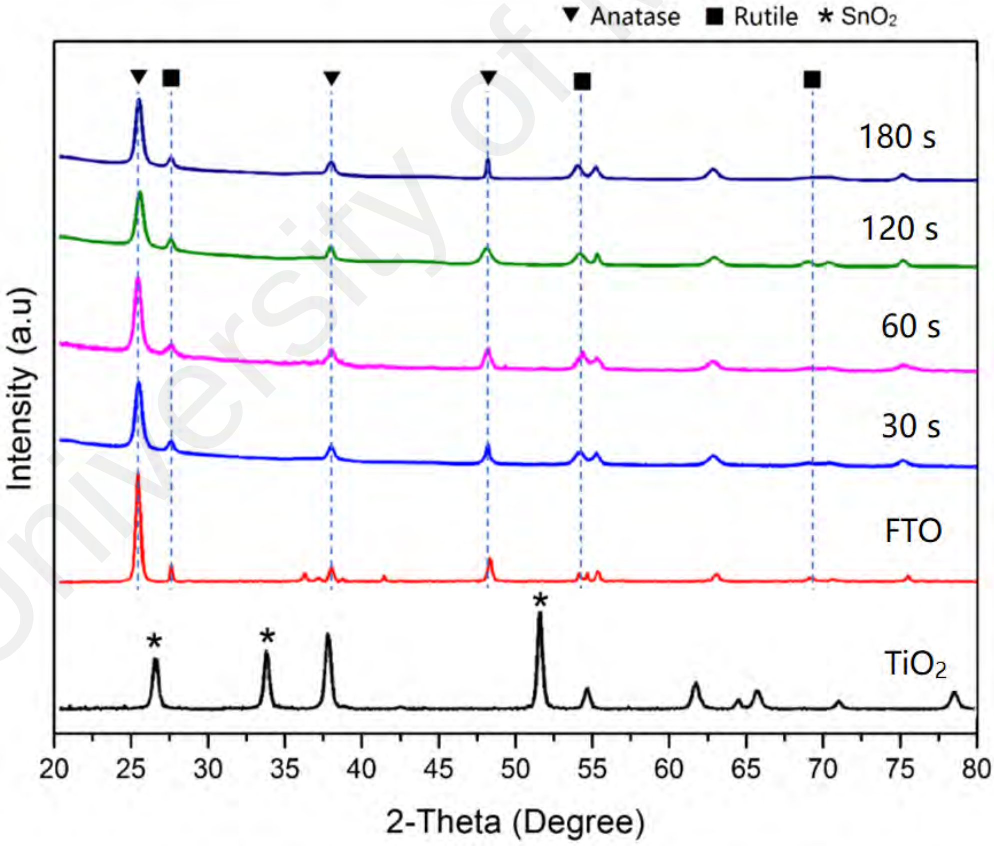

Figure 4.11: XRD patterns of nanocrystalline TiO_2 thin films that deposited at the different time.

4.1.5 PEC Water Splitting Performance

As the nanocrystalline TiO_2 thin film formation parameters were optimised in the previous section, this section will discuss the PEC water splitting efficiencies by analysing the PCE and the H_2 production rate of the optimised nanocrystalline TiO_2 photoelectrode.

4.1.5.1 Photoconversion Efficiency (PCE)

The PCE, η was determined to estimate the correlation of light absorption quantitatively. Figure 4.12 presents a graph of PCE in different nanocrystalline TiO_2 film thickness. It was found that the highest value was 2.49% for the film thickness of 14.7 µm whereas the lowest was about 0.56% for 6.7 µm of film thickness. The uniformity and thickness of nanocrystalline TiO_2 thin film affect the PCE of PEC water splitting. Besides that, a non-uniform thin film will cause recombination of charges and the PCE will be brought down (Bisquert, Zaban, Greenshtein, & Mora-Seró, 2004). As a result, it was found the optimum condition to fabricate nanocrystalline TiO_2 thin film by EPD to be 30 V of the electrical field applied, 60 s of deposition and 400 ^{o}C of post heat treatment in air.

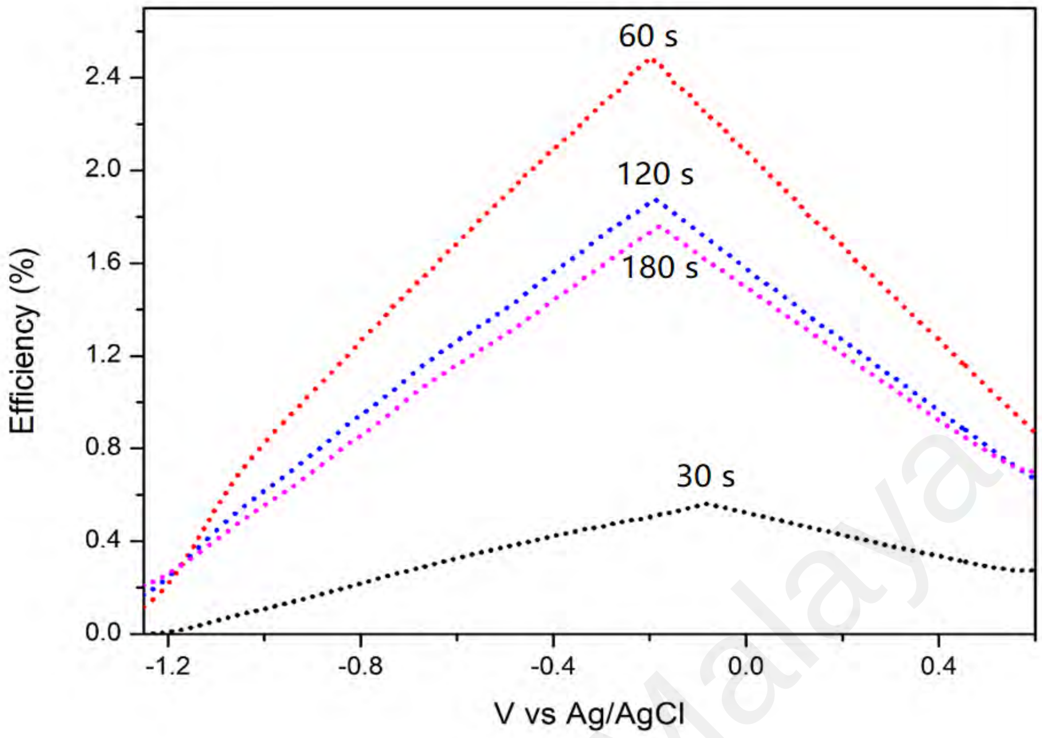

Figure 4.12: The calculated PCE of the nanocrystalline TiO_2 thin film at different deposition time.

4.1.5.2 Hydrogen Production

H_2 production is a crucial application for PEC water splitting. The H_2 evolution rate from the PEC water splitting process is examined as data collected from Figure 4.13. The reading was recorded in every 10 min and it gave a linear relation. By using a 1 cm^2 of photoelectrode, it was found 0.45 mL of H_2 evolved in an hour. Typically, in order to minimise the processing cost, photocatalyst potentially can be reused and several cycles were repeated to examine its recyclability. The H_2 production rate was maintained at about 0.40 mL cm^{-2} h^{-1} in the following cycles and can be reused up to five times.

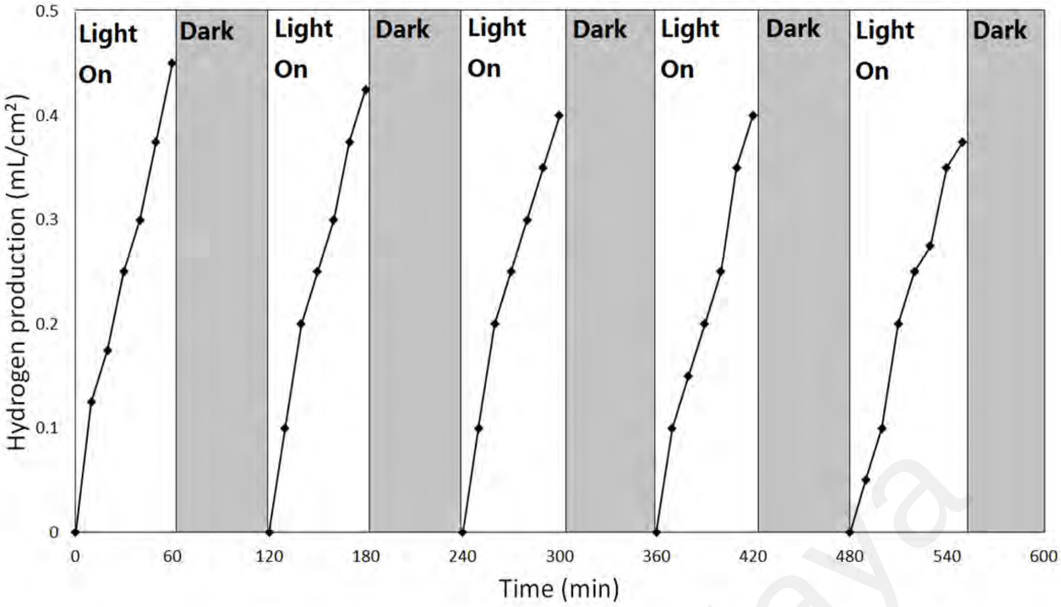

Figure 4.13: The hydrogen production under UV illumination at 0.6 V vs. Ag/AgCl in repeated cycles by using optimised nanocrystalline TiO_2 photoelectrode.

4.2 $SrTiO_3$ nanoparticles

4.2.1 Formation of $SrTiO_3$ Nanoparticles via Hydrothermal Reaction

$SrTiO_3$ nanoparticles were formed by hydrothermal reaction and several reaction temperatures were tested to optimise the best condition to synthesise a well-controlled morphology, uniform nanoparticle size, shape, good crystallinity, and purity. The properties of $SrTiO_3$ nanoparticles can be altered by different conditions, such as synthesis time (Zhang *et al.*, 2004) and temperature (Huang *et al.*, 2014). It was proposed that $SrTiO_3$ nanoparticles formation by hydrothermal synthesis is a dissolution-precipitation process (Ahn *et al.*, 2013). As a precursor, the TiO_2 powder was so stable that only dissolve under high alkalinity by breaking Ti-O bonds and to form a species that has high activity (Equation 4.2) that would react with Sr^{2+} and become $SrTiO_3$ (Equation 4.3). Equation 4.4 shows an overall reaction of the $SrTiO_3$

hydrothermal formation process. As the dissolution-precipitation process going on, TiO_2 precursor is dissolved gradually and more $SrTiO_3$ grains emerge until all of the TiO_2 are depleted. The small grains will then undergo crystal growth process and slowly to become large grains, and finally uniform $SrTiO_3$ nanoparticles are formed (Zhang *et al.*, 2015).

$TiO_2 + 2\ OH^- + H_2O \rightarrow [Ti(OH)_6]^{2-}$ (Equation 4.2)

$Sr^{2+} + [Ti(OH)_6]^{2-} \rightarrow SrTiO_3 + 3\ H_2O$ (Equation 4.3)

$TiO_2 + Sr(OH)_2.8H_2O \rightarrow SrTiO_3 + 9\ H_2O$ (Equation 4.4)

In this section, a few instrumentation analyses were done to study the morphology, chemical state, optical properties, and specific surface area of $SrTiO_3$ nanoparticles.

4.2.1.1 Phase Structure Analysis by XRD

An XRD analysis was done to determine the effects of the reaction temperature on the phase transition and crystallisation of the $SrTiO_3$ nanoparticles. The XRD patterns for commercial $SrTiO_3$ and synthesised $SrTiO_3$ samples are displayed as a graphical representation in Figure 4.14. It is evident that the patterns of commercial $SrTiO_3$ and $SrTiO_3$ synthesised at 90, 120, 150, and 180 °C showed the diffraction peaks and peak positions match well to the standard cubic perovskite $SrTiO_3$ (JCPDS 00-035-0734). The diffraction peaks of $SrTiO_3$ were detected at $2\theta = 22.75, 32.39, 40.00, 46.47, 52.35, 57.79, 67.82$, and 77.19° which corresponds to (100), (110), (111), (200), (210), (211), (220), and (310) planes, respectively. Also, the sharp peaks indicate the hydrothermal synthesised $SrTiO_3$ nanoparticles are in good crystallinity.

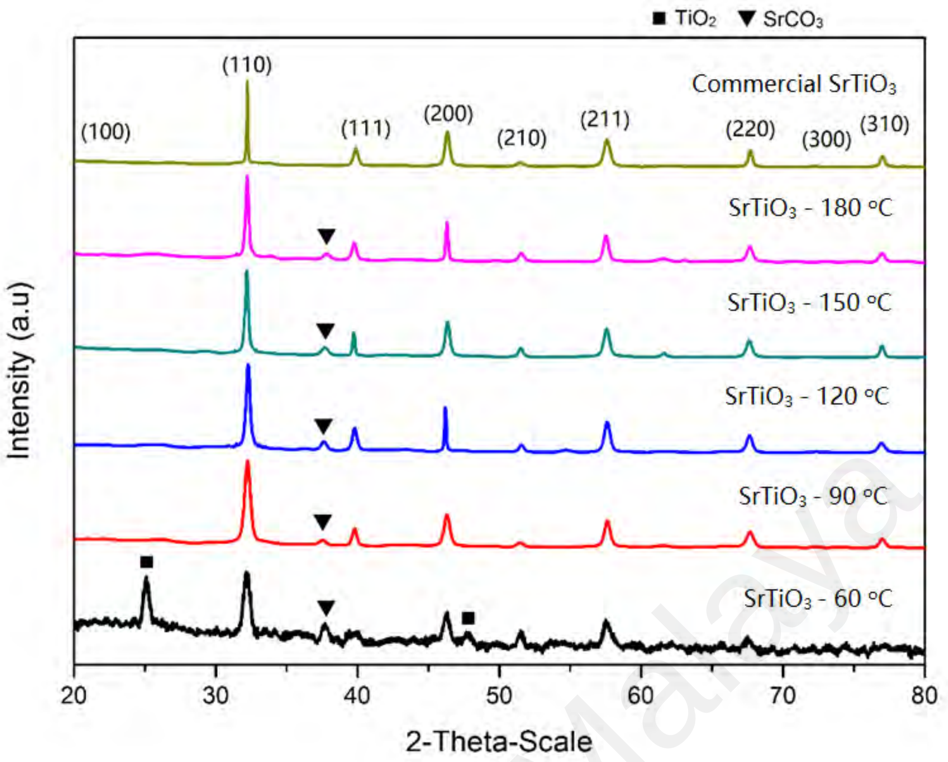

Figure 4.14: The XRD patterns for commercial $SrTiO_3$ and synthesised $SrTiO_3$ nanoparticles at the different hydrothermal reaction temperature.

Nevertheless, an orthorhombic $SrCO_3$ peak was observed in the XRD diffractogram at $2\theta = 36.65^o$ (JCPDS 00-005-0418) for all the hydrothermal synthesised $SrTiO_3$. This phenomenon was observed earlier by scientists that doing a similar synthesis by hydrothermal and solvothermal reaction (Huang *et al.*, 2014; Nakashima *et al.*, 2013; Souza *et al.*, 2012; Tsumura *et al.*, 2010; Wu *et al.*, 2015; S. Zhang *et al.*, 2004). It can be explained that during the process of pre-treatment and post-treatment, CO_2 in the air would dissolve in the mixture as CO_3^{2-} and undergo reactions with Sr^{2+} that originated from the precursor, that is $Sr(OH)_2.8H_2O$ (Equation 4.5 and 4.6). This reaction is favourable under alkaline conditions and thus causes the existence of $SrCO_3$ peak (Guo, Luo, Gao, Guo, & Yang, 2006; Huang *et al.*, 2014; Mourão *et al.*, 2015). In addition, $SrCO_3$ is a low solubility compound ($K_{sp} = 9.3 \times 10^{-10}$) and therefore it undergoes solid formation even though at low concentration of CO_2 (Douglas, 2004). Besides that, it was known that KOH is a good absorbent of CO_2 from the air. Also, the OH^- is a strong Lewis base, hence, the $SrCO_3$ arises from the effect of the OH^- (Yousefi *et al.*, 2015).

$CO_2\ (g) + H_2O\ (l) \rightleftharpoons 2\ H^+ + CO_3^{2-}\ (aq)$ (Equation 4.5)

$CO_3^{2-}\ (aq) + Sr^{2+} \rightleftharpoons SrCO_3\ (s)$ (Equation 4.6)

On the other hand, $SrTiO_3$ nanoparticles that synthesised by 60 °C shows a peak at $2\theta = 25.30$ and 48.05°, these peaks match well with JCPDS 01-071-1166, which is a TiO_2 anatase structure. At the same time, a $SrTiO_3$ major peak was found in the same diffractogram at $2\theta = 32.39°$, which is fitted well with JCPDS 00-035-0734. This might indicate that the hydrothermal reaction was incomplete and 60 °C is not a suitable hydrothermal temperature to synthesise $SrTiO_3$ nanoparticles due to insufficient of heat energy.

The crystallite size values were determined by estimating with Scherrer‘s equation (Equation 3.5) as shown in Table 4.1. According to the outcome, it shows a trend of increasing crystallite size when the hydrothermal reaction is increased. The smallest crystallite size was found in $SrTiO_3$ that hydrothermal reaction takes place at 60 °C (274 Å) whereas reaction at 180 °C shows a larger crystallite size, which is 550 Å. Commercial $SrTiO_3$ gives the largest crystallite size among, that is 1036 Å.

Table 4.1: The calculated crystallite size of commercial $SrTiO_3$ and hydrothermal synthesised $SrTiO_3$ at the different reaction temperature.

Samples	Average crystallite size*	Average nanoparticle size
	XRD (Å)	SEM (nm)
$SrTiO_3$ - 60 °C	274	30
$SrTiO_3$ - 90 °C	459	49
$SrTiO_3$ - 120 °C	487	49
$SrTiO_3$ - 150 °C	495	47
$SrTiO_3$ - 180 °C	550	56

Table 4.1 continued

Commercial $SrTiO_3$	1036	307

**Note: The XRD crystallite size obtained based on (110) plane.*

4.2.1.2 Morphological and Element Analysis by FESEM-EDX

A FESEM analysis was done to study the morphological of commercial $SrTiO_3$ and hydrothermal synthesised $SrTiO_3$ at different reactions temperature. Based on the FESEM micrographs displayed in Figure 4.15, it can be seen that the hydrothermal synthesised $SrTiO_3$ nanoparticles at 60 ^oC shows small nanoparticles but in non-uniform sizes. This is due to the hydrothermal reaction was incomplete as discussed in the previous section. $SrTiO_3$ synthesised at 90 and 120 ^oC shows a mixture of spherical nanoparticles and nanoparticles in cubic shape (nanocubes) but in non-uniform nanoparticle sizes. For $SrTiO_3$ nanoparticles synthesised at 150 and 180 ^oC, all nanoparticles show in regular size and nanocube shapes. Yet, $SrTiO_3$ synthesised at 180 ^oC produced a slightly larger nanoparticle sizes. As refer to Table 4.1, the diameter of $SrTiO_3$ nanoparticles synthesised at 180 ^oC was about 56 nm, which is the largest among all hydrothermal synthesised $SrTiO_3$. This indicates that the increase in the $SrTiO_3$ nanoparticles size because the increase in reaction temperature and that may also explained at higher synthesis temperature, agglomeration might occur (Huang *et al.*, 2014). Then, commercial $SrTiO_3$ shows all the particles cluster together and an agglomeration occurred.

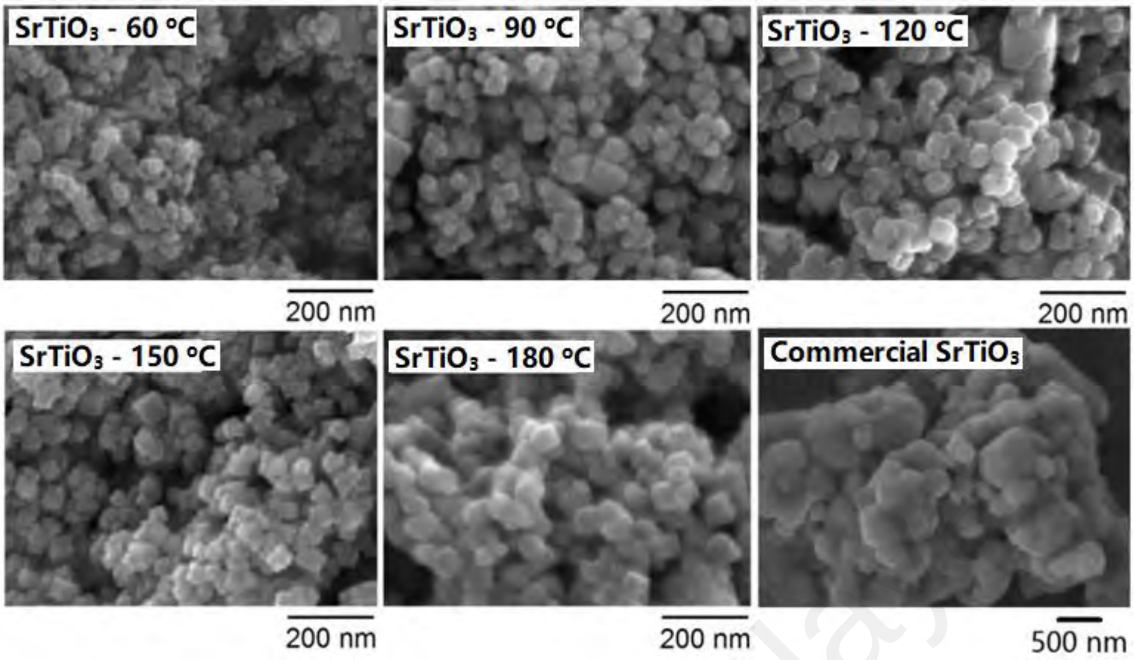

Figure 4.15: The FESEM micrographs of commercial $SrTiO_3$ and hydrothermal synthesised $SrTiO_3$ at different reactions temperature.

Figure 4.16 presents the histogram of hydrothermal synthesised $SrTiO_3$ nanoparticles size distribution that corresponding to FESEM micrographs that presented in Figure 4.15. $SrTiO_3$ nanoparticles that hydrothermal synthesised at 90 ^{o}C shows a broad peak which indicates a wide nanoparticles size distribution (non-uniform). Meanwhile for $SrTiO_3$ that hydrothermal synthesised at 150 ^{o}C indicates a narrow nanoparticles size distribution (uniform and regular). The diameter of each $SrTiO_3$ nanoparticle samples was measured and tabulated in Table 4.1. The nanoparticles size of synthesised $SrTiO_3$ was in the range of 30 to 56 nm. It was obvious that $SrTiO_3$ nanoparticles that synthesised at 150 ^{o}C show distinct nanocubes with narrow nanoparticle size distribution under 150 ^{o}C for 72 h.

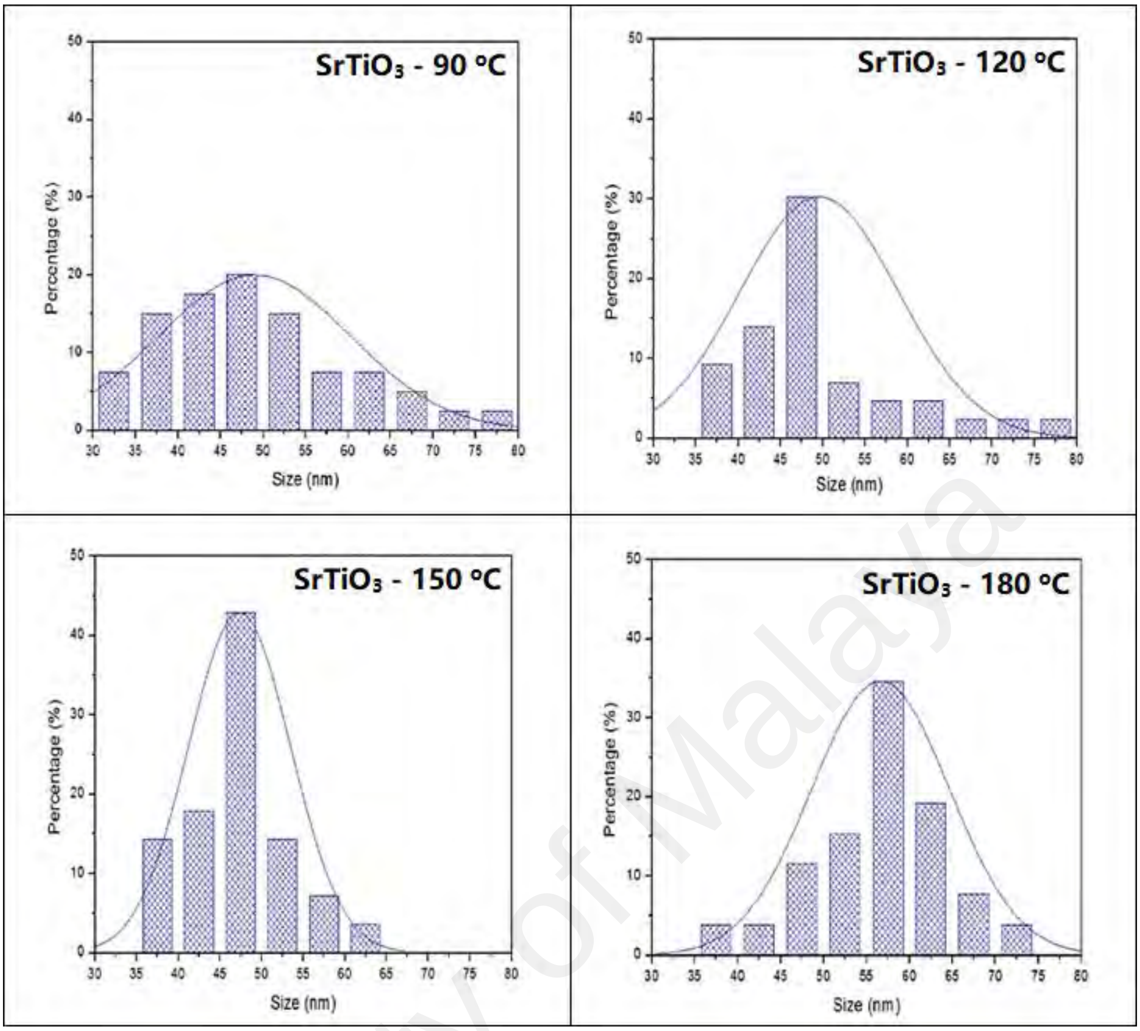

Figure 4.16: The nanoparticles size distribution of hydrothermal synthesised $SrTiO_3$ at different reactions temperature.

An elemental analysis was done by EDX to observe the surface region of commercial $SrTiO_3$ and hydrothermal synthesised $SrTiO_3$ at different reactions temperature. The EDX spectrum of commercial $SrTiO_3$ and hydrothermal synthesised $SrTiO_3$ at different reactions temperature were presented in *Appendix A* to *F*. The atomic ratio of the surface region of all $SrTiO_3$ nanoparticle samples was tabulated in Table 4.2. Commercial $SrTiO_3$ and hydrothermal synthesised $SrTiO_3$ nanoparticles at 90, 120, 150 and 180 ^{o}C show an atomic ratio that well matched with model compound and preparative stoichiometry. This reveals that the atomic percentage (at %) of Sr, Ti, and O in the samples basically concordance with the designed compositions and confirmed to the high purity of the prepared sample. In the meantime, $SrTiO_3$ nanoparticles that synthesised at 60 °C was a slightly different stoichiometric ratio of elements, which are Sr (6.86%), Ti (22.03%) and O (71.11%). This can be predicted that there are still remain some unreacted precursor (TiO_2) in the sample since the hydrothermal reaction was not complete as discussed in the previous section.

Table 4.2: The atomic ratio of the surface region of commercial $SrTiO_3$ and hydrothermal synthesised $SrTiO_3$ nanoparticles at different reactions temperature.

Samples	Element atomic ratio (at %)		
	Sr	Ti	O
TiO_2 (precursor)	N/A	34.35	65.65
$SrTiO_3$ - 60 °C	6.86	22.03	71.11
$SrTiO_3$ - 90 °C	19.11	17.62	63.26
$SrTiO_3$ - 120 °C	18.68	17.62	63.70
$SrTiO_3$ - 150 °C	18.38	18.42	63.20
$SrTiO_3$ - 180 °C	18.94	18.75	62.31
Commercial $SrTiO_3$	18.87	18.47	62.67

4.2.1.3 Optical Properties Analysis by UV-DRS

The optical band gap of hydrothermal synthesised $SrTiO_3$ nanoparticles and commercial $SrTiO_3$ were calculated using KM function (Equation 3.6). Figure 4.17 presents a graph of square root *αhv* against band gap energy (*eV*). The band gap was estimated by extrapolating the slope to the x-axis. Based on the outcomes, the E_g of hydrothermal all synthesised $SrTiO_3$ nanoparticles and commercial $SrTiO_3$ was determined to be approximately 3.01 eV and 3.10 eV, respectively. By substituting the E_g value to Equation 4.8 (originally derived from Equation 4.7), it can be known that the photocatalytic properties of $SrTiO_3$ nanoparticles exist in UV region.

$$E = \frac{hc}{\lambda} \qquad \text{(Equation 4.7)}$$

$$E = \frac{(1.987\ x\ 10^{-25})}{\lambda} J$$

$$E = \frac{1.987\ x\ 10^{-25}}{1.602\ x\ 10^{-19}\ \lambda}$$

$$E = \frac{1.240\ x\ 10^{-6}}{\lambda}$$

$$\lambda = \frac{1.240\ x\ 10^{-6}}{E} \qquad \text{(Equation 4.8)}$$

where E is the energy band gap (eV), h is the Planck‘s constant (6.626 x 10^{-34} J s), c is the speed of light (3.00 x 10^{8} m s^{-1}), and λ is the wavelength of the light (m).

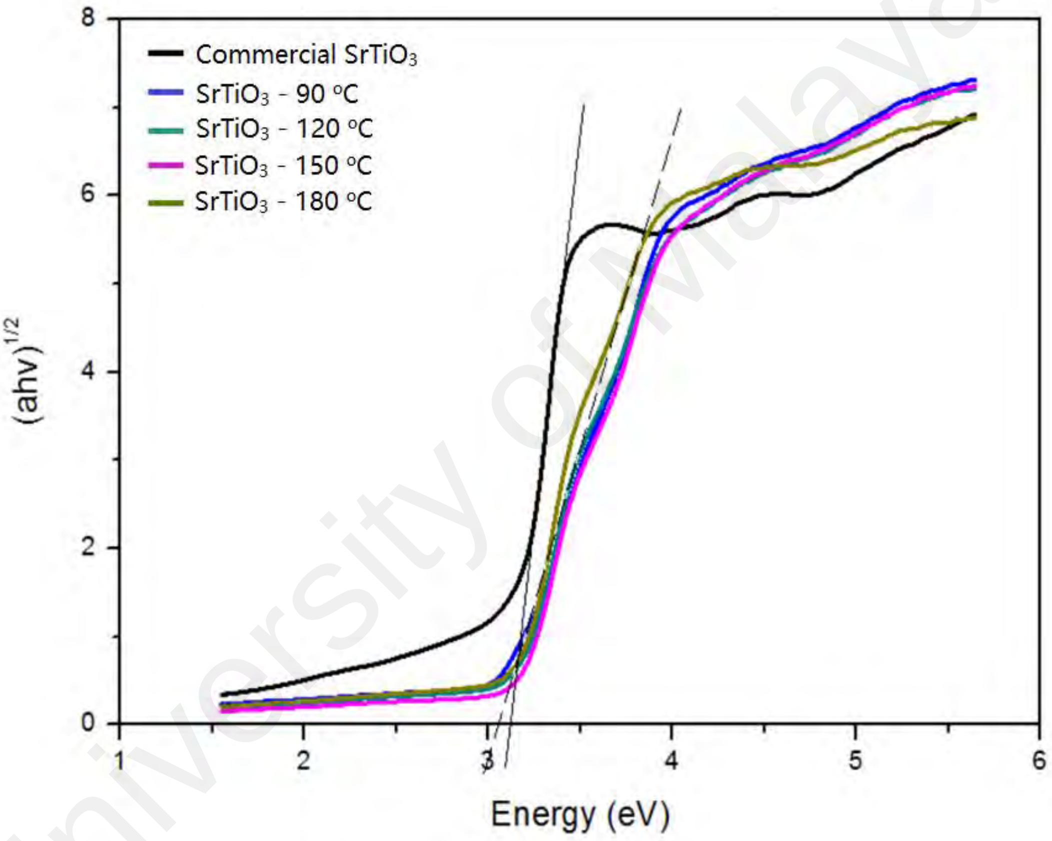

Figure 4.17: The UV-DRS of commercial $SrTiO_3$ and hydrothermal synthesised $SrTiO_3$ at different reactions temperature.

The E_g values of $SrTiO_3$ nanoparticles shows no significant changes in different reactions temperature but it shows slightly lower band gap energy than commercial $SrTiO_3$ in this study. It was reported that the band gap energy of $SrTiO_3$ nanoparticles could be slightly different when different processing details and sample preparation method was used (Huang *et al.*, 2014). The band gap of $SrTiO_3$ nanoparticles was found to be nearly 3.10 eV by conventional SSR (Liu *et al.*, 2008) and hydrothermal synthesis (Huang *et al.*, 2014). Also, it was reported by a researcher that $SrTiO_3$ nanoparticle was synthesised by SSR with ball milling assisted, the band gap is about 2.00 eV, which is photoactive in the visible region (Liu *et al.*, 2008). It was noticed metal impurities were found in $SrTiO_3$ lattice structure and this impurity was suspected alter the E_g value of the sample (Liu *et al.*, 2008). The $SrTiO_3$ nanoparticle was estimated to be 3.35 eV when co-precipitation synthesis was used (Chen & Chen, 2011) and about some researchers was synthesised $SrTiO_3$ nanoparticles with E_g value of 3.40 to 3.60 eV (Souza *et al.*, 2012).

4.2.1.4 Carrier Recombination Analysis by PL Spectroscopy

PL emission is the result of the recombination of free carriers. PL emission spectrum is a powerful tool that can be applied to determine the efficiency of charge carrier trapping by understanding the fate of e^- and h^+ in a semiconductor. PL spectra can explain the transfer rate of photogenerated e^- and h^+, immigration, and charge carrier trapping efficiency. The origin of luminescence is assigned to the STE formed in between the CB and VB of the $SrTiO_3$ nanoparticles (Jayabal *et al.*, 2014). Figure 4.18 shows the PL spectrum with the wavelength range of 350 to 750 nm of commercial $SrTiO_3$ and hydrothermal synthesised $SrTiO_3$ nanoparticles at different reactions temperature conducted at the excitation wavelength at 325 nm. Commercial $SrTiO_3$ produced the highest peak and this indicates that the e^--h^+ pairs have high recombination. A visible emission and the emission peak cantered at 510 nm are due to the recombination of STEs. Meanwhile, the intensity of $SrTiO_3$ nanoparticles that synthesised at 90, 120, 150 and 180 ^{o}C gradually decreased upon increased synthesis temperatures. $SrTiO_3$ nanoparticles that synthesised at 150 ^{o}C shows the lowest PL intensity and this demonstrated that slowest recombination occurred in which the electron was greatly restrained. This may be due to small particle size can affect the recombination rate and it has been reported earlier (Amano, Ishinaga, & Yamakata, 2013).

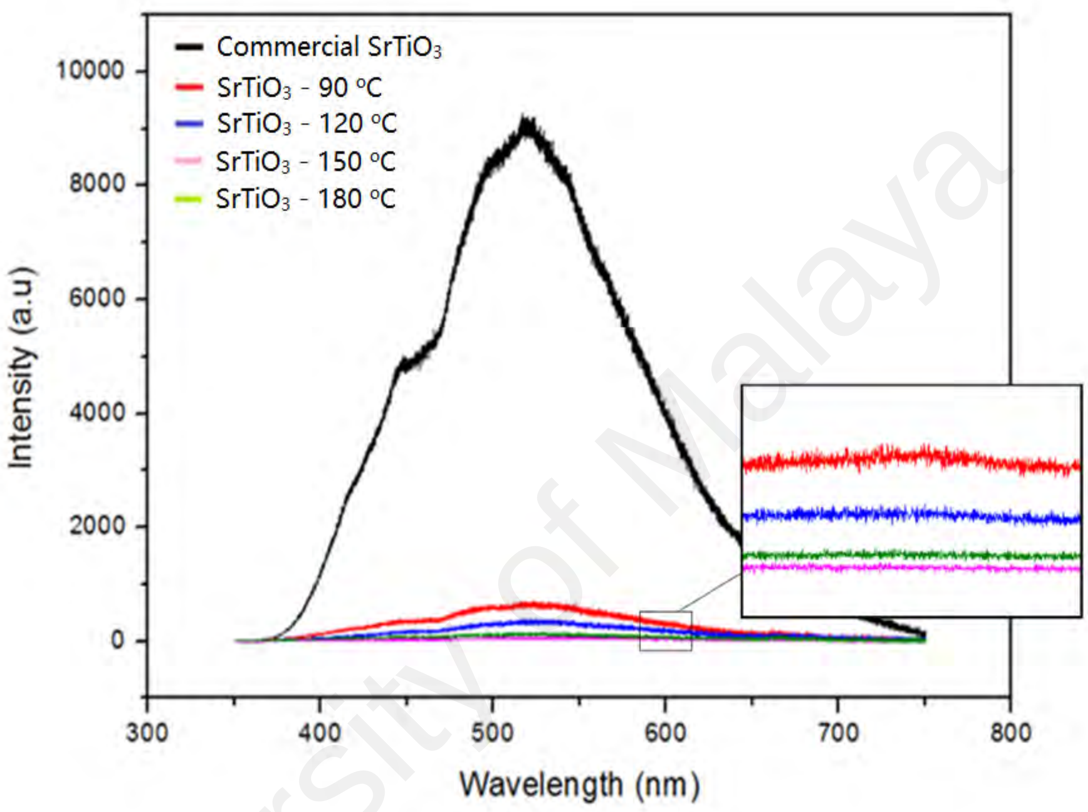

Figure 4.18: The PL spectrum of commercial $SrTiO_3$ and hydrothermal synthesised $SrTiO_3$ nanoparticles at different reactions temperature.

4.2.1.5 Specific Surface Area Analysis by BET

The BET analysis was applied to investigate the specific surface area of $SrTiO_3$ nanoparticle samples. Table 4.3 presents the specific surface area of commercial $SrTiO_3$ and hydrothermal synthesised $SrTiO_3$ at different reactions temperature. It was found that $SrTiO_3$ nanoparticles that synthesised at 150 °C give the largest surface area, which is 17.00 m^2/g. The surface area of $SrTiO_3$ nanoparticles was dropped when further increases the synthesis temperature to 180 °C. As discussed earlier in section 4.2.1.2, $SrTiO_3$ nanoparticles that synthesised at 180 °C shows a larger nanoparticles diameter compared to $SrTiO_3$ nanoparticles that synthesised at 150 °C. This can explain by small particles would have larger surface area per volume whereas the large particles might have smaller surface area and less active site. Besides that, $SrTiO_3$ nanoparticles that synthesised at 150 °C show about 12 times greater specific surface area than commercial $SrTiO_3$, which only 1.38 m^2/g. This is because agglomeration and large particle size (*ca.* 1 µm) was determined for commercial $SrTiO_3$.

Table 4.3: The specific surface area of commercial $SrTiO_3$ and hydrothermal synthesised $SrTiO_3$ at different reactions temperature.

Samples	BET specific surface area (m^2/g)
$SrTiO_3$ – 90 °C	14.65
$SrTiO_3$ – 120 °C	15.60
$SrTiO_3$ – 150 °C	17.00
$SrTiO_3$ – 180 °C	15.43
Commercial $SrTiO_3$	1.38

Basically, the size of $SrTiO_3$ nanoparticles is one of the key factors on the photocatalytic activities due to the active sites available, the variation of surface area, and so on. Figure 4.19 presents the j_p-V curves of commercial and hydrothermal synthesised $SrTiO_3$ at different reactions temperatures in a constant photoelectrode deposition condition by EPD method (35 V of electric field applied and 60 s of deposition). The photocurrent density was found to be increased when the $SrTiO_3$ nanoparticles synthesis temperature increased from 90 °C to 150 °C. $SrTiO_3$ nanoparticles that synthesised at 150 °C generated the highest photocurrent, which is (0.65 mA/cm^2). The photocurrent was dropped when further increase the synthesis temperature to 180 °C. Commercial $SrTiO_3$ shows the lowest efficiency, which approximately 0.01 mA/cm^2 was produced.

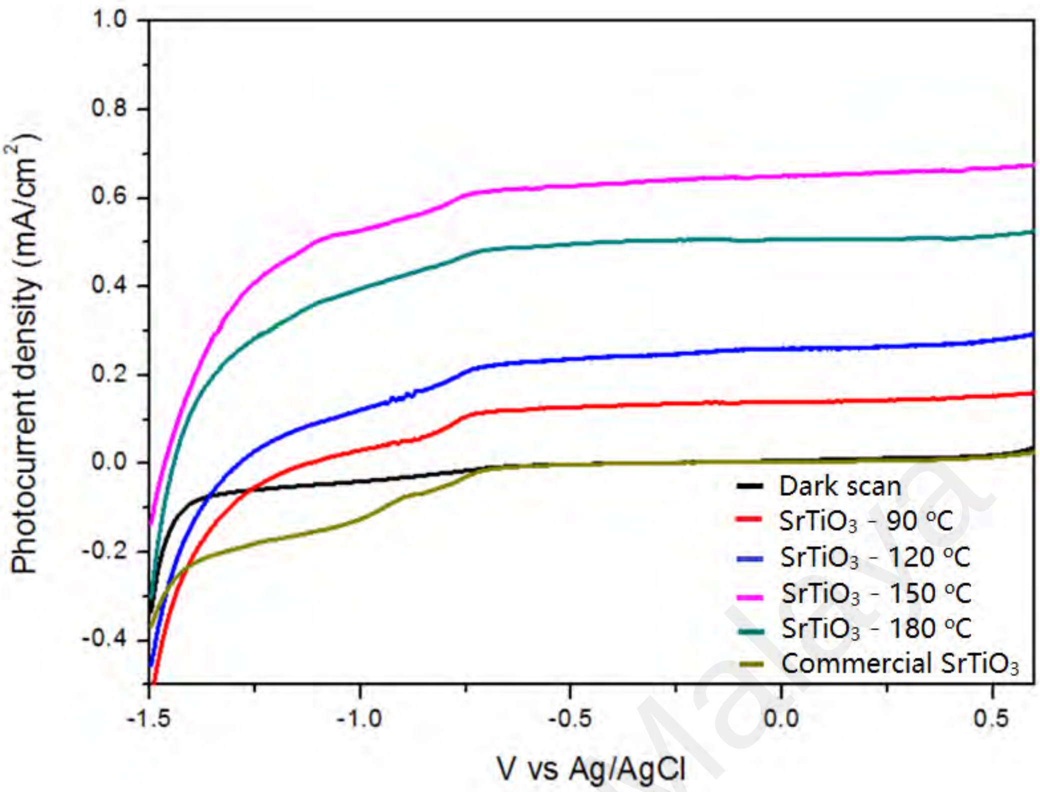

Figure 4.19: The j_p-V curves of commercial and hydrothermal synthesised SrTiO$_3$ at different reactions temperatures (Deposition condition: 35 V and 60 s).

4.2.2 Formation of SrTiO$_3$ Thin Film Coatings by EPD

According to the discussion in section 4.2.1, it was found that SrTiO$_3$ nanoparticles that synthesised at 150 ^{o}C shows a good morphology, uniform nanoparticle size, good purity as well as generated the highest photocurrent among all SrTiO$_3$ samples. Thus, SrTiO$_3$ nanoparticles that synthesised at 150 ^{o}C will be further discuss in this section by optimising the best condition of thin film formation for PEC water splitting photoelectrode purpose. Factors that influencing EPD can be categories into two parts, which are parameters related to the suspension and parameters related to the deposition process. In this section, the colloidal stability of SrTiO$_3$ suspension, effect of electric field applied for deposition and effect of deposition time will be discussed.

4.2.2.1 Colloidal Stability Analysis by ZP

One of the crucial parameters that involved in all flows of electrokinetic is ZP. Based on Helmholtz double-layer structure, it is the potential that isolates the bulk fluid from the boundary layer fluid at the slip plane (Lyklema, 1977). This develops charges at the slip plane between the boundary of nanoparticles and a liquid medium with the applied of DC lead to the electrophoretically mobility. When $SrTiO_3$ nanoparticles dispersed in the organic solvent or water, the addition of electrolytes helps to increase the stability of $SrTiO_3$ nanoparticles suspension. The electrophoretic mobility of $SrTiO_3$ nanoparticles value in IPA was measured as a function of the $Mg(NO_3)_2.6H_2O$ molarity. The ZP can be calculated by substituting electrophoretic mobility value to Helmholtz-Smoluchowski equation (Equation 4.9).

$$\mu = \frac{\varepsilon_o \varepsilon_r \zeta}{\eta} \qquad \text{(Equation 4.9)}$$

where μ is the mobility of the nanoparticles, ε_o is the permittivity of vacuum ($F\ m^{-1}$), ε_r is the dielectric constant of the medium, ζ is the zeta potential of the nanoparticles, and η is the viscosity of the solvent.

Figure 4.20 presents the concentration of $Mg(NO_3)_2.6H_2O$ salt act as a function of ZP of the $SrTiO_3$ nanoparticles in the IPA. The value of ZP was going up when the concentration of Mg salt increased from 10^{-5} to 10^{-4} M. The ZP value shows the highest when 10^{-4} M of Mg salt was added to the $SrTiO_3$ nanoparticles suspension. The ZP value was dropped when further increases the Mg salt concentration to 10^{-3}, 10^{-2} and 10^{-1} M.

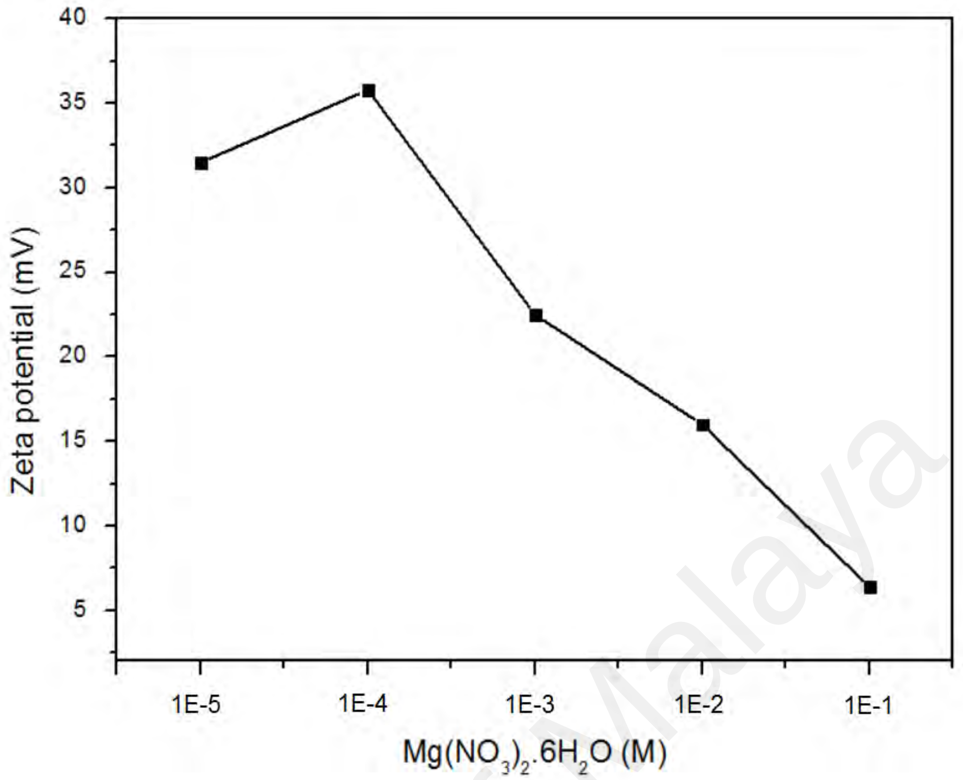

Figure 4.20: The ZP for SrTiO$_3$ nanoparticles as a function of the concentration of Mg salt in the IPA.

Since the surface of SrTiO$_3$ nanoparticles is saturated for ion adsorption and generates correspondingly more counter ions in diffuse layer, as a result, continue to increase the concentration of Mg salt would bring down the value of ZP. In the meantime, this makes the SrTiO$_3$ nanoparticles net force to become attractive. This could lead to certain flocculation and coagulation and finally sedimentation occurs because the EDL for SrTiO$_3$ nanoparticles is compressed and van der Waals forces became predominant. A SrTiO$_3$ nanoparticle suspension that stable will show no tendency to flocculate but settle slowly and form dense and strongly adhering deposits at the bottom of the beaker. Meanwhile, flocculating suspensions will settle faster and form low density and weakly adhering deposits (Besra & Liu, 2007). A similar phenomenon was reported by researcher and it is in agreement with published data (Chang *et al.*, 2010; Yum *et al.*, 2005).

4.2.2.2 Effect of Electric Field Applied

The electric field applied for $SrTiO_3$ nanoparticles deposition is discussed in this study. Figure 4.21 shows the j_p-V curves of $SrTiO_3$ nanoparticles deposited as the thin film at different applied voltages. It was found that the photocurrent gradually increases from 0.17 mA/cm^2 to 0.44 mA/cm^2 when 10 V to 30 V of electric field was applied for $SrTiO_3$ nanoparticles deposition. $SrTiO_3$ nanoparticles deposited by 40 V generate the highest photocurrent, which is 0.71 mA/cm^2 but the value was dropped to 0.60 mA/cm^2 when further increase the voltage to 50 V.

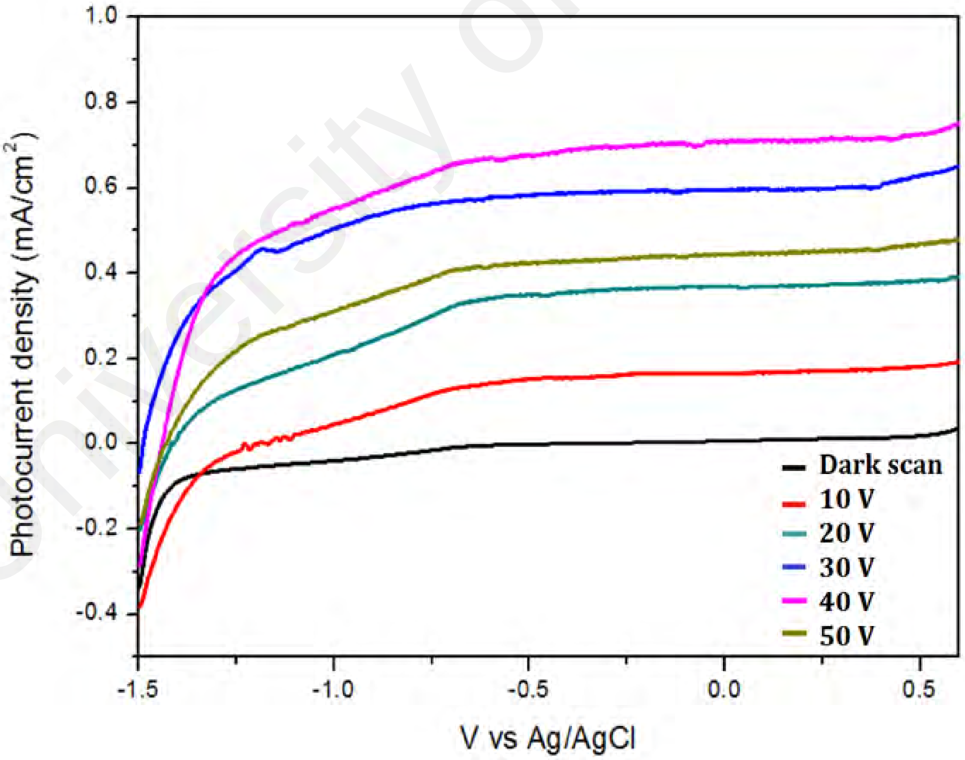

Figure 4.21: The j_p-V curves of $SrTiO_3$ nanoparticles deposited as the thin film at different applied voltages (Deposition time was fixed at 60 s).

Figure 4.22 shows a graph of the deposition mass against the electric field applied. Normally, the deposit amount increases with increase in deposition voltage and this explained the photocurrent increases from 10 V to 40 V due to more photoactive $SrTiO_3$ nanoparticles and more active sites available (Besra & Liu, 2007) and this explained why the thin film deposited by 40 V has generated better photocurrent than 10 V. However, under high deposition voltage, $SrTiO_3$ nanoparticles managed to deposit more quickly but the quality of thin film may deteriorate (Basu *et al.*, 2001). This is because the $SrTiO_3$ nanoparticles are moving faster and attaching faster towards the electrode when a higher voltage is applied. Then, the deposition rate can affect the packing behaviour of thin film.

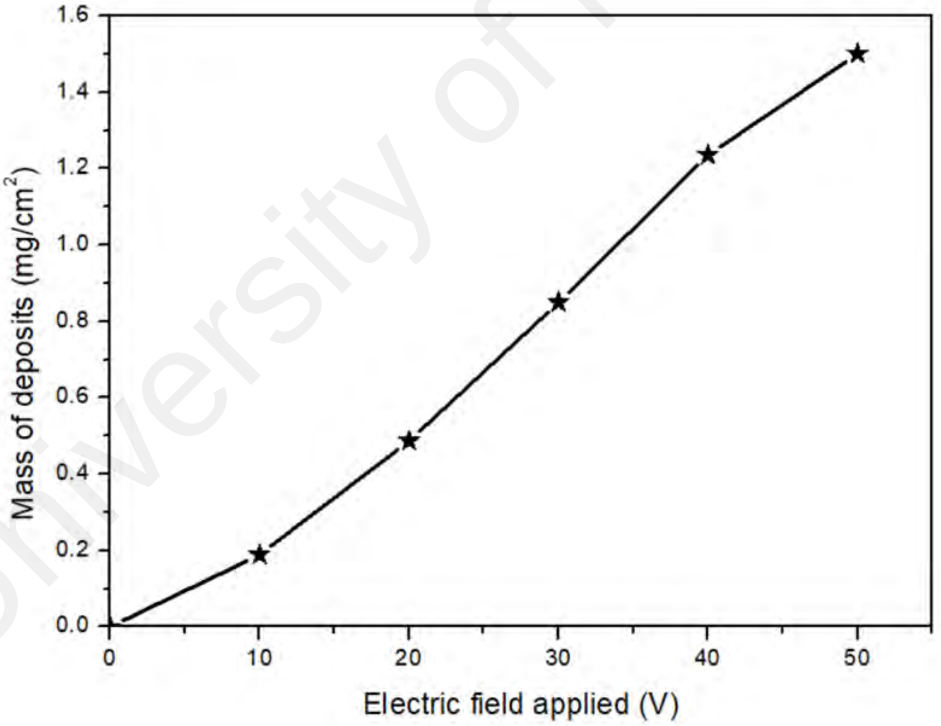

Figure 4.22: The deposition mass of $SrTiO_3$ nanoparticles on FTO substrate by EPD method in the different electric field applied.

In Figure 4.23, the 10 V deposition shows a more compact arrangement compared to 50 V of deposition under FESEM analysis. For 50 V deposits, numerous of holes and voids appeared on the thin film surface. This is because when 50 V of the electric field applied, $SrTiO_3$ nanoparticles that move faster might have insufficient time to –sit” in a good position and thus the nanoparticles and therefore, is unable to arrange methodically (Liou *et al.*, 2011; Phoon *et al.*, 2017). This explained why the thin film that deposited by 50 V will drop in photocurrent. This may form a rough surface and loose packing thin film structure that can cause the electron flows pathway is obstructed (Basu *et al.*, 2001; Chen & Liu, 2001). Moreover, Figure 4.24 illustrates the electron flow pattern in both tightly packed and loosely packed structure of $SrTiO_3$ nanoparticles thin film when the PEC water splitting takes place. Obviously, the voids and holes were found in loosely packed structure potential to block the electron transport pathway may cause electron diffusion (Hsiao & Teng, 2009).

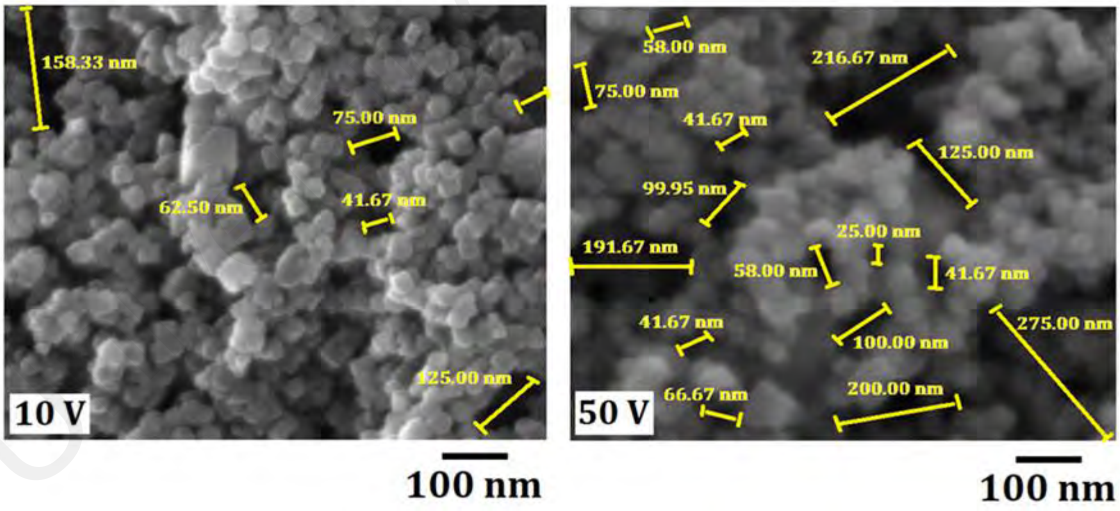

Figure 4.23: The FESEM analysis of $SrTiO_3$ nanoparticles arrangement on FTO glass.

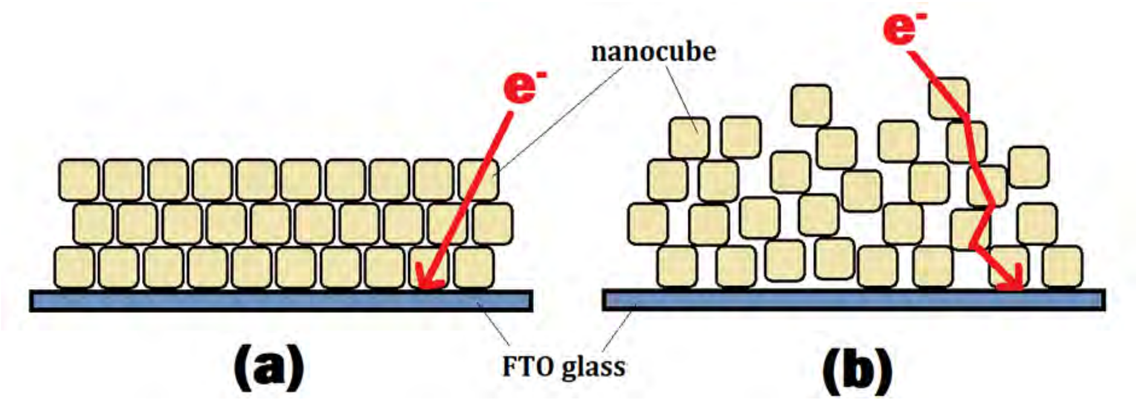

Figure 4.24: Schematic diagram showing the electron pathway of $SrTiO_3$ nanoparticles on FTO glass in different packing density of thin film (a) closely packed, and (b) loosely packed.

4.2.2.3 Effect of Deposition Time

The deposition time of thin film able to control the thickness of $SrTiO_3$ nanoparticles deposited on FTO substrate. Figure 4.25 shows the j_p-V curves of $SrTiO_3$ nanoparticles deposited as the thin film at different deposition time. The photocurrent density increased from 0.54 mA/cm^2 to 0.66 mA/cm^2 when the deposition time prolonged from 30 s to 60 s. The photocurrent reached the maximum when 120 s of deposition time was applied (1.05 mA/cm^2) but a slight dropped was found when 180 s of deposition was applied (0.80 mA/cm^2).

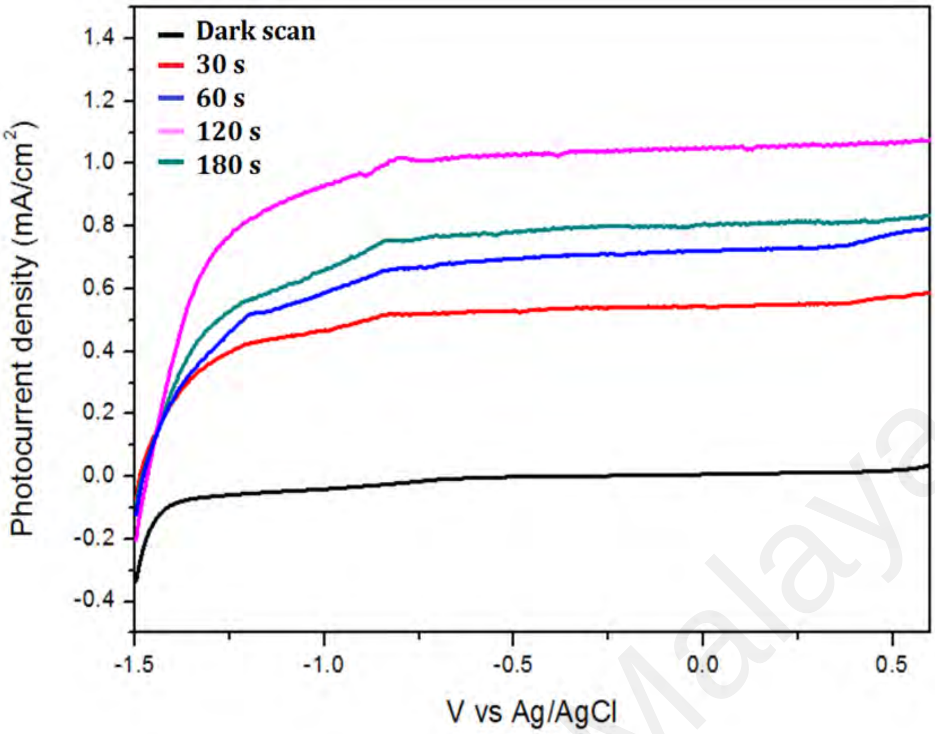

Figure 4.25: The j_p-V curves of $SrTiO_3$ nanoparticles deposited as the thin film at different deposition time (Deposition voltage was fixed at 40 V).

Figure 4.26 presents the FESEM micrograph in cross-section view of electrophoretically deposited $SrTiO_3$ nanoparticles on FTO substrate and it is clearly show that the deposition thickness is linear relationship with the deposition time (Figure 4.27). As a result, based on these outcomes, $SrTiO_3$ nanoparticles deposited by 120 s with film thickness of 18.8 µm shows the best photocurrent density and this outcome is consistent with researcher published data (Hsiao & Teng, 2009).

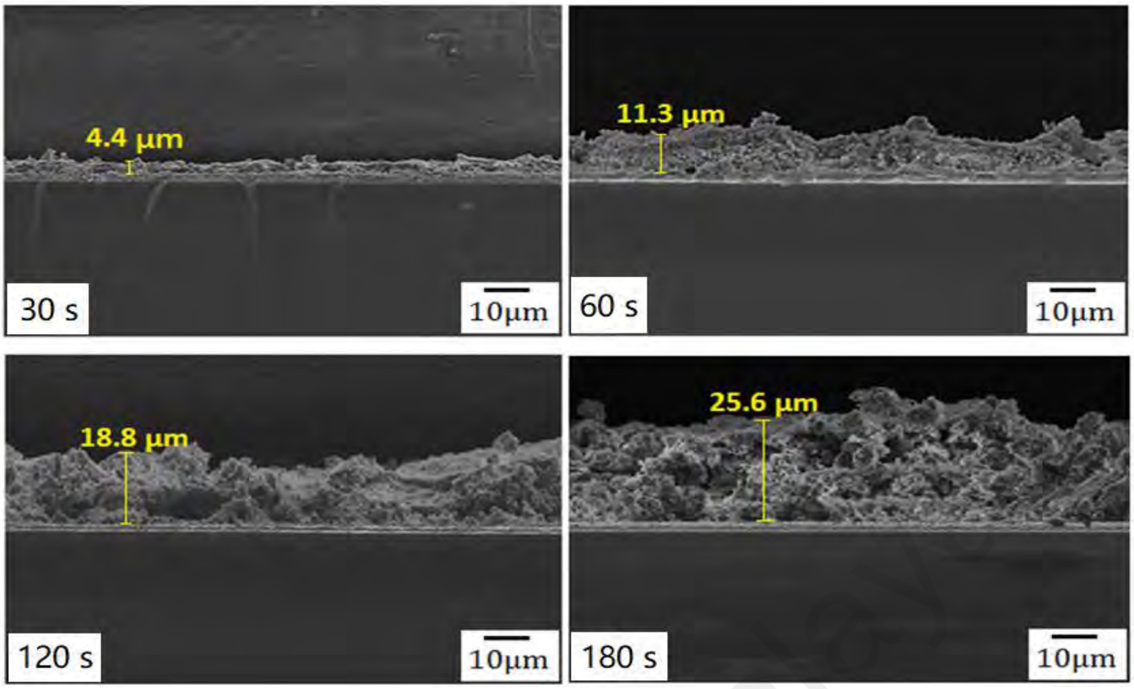

Figure 4.26: The FESEM micrograph in the cross-section view of electrophoretically deposited $SrTiO_3$ nanoparticles on FTO substrate.

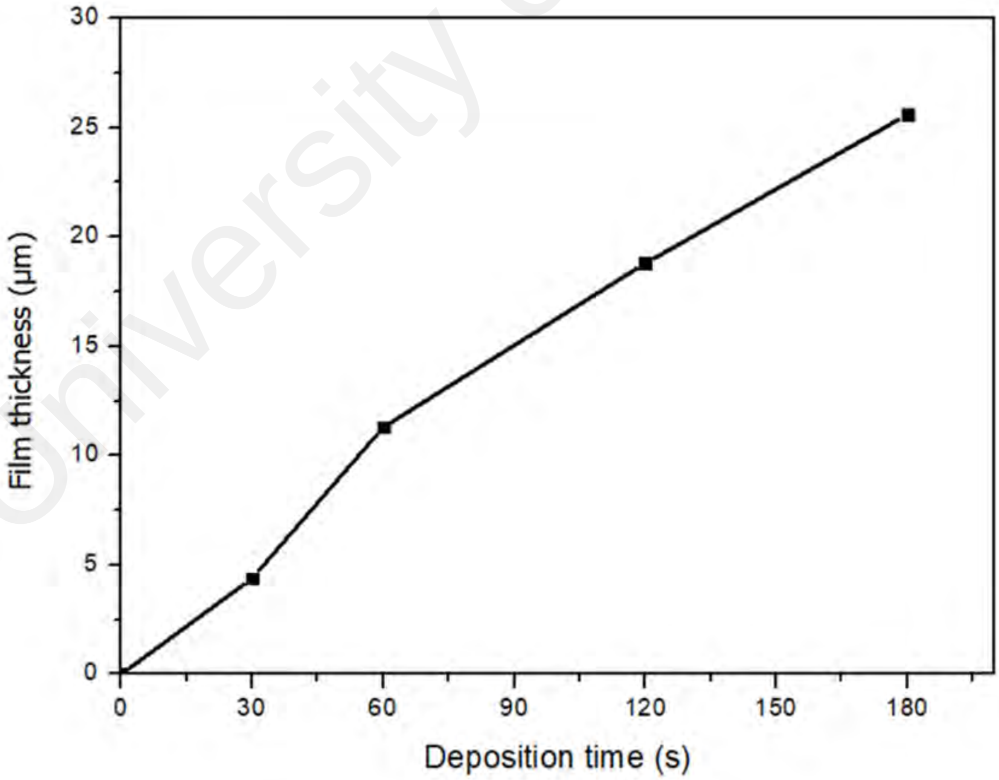

Figure 4.27: A graph of $SrTiO_3$ nanoparticles thin film thickness against the deposition time.

A rough surface of the thin film was observed for 180 s deposition in the FESEM micrograph in Figure 4.28. This indicates that the $SrTiO_3$ nanoparticle thin film that deposited for 180 s shows a bad surface uniformity compared to $SrTiO_3$ nanoparticle thin film that deposited by 120 s. This suggested that hole and voids in between interparticle may block the electron transferring. On the other hand, the $SrTiO_3$ nanoparticles thin film with high roughness surface might lead to high e^--h^+-pairs recombination, therefore lower down the efficiency.

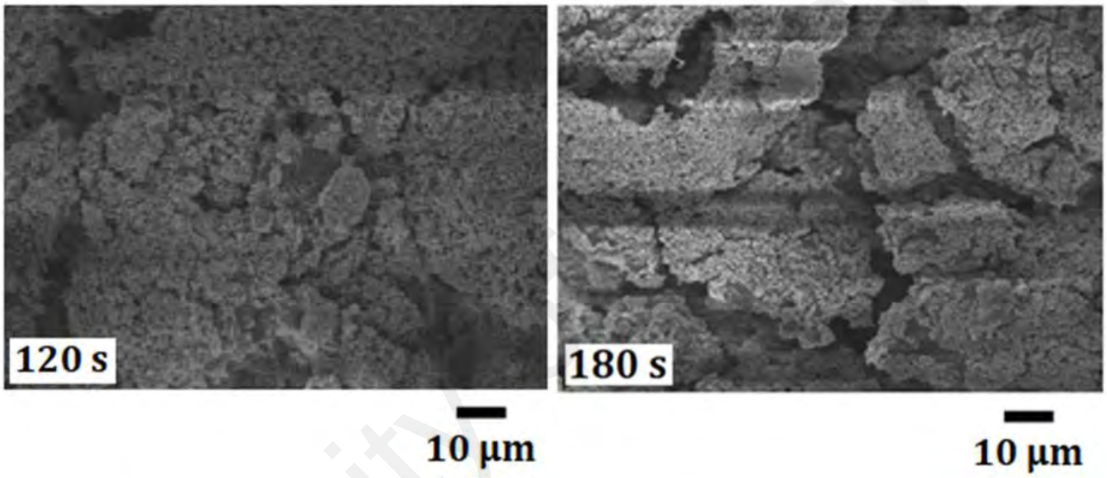

Figure 4.28: The FESEM micrographs of the $SrTiO_3$ nanoparticles thin film surface on FTO substrate by EPD.

One of the factors that have caused crack formation is due to the solvent selection. IPA was used for the EPD process in this study. It is an organic solvent that is volatile at room temperature and low boiling point. In addition, crack formation usually occurs before the sintering process and this would influence the adherence in between the $SrTiO_3$ nanoparticles and FTO substrate (Chang *et al.*, 2010). This concludes that a thicker STO nanoparticle thin film is likely to form more cracks and a rough surface. As a result, it can directly affect the performance of PEC water splitting and this explains the reason for the photocurrent to drop when the deposition time was prolonged to 180 s due to the non-uniform surface and many visible cracks were found. Besides that, it was reported that light scattering might occur on the thin film with a rough surface and it may lower down the PEC water splitting response (Osterloh, 2013). The STO nanoparticles photoelectrodes that were deposited by 120 s with a film thickness of 18.8 μm showed the best photocurrent density and this result is consistent with Hsiao *et al.* findings (Hsiao *et al.*, 2010).

4.2.3 PEC Water Splitting Performance

As the properties of $SrTiO_3$ nanoparticles was discussed and the parameters were optimised in the previous section. To understand the electron-transfer process in $SrTiO_3$ nanoparticles, transient measurements of photocurrent were conducted in a tri-electrode PEC cell under UV light irradiation. This section will discuss the PEC water splitting efficiencies in photocurrent response, EIS, PCE and the H_2 production rate of the optimised $SrTiO_3$ nanoparticles photoelectrode.

4.2.3.1 Photocurrent Response

The photocurrent-time curves of $SrTiO_3$ nanoparticles photoelectrode in different thickness were done and presented in Figure 4.29. Based on the graph, it shows a fast and uniform photocurrent response was observed for each on-and-off cycle under UV light irradiation, which can be attributed to the generation and transfer of electrons from the $SrTiO_3$ nanoparticles (Wang, Wong, Ho, Jiang, & Amal, 2017). When the light was switch off, the photocurrent immediately goes to zero. When the light was switch on again, the photocurrent comes back. Under UV light irradiation, all $SrTiO_3$ nanoparticles photoelectrode present a good reproducibility with photocurrent density. This might show all photoelectrodes are reversible in photoresponse and it is quite stable.

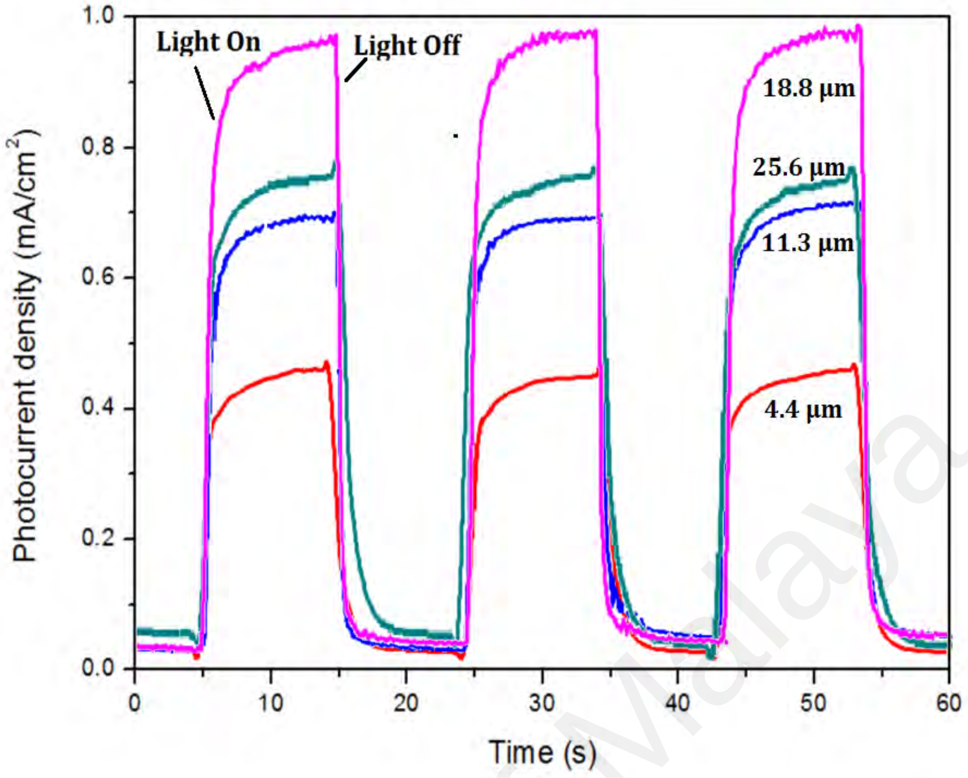

Figure 4.29: The photocurrent response for $SrTiO_3$ nanoparticles photoelectrode that fabricated in different thickness.

4.2.3.2 Electrochemical Impedance Spectroscopy (EIS)

EIS was measured for $SrTiO_3$ nanoparticles photoelectrodes in different thickness for the purpose of investigating on the photogenerated charge carrier separation efficiency and the process of charge transfer. Based on the graph shown in Figure 4.30, Nyquist semicircle for $SrTiO_3$ nanoparticles photoelectrode with the film thickness of 18.8 µm has the smallest diameter among samples, which indicates that film thickness of 18.8 µm has a smaller impedance value under UV light irradiation as a result of electrons and holes generation. This result is concordance with earlier published data (He *et al.*, 2016).

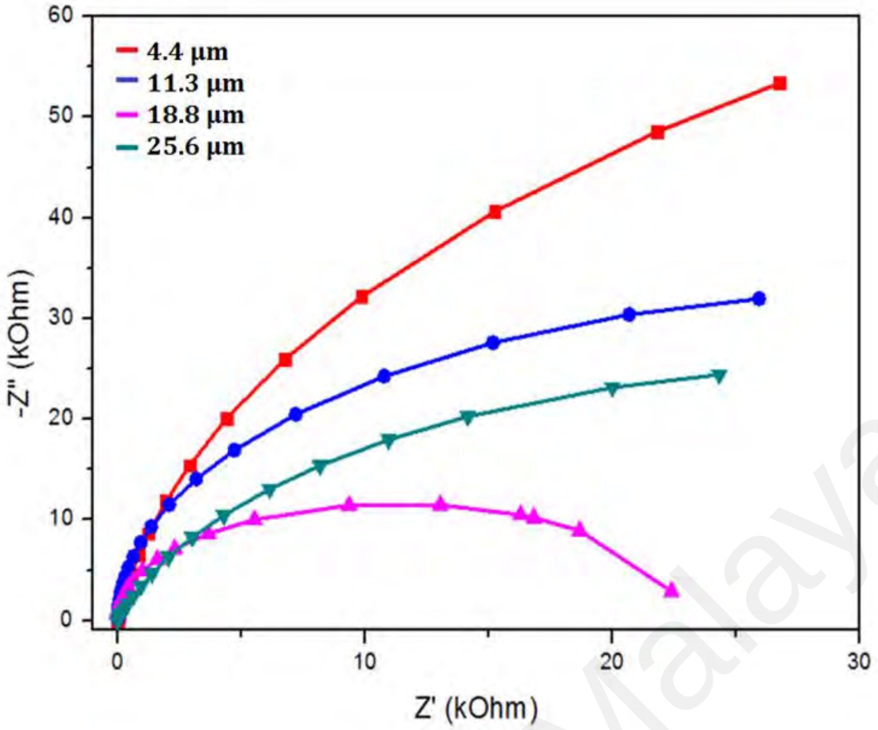

Figure 4.30: The electrochemical impedance spectroscopy (EIS) for SrTiO3 nanoparticles photoelectrode that fabricated in different thickness.

4.2.3.3 Photoconversion Efficiency (PCE)

The PCE, η is determined to predict quantitatively the correlation of light absorption. The photoconversion efficiency can be described as the ratio of its electric power output to the incoming light intensity that strikes the cell. Figure 4.31 shows the graph of PCE against potential (vs. Ag/AgCl), it was found $SrTiO_3$ nanoparticles photoelectrode with 18.8 µm gives the highest efficiency, which is 1.28 % whereas is about 0.62 % for 4.4 µm of film thickness.

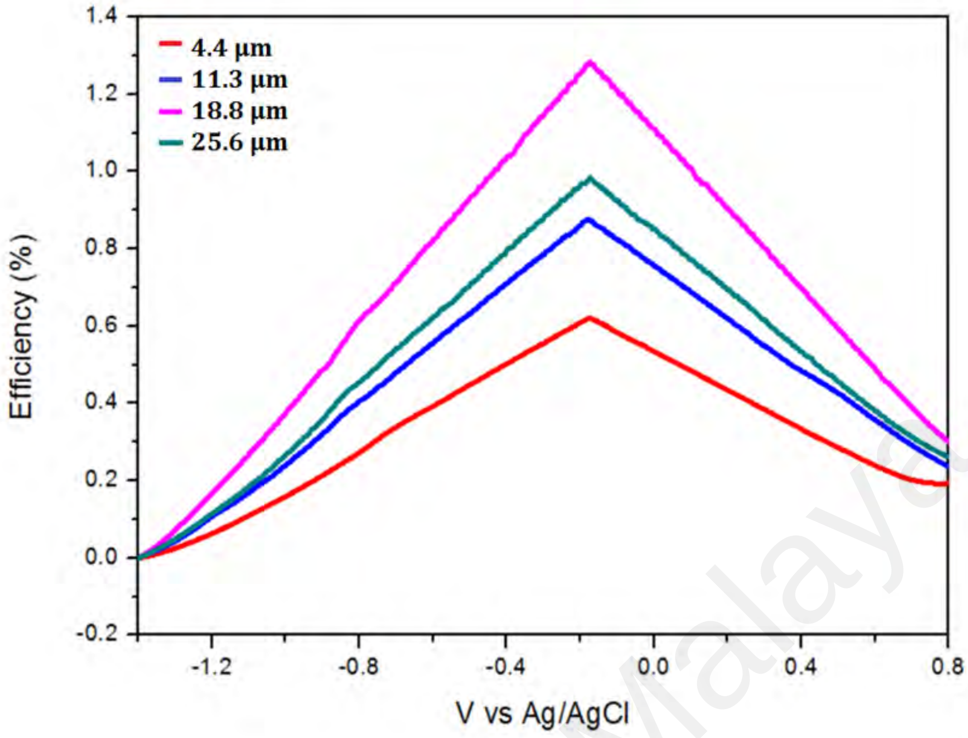

Figure 4.31: The calculated photoconversion efficiency (PCE) for $SrTiO_3$ nanoparticles photoelectrode that fabricated in different thickness.

4.2.3.4 Hydrogen Production

As the parameters studied, it was found that the optimum condition for the $SrTiO_3$ nanoparticles photoelectrode fabrication by using EPD method is 40 V and 120 s. For PEC water splitting, H_2 generation is an important application. The H_2 production rate from PEC water splitting was recorded and presented in Figure 4.32. The reading was recorded in every 10 min and a linear relation of H_2 production versus time was found. The H_2 production rate of $SrTiO_3$ nanoparticles as a photocatalyst was found to be 0.25 mL/cm^2/h. According to Figure 4.32, it was noticed that a slight drop in the H_2 production value for the 3rd cycle, which is only 0.23 mL of H_2 generated in an hour and the value was further dropped to 0.20 mL in 5th cycle. This might due to the $SrTiO_3$

nanoparticles sample on FTO glass substrate was peeling after soaked in a strong alkaline electrolyte for some time.

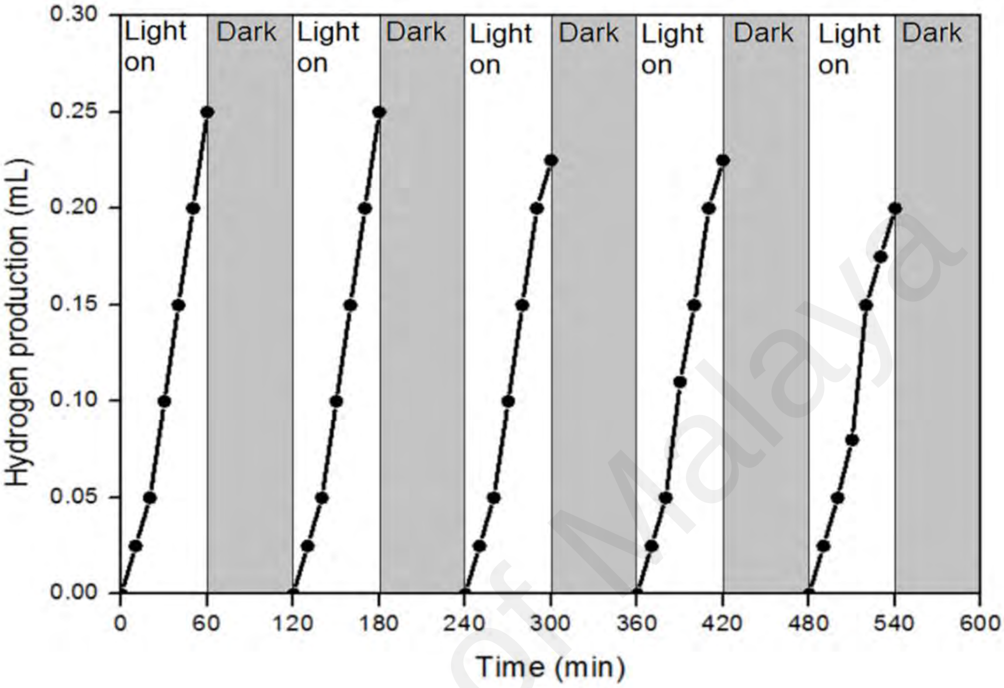

Figure 4.32: The hydrogen production of the optimised $SrTiO_3$ nanoparticles photoelectrode under UV light irradiation at 0.60 V vs. Ag/AgCl in five cycles.

4.3 Comparison between TiO_2 and $SrTiO_3$ nanoparticles

In this section, both water splitting efficiencies of nanocrystalline TiO_2 and $SrTiO_3$ nanoparticles was compared. According to section 4.1 and 4.2, the best photocurrent generated for nanocrystalline TiO_2 and $SrTiO_3$ nanoparticles was found to be 2.12 mA/cm^2 and 1.05 mA/cm^2, respectively (Figure 4.33). Therefore, the H_2 production rate of nanocrystalline TiO_2 (0.40 mL cm^{-2} h^{-1}) was 1.6 times better than that of $SrTiO_3$ nanoparticles (0.25 mL cm^{-2} h^{-1}).

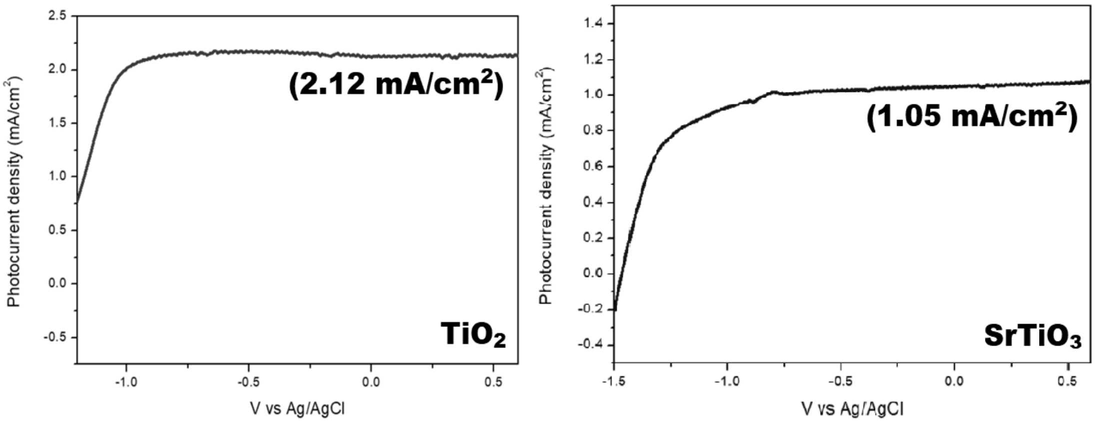

Figure 4.33: The j_p-V curve of nanocrystalline TiO_2 and $SrTiO_3$ nanoparticles at the optimised condition.

Since the chemical properties such as band hap and recombination rate did not vary significantly, the plausible explanation is based on the physical properties. It was noticeable the size of TiO_2 which is smaller than that of $SrTiO_3$. According to FESEM analysis (Figure 4.34), the diameter of TiO_2 nanoparticles is approximately 25 nm whereas for STO nanoparticles, it was found to be about 47 nm. Thus, the size of the nanoparticles might be directly affects the PEC water splitting efficiency.

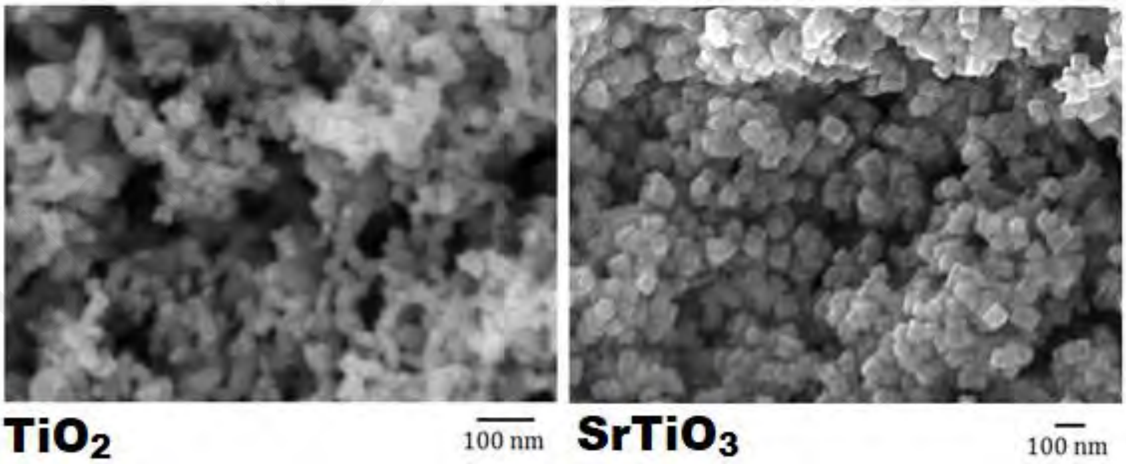

Figure 4.34: The FESEM micrographs of nanocrystalline TiO_2 and $SrTiO_3$ nanoparticles.

Secondly, the specific surface area of nanocrystalline TiO_2 (57.40 m^2/g) was 3.3 times greater than that of $SrTiO_3$ nanoparticles (17.00 m^2/g). Since the surface area of nanocrystalline TiO_2 is larger than $SrTiO_3$ nanoparticles, TiO_2 would have more active sites. As illustrated in Figure 4.35, TiO_2 could have more nanoparticles to attach to the FTO glass surface. In other words, more nanoparticles will be able to receive the light energy and thus more e^- and h^+ will be induced for PEC water splitting. As for $SrTiO_3$ thin film, a lesser number of nanoparticles attach on the surface of FTO glass due to large nanoparticles will occupy more space on the same dimension of FTO glass. Therefore, PEC water splitting of $SrTiO_3$ is relatively poor as compared to that of TiO_2.

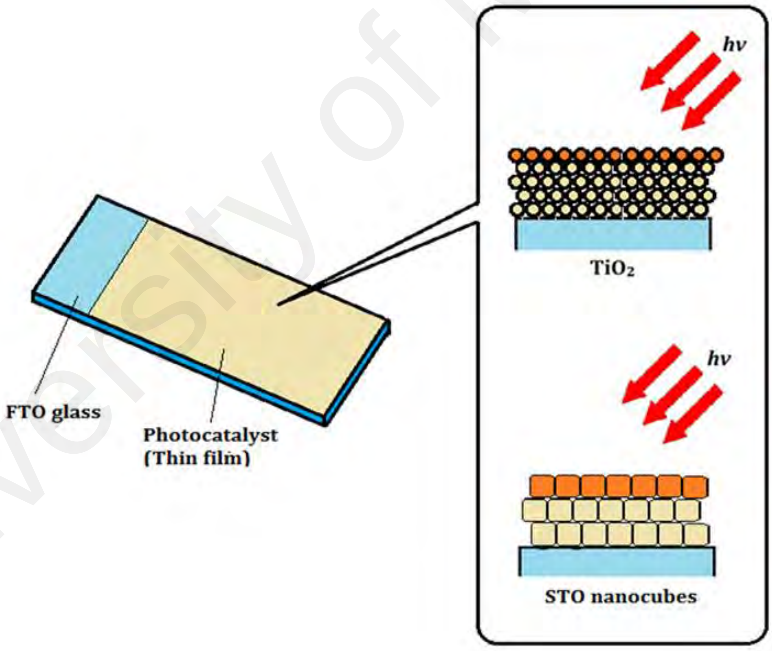

Figure 4.35: The schematic diagram of nanocrystalline TiO_2 and $SrTiO_3$ nanoparticles on FTO glass.

CHAPTER 5: CONCLUSION AND RECOMMENDATION

5.1 Conclusion

This research work was dedicated to use the thin film of nanocrystalline TiO_2 and $SrTiO_3$ nanoparticles as photoelectrode for the application of PEC water splitting process. In short, the objectives of the experiments were achieved. Initially, the formation of uniform, high crystallinity, and small particle size $SrTiO_3$ nanoparticles was successfully synthesised through one-step hydrothermal reaction. A comprehensive study was carried out to investigate the effect of EPD coating technique of TiO_2 and $SrTiO_3$ on FTO glass. Finally, the PEC water splitting system for H_2 production was successfully conducted using the TiO_2 and $SrTiO_3$ coated on FTO glass.

In the first stage of research study, the nanocrystalline TiO_2 was deposited as a thin film on FTO glass for the photoelectrode of PEC cells purpose. EPD technique was used to coat the photocatalyst. Four parameters namely colloidal stability, voltage, time, and post treatment temperature were tested. The conclusions attained in this research work are elaborated as follows:

- Based on the results obtained, concentration of Mg salt in the TiO_2 suspension was directly affects the ZP value. The ZP value shows the best when 10^{-4} M of Mg salt was added. Further increase the salt concentration would make the ZP value to fall due to compression of EDL and finally sedimentations occurred.
- The post-heat treatment parameter was studied. Based on the findings, TiO_2 thin film that undergoes 400 ^oC of heat treatment shows a better efficiency compared to as-annealed thin film. This is due to the heat treatment able to improve the necking, and the adherence of nanocrystalline TiO_2 and FTO substrate. Nonetheless, further increase the calcination temperature to 600 ^oC does not give

a better reading compared to 400 ^{o}C because the nanocrystalline was undergoes phase transformation.

- For deposition voltage parameter, TiO_2 thin film that deposited by 30 V generates the best photocurrent. However, when the deposition voltage was increased to 40 and 50 V, it makes the condition worse and this can be explained by the faster moving of particles when higher voltage is applied. The fast-moving particles do not have sufficient time to attach orderly on the FTO substrate and a loosely packed thin film was formed. The loosely pack thin film can affect the electron transport pathway.
- For deposition time parameter, TiO_2 thin film that deposited by 60 s produced the best photocurrent among samples. The deposition time can affect the film thickness and uniformity. The efficiency of TiO_2 thin film was dropped when the deposition time was extended to 120 s and 180 s. This is because the film that deposited by longer time will shows more cracks. These cracks possible to cause electron diffusion.
- The optimised EPD condition for nanocrystalline TiO_2 deposition was found to be 400 ^{o}C of heat treatment, 30 V and 60 s of deposition. The optimised TiO_2 photoelectrode was further tested with H_2 production and the PCE was calculated, which are 0.40 mL/cm^2/h and 2.49%, respectively. The TiO_2 photoelectrode can be reused for five times

In the second stage, the temperature parameter of hydrothermal reaction was determined in order to form a well-controlled morphology of $SrTiO_3$ nanoparticles. The conclusions attained from this research work are elaborated as follow:

- With the assist of instrument characterisations, formation of narrow nanoparticles size distribution, high crystallinity, small particle size and uniform particle shape of $SrTiO_3$ was achieved by hydrothermal reaction in alkaline (KOH) medium containing $Sr(OH)_2.8H_2O$ and TiO_2 precursors at 150 ^oC for 72 h. In the present study, the hydrothermal temperature can directly affects the morphology of $SrTiO_3$ nanoparticles. The $SrTiO_3$ nanoparticle was successfully formed in the range of temperature from 90 to 180 ^oC. Hydrothermal temperature below 90 ^oC could not form the $SrTiO_3$ nanoparticle completely.

- The hydrothermal synthesised $SrTiO_3$ nanoparticles in the range of 90 to 180 ^oC were fabricated as photoelectrode to test the PEC performance and the $SrTiO_3$ nanoparticle synthesised at 150 ^oC generates the best photocurrent due to uniform size, shape, and large specific surface area.
- The $SrTiO_3$ nanoparticle that synthesised at 150 ^oC was then further study by EPD parameters. The ZP value shows that adding 10^{-4} M of Mg salt in the $SrTiO_3$ suspension shows the highest colloidal stability and further increase the Mg salt concentration will bring down the ZP value due to EDL compression.
- The $SrTiO_3$ thin film that undergo 40 V of deposition voltage shows the best efficiency but further increase the voltage to 50 V did not produce a better photocurrent due to the $SrTiO_3$ nanoparticles arrangement on FTO substrate do not form a compactly packed thin film. The packing pattern of the thin film can affect the electron transport pathway.
- The $SrTiO_3$ thin film that undergo 120 s of deposition time shows the best efficiency but further extend the deposition time to 180 s did not produce a better photocurrent. This is because the thin film that deposition by 180 s shows a non-uniform thin film surface based on FESEM analysis. This non-uniform thin film surface possible to cause electron diffusion.
- As a result, $SrTiO_3$ thin film that deposited by 40 V and 120 s is optimised. This optimised $SrTiO_3$ photoelectrode was further undergo H_2 production testing and

the PCE was calculated, which is 0.25 mL/cm^2/h and 1.28%, respectively. The $SrTiO_3$ photoelectrode can be reused for five times.

Finally, both TiO_2 and $SrTiO_3$ photoelectrodes were compared in terms of PEC water splitting response. It was found that the H_2 production rate and PEC water splitting efficiency of TiO_2 coated on FTO glass using EPD technique was 0.40 mL/cm^2/h and 2.49%, respectively. This shows the EPD technique could be used to coat TiO_2 on FTO glass for PEC water splitting. Meanwhile, $SrTiO_3$ coated on FTO glass managed to produce up to 0.25 mL/cm^2/h (PCE of 1.28%) of H_2. This study also demonstrated that TiO_2 is about 1.6 times better efficiency than that of $SrTiO_3$. Therefore, it was proposed that this is due to (i) TiO_2 specific surface area is larger than $SrTiO_3$, and (ii) the particle size of TiO_2 is smaller than $SrTiO_3$.

5.2 Suggestions and Recommendations

In order to further develop the PEC water splitting H_2 generation technologies, several recommendations for future studies were proposed as follows:

- For further improve the STO nanoparticles efficiencies in PEC water splitting, some modification can be done (*e.g.* nanocomposites and ion doping are believed as a potential approach to further improve the surface charge carriers transfer rate and minimise the recombination rate).
- Meanwhile, the TiO_2 and STO thin film on FTO glass can only remain stable for five cycles in PEC water splitting H_2 generation. Therefore, further studies can be done (*e.g.* spin coating) so that able to extend the reusability and recyclability of photoelectrode thin film.

REFERENCES

Abanades, S., & Flamant, G. (2006). Thermochemical hydrogen production from a two-step solar-driven water-splitting cycle based on cerium oxides. *Solar Energy, 80*(12), 1611-1623.

Abdullah, H., Razali, M. Z., Shaari, S., & Taha, M. R. (2014). Enhancement of dye-sensitized solar cell efficiency using carbon nanotube/TiO2 nanocomposite thin films fabricated at various annealing temperatures. *Electronic Materials Letters, 10*(3), 611-619.

Abdullah, H., & Sorrell, C. (2008). TiO2 thick films by electrophoretic deposition. *Journal of the Australian Ceramic Society, 44*(2), 12-16.

Acar, C., & Dincer, I. (2014). Comparative assessment of hydrogen production methods from renewable and non-renewable sources. *International Journal of Hydrogen Energy, 39*(1), 1-12.

Ahn, K. H., Lee, Y.-H., Kim, M., Lee, H.-s., Youn, Y.-S., Kim, J., & Lee, Y.-W. (2013). Effects of surface area of titanium dioxide precursors on the hydrothermal synthesis of barium titanate by dissolution–precipitation. *Industrial & Engineering Chemistry Research, 52*(37), 13370-13376.

Amano, F., Ishinaga, E., & Yamakata, A. (2013). Effect of particle size on the photocatalytic activity of WO3 particles for water oxidation. *The Journal of Physical Chemistry C, 117*(44), 22584-22590.

Amiri, H., Mohammadi, I., & Afshar, A. (2016). Electrophoretic deposition of nano-zirconia coating on AZ91D magnesium alloy for bio-corrosion control purposes. *Surface and Coatings Technology*, *311*, 182-190.

Archer, M. D. (2002). Photovoltaics and photoelectrochemistry: similarities and differences. *Physica E: Low-dimensional Systems and Nanostructures, 14*(1), 61-64.

Ashiri, R., Ajami, R., & Moghtada, A. (2015). Sonochemical synthesis of SrTiO3 nanocrystals at low temperature. *International Journal of Applied Ceramic Technology, 12*(S2).

Azwar, M., Hussain, M., & Abdul-Wahab, A. (2014). Development of biohydrogen production by photobiological, fermentation and electrochemical processes: A review. *Renewable and Sustainable Energy Reviews, 31*, 158-173.

Banitaba, M. H., Davarani, S. S. H., & Pourahadi, A. (2013). Solid-phase microextraction of phthalate esters from aqueous media by electrophoretically deposited TiO 2 nanoparticles on a stainless steel fiber. *Journal of Chromatography A, 1283*, 1-8.

Bao, D., Yao, X., Wakiya, N., Shinozaki, K., & Mizutani, N. (2001). Band-gap energies of sol-gel-derived SrTiO 3 thin films. *Applied Physics Letters, 79*(23), 3767-3769.

Bard, A. J. (1982). Design of semiconductor photoelectrochemical systems for solar energy conversion. *The Journal of Physical Chemistry, 86*(2), 172-177.

Barreca, D., Carraro, G., Gombac, V., Gasparotto, A., Maccato, C., Fornasiero, P., & Tondello, E. (2011). Supported metal oxide nanosystems for hydrogen photogeneration: Quo vadis? *Advanced Functional Materials, 21*(14), 2611-2623.

Basu, R. N., Randall, C. A., & Mayo, M. J. (2001). Fabrication of dense zirconia electrolyte films for tubular solid oxide fuel cells by electrophoretic deposition. *Journal of the American Ceramic Society, 84*(1), 33-40.

Bellardita, M., Di Paola, A., Megna, B., & Palmisano, L. (2017). Absolute crystallinity and photocatalytic activity of brookite TiO 2 samples. *Applied Catalysis B: Environmental, 201*, 150-158.

Berbenni, V., Marini, A., & Bruni, G. (2001). Effect of mechanical activation on the preparation of SrTiO 3 and Sr 2 TiO 4 ceramics from the solid state system SrCO 3–TiO 2. *Journal of Alloys and Compounds, 329*(1), 230-238.

Besra, L., & Liu, M. (2007). A review on fundamentals and applications of electrophoretic deposition (EPD). *Progress in Materials Science, 52*(1), 1-61.

Bicakova, O., & Straka, P. (2010). The resources and methods of hydrogen production. *Acta Geodynamica et Geomaterialia, 7*(158), 175.

Binetti, E., El Koura, Z., Patel, N., Dashora, A., & Miotello, A. (2015). Rapid hydrogenation of amorphous TiO 2 to produce efficient H-doped anatase for photocatalytic water splitting. *Applied Catalysis A: General, 500*, 69-73.

Bisquert, J., Zaban, A., Greenshtein, M., & Mora-Seró, I. (2004). Determination of rate constants for charge transfer and the distribution of semiconductor and electrolyte electronic energy levels in dye-sensitized solar cells by open-circuit photovoltage decay method. *Journal of the American Chemical Society, 126(41),* 13550-13559.

Brattain, W., & Garrett, C. (1955). Experiments on the interface between germanium and an electrolyte. *Bell Labs Technical Journal, 34*(1), 129-176.

Burnside, S., Moser, J.-E., Brooks, K., Grätzel, M., & Cahen, D. (1999). Nanocrystalline mesoporous strontium titanate as photoelectrode material for photosensitized solar devices: increasing photovoltage through flatband potential engineering. *The Journal of Physical Chemistry B, 103*(43), 9328-9332.

Carneiro-da-Cunha, M. G., Cerqueira, M. A., Souza, B. W., Teixeira, J. A., & Vicente, A. A. (2011). Influence of concentration, ionic strength and pH on zeta potential and mean hydrodynamic diameter of edible polysaccharide solutions envisaged for multinanolayered films production. *Carbohydrate Polymers, 85*(3), 522-528.

Centi, G., & Perathoner, S. (2009). The role of nanostructure in improving the performance of electrodes for energy storage and conversion. *European Journal of Inorganic Chemistry, 2009*(26), 3851-3878.

Chang, H., Su, H.-T., Chen, W.-A., Huang, K. D., Chien, S.-H., Chen, S.-L., & Chen, C.-C. (2010). Fabrication of multilayer TiO 2 thin films for dye-sensitized solar cells with high conversion efficiency by electrophoresis deposition. *Solar Energy, 84*(1), 130-136.

Chen, D., Jiao, X., & Zhang, M. (2000). Hydrothermal synthesis of strontium titanate powders with nanometer size derived from different precursors. *Journal of the European Ceramic Society, 20*(9), 1261-1265.

Chen, F., & Liu, M. (2001). Preparation of yttria-stabilized zirconia (YSZ) films on La 0.85 Sr 0.15 MnO 3 (LSM) and LSM–YSZ substrates using an electrophoretic deposition (EPD) process. *Journal of the European Ceramic Society, 21*(2), 127-134.

Chen, L., Zhang, S., Wang, L., Xue, D., & Yin, S. (2009). Preparation and photocatalytic properties of strontium titanate powders via sol–gel process. *Journal of Crystal Growth, 311*(3), 746-748.

Chen, W., Liu, H., Li, X., Liu, S., Gao, L., Mao, Liu, Y. (2016). Polymerizable complex synthesis of SrTiO 3:(Cr/Ta) photocatalysts to improve photocatalytic water splitting activity under visible light. *Applied Catalysis B: Environmental, 192*, 145-151.

Chen, Y.-H., & Chen, Y.-D. (2011). Kinetic study of Cu (II) adsorption on nanosized BaTiO 3 and SrTiO 3 photocatalysts. *Journal of Hazardous Materials, 185*(1), 168-173.

Chiu, S.-C., & Li, Y.-Y. (2009). SiC nanowires in large quantities: Synthesis, band gap characterization, and photoluminescence properties. *Journal of Crystal Growth, 311*(4), 1036-1041.

Chong, S., & Yang, T. C.-K. (2017). Parametric Studies of Titania-Supported Gold-Catalyzed Oxidation of Carbon Monoxide. *Materials, 10*(7), 756.

Clavijo, S., Membrives, F., Quiroga, G., Boccaccini, A. R., & Santillán, M. J. (2016). Electrophoretic Deposition of Chitosan/Bioglass® and Chitosan/Bioglass®/TiO 2 Composite Coatings for Bioimplants. *Ceramics International, 42*(12), 14206-14213.

De Levie, R. (1999). The electrolysis of water. *Journal of Electroanalytical Chemistry, 476*(1), 92-93.

de Melo, J. V. S., & Trichês, G. (2012). Evaluation of the influence of environmental conditions on the efficiency of photocatalytic coatings in the degradation of nitrogen oxides (NOx). *Building and Environment, 49*, 117-123.

Deng, Q., Wei, M., Ding, X., Jiang, L., Ye, B., & Wei, K. (2008). Brookite-type TiO 2 nanotubes. *Chemical Communications,* (31), 3657-3659.

Di Paola, A., Bellardita, M., & Palmisano, L. (2013). Brookite, the least known TiO2 photocatalyst. *Catalysts, 3*(1), 36-73.

Esmaeilzadeh, J., Ghashghaie, S., Hosseinmardi, A., Marzbanrad, E., Raissi, B., & Zamani, C. (2014). Effect of dispersant on chain formation capability of TiO 2 nanoparticles under low frequency electric fields for NO 2 gas sensing applications. *Journal of the European Ceramic Society, 34*(5), 1201-1208.

Esswein, A. J., & Nocera, D. G. (2007). Hydrogen production by molecular photocatalysis. *Chemical reviews, 107*(10), 4022-4047.

Evans, P., & Sheel, D. (2007). Photoactive and antibacterial TiO 2 thin films on stainless steel. *Surface and Coatings Technology, 201*(22), 9319-9324.

Ewan, B., & Allen, R. (2005). A figure of merit assessment of the routes to hydrogen. *International Journal of Hydrogen Energy, 30*(8), 809-819.

Fakhouri, H., Pulpytel, J., Smith, W., Zolfaghari, A., Mortaheb, H. R., Meshkini, Arefi-Khonsari, F. (2014). Control of the visible and UV light water splitting and photocatalysis of nitrogen doped TiO 2 thin films deposited by reactive magnetron sputtering. *Applied Catalysis B: Environmental, 144*, 12-21.

Firouzdor, V., Brechtl, J., Hauch, B., Sridharan, K., & Allen, T. R. (2013). Electrophoretic deposition of diffusion barrier titanium oxide coatings for nuclear reactor cladding applications. *Applied Surface Science, 282*, 798-808.

Fritts, C. E. (1883). On a new form of selenium cell, and some electrical discoveries made by its use. *American Journal of Science,* (156), 465-472.

Fujishima, A., & Honda, K. (1972). Photolysis-decomposition of water at the surface of an irradiated semiconductor. *Nature, 238*(5385), 37-38.

Funk, J. E. (2001). Thermochemical hydrogen production: past and present. *International Journal of Hydrogen Energy, 26*(3), 185-190.

Ghicov, A., & Schmuki, P. (2009). Self-ordering electrochemistry: a review on growth and functionality of TiO 2 nanotubes and other self-aligned MO x structures. *Chemical Communications,* (20), 2791-2808.

Gorczyca, I., Suski, T., Christensen, N. E., & Svane, A. (2010). Limitations to band gap tuning in nitride semiconductor alloys. *Applied physics letters, 96*(10), 101907.

Grimes, Craig A. (2007). Synthesis and application of highly ordered arrays of TiO2 nanotubes. *Journal of Materials Chemistry*, *17*(15), 1451-1457.

Guo, L., Luo, H., Gao, J., Guo, L., & Yang, J. (2006). Microwave hydrothermal synthesis of barium titanate powders. *Materials Letters, 60*(24), 3011-3014.

Höhn, S., Braem, A., Neirinck, B., & Virtanen, S. (2017). Albumin coatings by alternating current electrophoretic deposition for improving corrosion resistance and bioactivity of titanium implants. *Materials Science and Engineering: C*, *73*, 798-807.

Hall, D. B., Underhill, P., & Torkelson, J. M. (1998). Spin coating of thin and ultrathin polymer films. *Polymer Engineering & Science, 38*(12), 2039-2045.

Ham, Y., Hisatomi, T., Goto, Y., Moriya, Y., Sakata, Y., Yamakata, A., . . . Domen, K. (2016). Flux-mediated doping of SrTiO 3 photocatalysts for efficient overall water splitting. *Journal of Materials Chemistry A, 4*(8), 3027-3033.

Hamaker, H. (1940). Formation of a deposit by electrophoresis. *Transactions of the Faraday Society, 35*, 279-287.

Han, C., Wang, Y., Lei, Y., Wang, B., Wu, N., Shi, Q., & Li, Q. (2015). In situ synthesis of graphitic-C3N4 nanosheet hybridized N-doped TiO2 nanofibers for efficient photocatalytic H2 production and degradation. *Nano Research, 8*(4), 1199-1209.

Hao, Y., Wang, X., & Li, L. (2014). Highly dispersed SrTiO 3 nanocubes from a rapid sol-precipitation method. *Nanoscale, 6*(14), 7940-7946.

He, G.-L., Zhong, Y.-H., Chen, M.-J., Li, X., Fang, Y.-P., & Xu, Y.-H. (2016). One-pot hydrothermal synthesis of SrTiO 3-reduced graphene oxide composites with enhanced photocatalytic activity for hydrogen production. *Journal of Molecular Catalysis A: Chemical, 423*, 70-76.

He, H. (2009). Comparison study of photocatalytic properties of SrTiO3 and TiO2 powders in decomposition of methyl orange. *International Journal of Environmental Research, 3*(1), 57-60.

Hosseini, S. E., & Wahid, M. A. (2016). Hydrogen production from renewable and sustainable energy resources: Promising green energy carrier for clean development. *Renewable and Sustainable Energy Reviews, 57*, 850-866.

Hou, D., Hu, X., Ho, W., Hu, P., & Huang, Y. (2015). Facile fabrication of porous Cr-doped SrTiO 3 nanotubes by electrospinning and their enhanced visible-light-driven photocatalytic properties. *Journal of Materials Chemistry A, 3*(7), 3935-3943.

Hsiao, P.-T., Tung, Y.-L., & Teng, H. (2010). Electron transport patterns in TiO2 nanocrystalline films of dye-sensitized solar cells. *The Journal of Physical Chemistry C, 114*(14), 6762-6769.

Hsiao, P. T., & Teng, H. (2009). Coordination of Ti4+ Sites in Nanocrystalline TiO2 Films Used for Photoinduced Electron Conduction: Influence of Nanoparticle Synthesis and Thermal Necking. *Journal of the American Ceramic Society, 92*(4), 888-893.

Huang, S.-T., Lee, W. W., Chang, J.-L., Huang, W.-S., Chou, S.-Y., & Chen, C.-C. (2014). Hydrothermal synthesis of SrTiO3 nanocubes: Characterization, photocatalytic activities, and degradation pathway. *Journal of the Taiwan Institute of Chemical Engineers, 45*(4), 1927-1936. doi: 10.1016/j.jtice.2014.02.003

Ikeda, S., Itani, T., Nango, K., & Matsumura, M. (2004). Overall water splitting on tungsten-based photocatalysts with defect pyrochlore structure. *Catalysis letters, 98*(4), 229-233.

Jafari, T., Moharreri, E., Amin, A. S., Miao, R., Song, W., & Suib, S. L. (2016). Photocatalytic water splitting—the untamed dream: a review of recent advances. *Molecules, 21*(7), 900.

Jang, J. T., Ko, D., Ahn, G., Yu, H. R., Jung, H., Kim, Y. S., Choi, S.-J. (2017). Effect of oxygen content of the LaAlO3 layer on the synaptic behavior of Pt/LaAlO3/Nb-doped SrTiO3 memristors for neuromorphic applications. *Solid-State Electronics*, *140*, 139-143.

Jayabal, P., Sasirekha, V., Mayandi, J., Jeganathan, K., & Ramakrishnan, V. (2014). A facile hydrothermal synthesis of SrTiO 3 for dye sensitized solar cell application. *Journal of Alloys and Compounds, 586*, 456-461.

Jeon, B. S., Hong, K. Y., Yoo, J. S., & Whang, K. W. (2000). Studies on the phosphor screen prepared by electrophoretic deposition for plasma display panel applications. *Journal of The Electrochemical Society, 147*(11), 4356-4362.

Jiang, Y., Zheng, B., Du, J., Liu, G., Guo, Y., & Xiao, D. (2013). Electrophoresis deposition of Ag nanoparticles on TiO 2 nanotube arrays electrode for hydrogen peroxide sensing. *Talanta, 112*, 129-135.

Joung, Y. S., & Buie, C. R. (2012). A hybrid method employing breakdown anodization and electrophoretic deposition for superhydrophilic surfaces. *The Journal of Physical Chemistry B, 117*(6), 1714-1723.

Kajale, D. D., Patil, G. E., Gaikwad, V. B., Shinde, S. D., Chavan, D. N., Pawar, N. K., . . . Jain, G. H. (2012). Synthesis of $SrTiO_3$ nanopowder by sol-gel hydrothermal method for gas sensing application. *International Journal on Smart Sensing and Intelligent Systems, 5*, 382-399.

Kalyani, V., Vasile, B. S., Ianculescu, A., Buscaglia, M. T., Buscaglia, V., & Nanni, P. (2012). Hydrothermal synthesis of SrTiO3 mesocrystals: single crystal to mesocrystal transformation induced by topochemical reactions. *Crystal Growth & Design, 12*(9), 4450-4456.

Karaphun, A., Hunpratub, S., & Swatsitang, E. (2014). Effect of annealing on magnetic properties of Fe-doped SrTiO 3 nanopowders prepared by hydrothermal method. *Microelectronic Engineering, 126*, 42-48.

Kaya, C., Kaya, F., Su, B., Thomas, B., & Boccaccini, A. (2005). Structural and functional thick ceramic coatings by electrophoretic deposition. *Surface and Coatings Technology, 191*(2), 303-310.

Kimijima, T., Kanie, K., Nakaya, M., & Muramatsu, A. (2014). Solvothermal synthesis of SrTiO 3 nanoparticles precisely controlled in surface crystal planes and their photocatalytic activity. *Applied Catalysis B: Environmental, 144*, 462-467.

Klaytae, T., Panthong, P., & Thountom, S. (2013). Preparation of nanocrystalline SrTiO 3 powder by sol–gel combustion method. *Ceramics International, 39*, S405-S408.

Kraeutler, B., & Bard, A. J. (1978). Heterogeneous photocatalytic preparation of supported catalysts. Photodeposition of platinum on titanium dioxide powder and other substrates. *Journal of the American Chemical Society, 100*(13), 4317-4318.

Kudo, A., & Miseki, Y. (2009). Heterogeneous photocatalyst materials for water splitting. *Chemical Society Reviews, 38*(1), 253-278.

Lee, D., Vu, H., Sun, H., Pham, T. L., Nguyen, D. T., Lee, J.-S., & Fisher, J. G. (2016). Growth of (Na 0.5 Bi 0.5) TiO 3-SrTiO 3 single crystals by solid state crystal growth. *Ceramics International, 42*(16), 18894-18901.

Lee, P.-w., Ong, S.-t., Hung, Y.-t., & Lee, S.-l. (2013). Photodegradation of Malachite Green by Immobilization of Titanium Dioxide on Glass Plates. *Asian Journal of Chemistry, 25*(2), 755.

Lee, S. W., Kwon, O. S., Han, J. H., & Hwang, C. S. (2008). Enhanced electrical properties of SrTiO3 thin films grown by atomic layer deposition at high temperature for dynamic random access memory applications. *Applied physics letters, 92*(22), 222903-222903.

Li, H.-L., Du, Z.-N., Wang, G.-L., & Zhang, Y.-C. (2010). Low temperature molten salt synthesis of SrTiO 3 submicron crystallites and nanocrystals in the eutectic NaCl–KCl. *Materials Letters, 64*(3), 431-434.

Linkous, C., Anderson, H., Kopitzke, R., & Nelson, G. (1998). Development of new proton exchange membrane electrolytes for water electrolysis at higher temperatures. *International Journal of Hydrogen Energy, 23*(7), 525-529.

Liou, Y.-J., Hsiao, P.-T., Chen, L.-C., Chu, Y.-Y., & Teng, H. (2011). Structure and electron-conducting ability of TiO2 films from electrophoretic deposition and paste-coating for dye-sensitized solar cells. *The Journal of Physical Chemistry C, 115*(51), 25580-25589.

Liu, J., Chen, G., Li, Z., & Zhang, Z. (2006). Electronic structure and visible light photocatalysis water splitting property of chromium-doped SrTiO 3. *Journal of Solid State Chemistry, 179*(12), 3704-3708.

Liu, S., Xiu, Z., Liu, J. a., Xu, F., Yu, W., Yu, J., & Feng, G. (2008). Combustion synthesis and characterization of perovskite SrTiO 3 nanopowders. *Journal of Alloys and Compounds, 457*(1), L12-L14.

Liu, Y., Xie, L., Li, Y., Yang, R., Qu, J., Li, Y., & Li, X. (2008). Synthesis and high photocatalytic hydrogen production of SrTiO3 nanoparticles from water splitting under UV irradiation. *Journal of Power Sources, 183*(2), 701-707. doi: 10.1016/j.jpowsour.2008.05.057

Low, F. W., Lai, C. W., & Hamid, S. B. A. (2017). Surface modification of reduced graphene oxide film by Ti ion implantation technique for high dye-sensitized solar cells performance. *Ceramics International, 43*(1), 625-633.

Luttrell, T., Halpegamage, S., Tao, J., Kramer, A., Sutter, E., & Batzill, M. (2014). Why is anatase a better photocatalyst than rutile?-Model studies on epitaxial TiO2 films. *Scientific reports, 4*, 4043.

Lyklema, J. (1977). Water at interfaces: a colloid-chemical approach. *Journal of colloid and Interface Science, 58*(2), 242-250.

Møller, J., Boldrin, A., & Christensen, T. H. (2009). Anaerobic digestion and digestate use: accounting of greenhouse gases and global warming contribution. *Waste Management & Research, 27*(8), 813-824.

Maggio, G., & Cacciola, G. (2012). When will oil, natural gas, and coal peak? *Fuel, 98*, 111-123.

Malghe, Y. (2010). Nanosized SrTiO3 powder from oxalate precursor microwave aided synthesis and thermal characterization. *Journal of Thermal Analysis and Calorimetry, 102*(3), 831-836.

Meda, L., & Abbondanza, L. (2013). Materials for Photo-Electrochemical Water Splitting. *Reviews in Advanced Sciences and Engineering, 2*(3), 200-207.

Mingyi, L., Bo, Y., Jingming, X., & Jing, C. (2008). Thermodynamic analysis of the efficiency of high-temperature steam electrolysis system for hydrogen production. *Journal of Power Sources, 177*(2), 493-499.

Molla, M. A. I., Tateishi, I., Furukawa, M., Katsumata, H., Suzuki, T., & Kaneco, S. (2017). Evaluation of Reaction Mechanism for Photocatalytic Degradation of Dye with Self-Sensitized TiO2 under Visible Light Irradiation. *Open Journal of Inorganic Non-metallic Materials, 7*(01), 1.

Momeni, M. M., & Ghayeb, Y. (2015a). Fabrication, characterization and photoelectrochemical behavior of Fe–TiO 2 nanotubes composite photoanodes for solar water splitting. *Journal of Electroanalytical Chemistry, 751*, 43-48.

Momeni, M. M., & Ghayeb, Y. (2015b). Photoelectrochemical water splitting on chromium-doped titanium dioxide nanotube photoanodes prepared by single-step anodizing. *Journal of Alloys and Compounds, 637*, 393-400. doi: 10.1016/j.jallcom.2015.02.137

Momeni, M. M., & Nazari, Z. (2016). Preparation of TiO 2 and WO 3–TiO 2 nanotubes decorated with PbO nanoparticles by chemical bath deposition process: a stable and efficient photo catalyst. *Ceramics International, 42*(7), 8691-8697.

Moniz, S. J., Shevlin, S. A., Martin, D. J., Guo, Z.-X., & Tang, J. (2015). Visible-light driven heterojunction photocatalysts for water splitting–a critical review. *Energy & Environmental Science, 8*(3), 731-759.

Moreira, M. L., Longo, V. M., Avansi Jr, W., Ferrer, M. M., Andres, J., Mastelaro, V. R., . . . Longo, E. (2012). Quantum mechanics insight into the microwave nucleation of SrTiO3 nanospheres. *The Journal of Physical Chemistry C, 116*(46), 24792-24808.

Mourão, H. A., Lopes, O. F., Ribeiro, C., & Mastelaro, V. R. (2015). Rapid hydrothermal synthesis and pH-dependent photocatalysis of strontium titanate microspheres. *Materials Science in Semiconductor Processing, 30*, 651-657.

Murphy, A. (2007). Band-gap determination from diffuse reflectance measurements of semiconductor films, and application to photoelectrochemical water-splitting. *Solar Energy Materials and Solar Cells, 91*(14), 1326-1337.

Nakashima, K., Kera, M., Fujii, I., & Wada, S. (2013). A new approach for the preparation of SrTiO 3 nanocubes. *Ceramics International, 39*(3), 3231-3234.

Navarro, R. M., Pena, M., & Fierro, J. (2007). Hydrogen production reactions from carbon feedstocks: fossil fuels and biomass. *Chemical Reviews, 107*(10), 3952-3991.

Negishi, H., Yanagishita, H., & Yokokawa, H. (2002). Electrophoretic deposition of solid oxide fuel cell material powders. *Proceedings of the electrochemical society on electrophoretic deposition: fundamentals and applications, 21*, 214-221.

Ni, M., Leung, D. Y., Leung, M. K., & Sumathy, K. (2006). An overview of hydrogen production from biomass. *Fuel Processing Technology, 87*(5), 461-472.

Ni, M., Leung, M. K., Leung, D. Y., & Sumathy, K. (2007). A review and recent developments in photocatalytic water-splitting using TiO2 for hydrogen production. *Renewable and Sustainable Energy Reviews, 11*(3), 401-425.

Nikolaidis, P., & Poullikkas, A. (2017). A comparative overview of hydrogen production processes. *Renewable and Sustainable Energy Reviews, 67*, 597-611.

Nikolic, V. M., Tasic, G. S., Maksic, A. D., Saponjic, D. P., Miulovic, S. M., & Kaninski, M. P. M. (2010). Raising efficiency of hydrogen generation from alkaline water electrolysis–energy saving. *International Journal of Hydrogen Energy, 35*(22), 12369-12373.

Nikolov, N., & Zeller, K. (2017). New insights on the physical nature of the atmospheric greenhouse effect deduced from an empirical planetary temperature model. *Environment Pollution and Climate Change, 1*(2), 112.

Noberi, C., Kaya, F., & Kaya, C. (2016). Synthesis, structure and characterization of hydrothermally synthesized Ag-TiO 2 nano-structures onto Ni filters using electrophoretic deposition. *Ceramics International, 42*(15), 17202-17209.

Odling, G., & Robertson, N. (2015). Why is anatase a better photocatalyst than rutile? The importance of free hydroxyl radicals. *ChemSusChem, 8*(11), 1838-1840.

Ogden, J. M., Steinbugler, M. M., & Kreutz, T. G. (1999). A comparison of hydrogen, methanol and gasoline as fuels for fuel cell vehicles: implications for vehicle design and infrastructure development. *Journal of Power Sources, 79*(2), 143-168.

Olah, G. A. (2005). Beyond oil and gas: the methanol economy. *Angewandte Chemie International Edition, 44*(18), 2636-2639.

Orhan, M. F., Dincer, I., & Rosen, M. A. (2008). Energy and exergy assessments of the hydrogen production step of a copper–chlorine thermochemical water splitting cycle driven by nuclear-based heat. *International Journal of Hydrogen Energy, 33*(22), 6456-6466.

Osterloh, F. E. (2013). Inorganic nanostructures for photoelectrochemical and photocatalytic water splitting. *Chemical Society Reviews, 42*(6), 2294-2320.

Park, J. H., Kim, J. S., & Park, J. M. (2013). Electrophoretic deposition of nano-ceramics for the photo-generated cathodic corrosion protection of steel substrates. *Surface and Coatings Technology, 236*, 172-181.

Park, N.-G., Van de Lagemaat, J., & Frank, A. (2000). Comparison of dye-sensitized rutile-and anatase-based TiO2 solar cells. *The Journal of Physical Chemistry B, 104*(38), 8989-8994.

Patil, N. B., Nimbalkar, A. R., & Patil, M. G. (2018). ZnO thin film prepared by a sol-gel spin coating technique for NO 2 detection. *Materials Science and Engineering: B, 227*, 53-60.

Perkins, C., & Weimer, A. W. (2004). Likely near-term solar-thermal water splitting technologies. *International Journal of Hydrogen Energy, 29*(15), 1587-1599.

Phoon, B. L., Pan, G.-T., Yang, T. C.-K., Lee, K. M., Lai, C. W., & Juan, J. C. (2017). Facile preparation of nanocrystalline TiO2 thin films using electrophoretic deposition for enhancing photoelectrochemical water splitting response. *Journal of Materials Science: Materials in Electronics, 28*(21), 16244-16253.

Pimentel, D., Bailey, O., Kim, P., Mullaney, E., Calabrese, J., Walman, Yao, X. (1999). Will limits of the Earth's resources control human numbers? *Environment, Development and Sustainability, 1*(1), 19-39.

Ramachandran, R., & Menon, R. K. (1998). An overview of industrial uses of hydrogen. *International Journal of Hydrogen Energy, 23*(7), 593-598.

Rao, C., & Dey, S. (2017). Solar thermochemical splitting of water to generate hydrogen. *Proceedings of the National Academy of Sciences*, 201700104.

Reber, J. F., & Meier, K. (1984). Photochemical production of hydrogen with zinc sulfide suspensions. *The Journal of Physical Chemistry, 88*(24), 5903-5913.

Rostrup-Nielsen, J. R. (2001). Conversion of hydrocarbons and alcohols for fuel cells. *Physical Chemistry Chemical Physics, 3*(3), 283-288.

Rostrup-Nielsen, J. R., Sehested, J., & Nørskov, J. K. (2002). Hydrogen and synthesis gas by steam-and C0 2 reforming. *Advances in Catalysis, 47*, 65-139.

Schrauzer, G., & Guth, T. (1977). Photocatalytic reactions. 1. Photolysis of water and photoreduction of nitrogen on titanium dioxide. *Journal of the American Chemical Society, 99*(22), 7189-7193.

Shane, M. J., Talbot, J. B., Schreiber, R. D., Ross, C. L., Sluzky, E., & Hesse, K. (1994). Electrophoretic deposition of phosphors: I. Conductivity and zeta potential measurements. *Journal of Colloid and Interface Science, 165*(2), 325-333.

Sharif, S. M., Bakar, N. F. A., & Naim, M. N. (2015). Deposition of fine iron oxide particles in tap water using electrophoretic deposition (EPD) technique. *Journal of Water Process Engineering, 7*, 123-130.

Sharma, D., Verma, A., Satsangi, V. R., Shrivastav, R., & Dass, S. (2014). Nanostructured SrTiO 3 thin films sensitized by Cu 2 O for photoelectrochemical hydrogen generation. *International Journal of Hydrogen Energy, 39*(9), 4189-4197.

Souza, A., Santos, G., Barra, B., Macedo Jr, W., Teixeira, S., Santos, Longo, E. (2012). Photoluminescence of SrTiO3: influence of particle size and morphology. *Crystal Growth & Design, 12*(11), 5671-5679.

Stassen, I., Styles, M., Grenci, G., Van Gorp, H., Vanderlinden, W., De Feyter, Ameloot, R. (2016). Chemical vapour deposition of zeolitic imidazolate framework thin films. *Nature Materials, 15*(3), 304-310.

Steinfeld, A. (2002). Solar hydrogen production via a two-step water-splitting thermochemical cycle based on Zn/ZnO redox reactions. *International Journal of Hydrogen Energy, 27*(6), 611-619.

Sudireddy, B. R., & Agersted, K. (2014). Sintering and Electrical Characterization of La and Nb Co-doped SrTiO3 Electrode Materials for Solid Oxide Cell Applications. *Fuel Cells, 14*(6), 961-965.

Sui, D., Yin, X., Dong, H., Qin, S., Chen, J., & Jiang, W. (2012). Photocatalytically reducing CO2 to methyl formate in methanol over Ag loaded SrTiO3 nanocrystal catalysts. *Catalysis letters, 142*(10), 1202-1210.

Sulaeman, U., Yin, S., & Sato, T. (2010). Solvothermal synthesis and photocatalytic properties of nitrogen-doped SrTiO 3 nanoparticles. *Journal of Nanomaterials, 2010*, 32.

Suttiponparnit, K., Jiang, J., Sahu, M., Suvachittanont, S., Charinpanitkul, T., & Biswas, P. (2011). Role of surface area, primary particle size, and crystal phase on titanium dioxide nanoparticle dispersion properties. *Nanoscale Research Letters, 6*(1), 27.

Townsend, T. K., Browning, N. D., & Osterloh, F. E. (2012). Nanoscale strontium titanate photocatalysts for overall water splitting. *Acs Nano, 6*(8), 7420-7426.

Trainer, M. (2001). Ferroelectricity: Measurement of the dielectric susceptibility of strontium titanate at low temperatures. *American Journal of Physics, 69*(9), 966-969.

Trasatti, S. (1999). Water electrolysis: who first? *Journal of Electroanalytical Chemistry, 476*(1), 90-91.

Travis, T. (1993). The Haber-Bosch process: exemplar of Twentieth century chemical industry. *Chemistry and Industry,* (15), 581-585.

Tsuchiya, T., Ochi, M., Higuchi, T., Terabe, K., & Aono, M. (2015). Effect of Ionic Conductivity on Response Speed of SrTiO3-Based All-Solid-State Electric-Double-Layer Transistor. *ACS applied materials & interfaces, 7*(22), 12254-12260.

Tsumura, T., Matsuoka, K., & Toyoda, M. (2010). Formation and annealing of BaTiO 3 and SrTiO 3 nanoparticles in KOH solution. *Journal of Materials Science & Technology, 26*(1), 33-38.

Turn, S., Kinoshita, C., Zhang, Z., Ishimura, D., & Zhou, J. (1998). An experimental investigation of hydrogen production from biomass gasification. *International Journal of Hydrogen Energy, 23*(8), 641-648.

Turner, J. A. (2004). Sustainable hydrogen production. *Science, 305*(5686), 972-974.

Umbach, F. (2010). Global energy security and the implications for the EU. *Energy Policy, 38*(3), 1229-1240.

Vázquez, A., Hernández-Uresti, D., & Obregón, S. (2016). Electrophoretic deposition of CdS coatings and their photocatalytic activities in the degradation of tetracycline antibiotic. *Applied Surface Science, 386*, 412-417.

Van Benthem, K., Elsässer, C., & French, R. (2001). Bulk electronic structure of SrTiO 3: experiment and theory. *Journal of Applied Physics, 90*(12), 6156-6164.

Vequizo, J. J. M., Matsunaga, H., Ishiku, T., Kamimura, S., Ohno, T., & Yamakata, A. (2017). Trapping-Induced Enhancement of Photocatalytic Activity on Brookite TiO2 Powders: Comparison with Anatase and Rutile TiO2 Powders. *ACS Catalysis, 7*(4), 2644-2651.

Verma, A., Samanta, S., Bakhshi, A., & Agnihotry, S. (2005). Effect of stabilizer on structural, optical and electrochemical properties of sol–gel derived spin coated TiO 2 films. *Solar Energy Materials and Solar Cells, 88*(1), 47-64.

Wang, F., Wong, R. J., Ho, J. H., Jiang, Y., & Amal, R. (2017). Sensitization of Pt/TiO2 Using Plasmonic Au Nanoparticles for Hydrogen Evolution under Visible-Light Irradiation. *ACS applied materials & interfaces, 9*(36), 30575-30582.

Wang, T. X., Liu, S. Z., & Chen, J. (2011). Molten salt synthesis of SrTiO 3 nanocrystals using nanocrystalline TiO 2 as a precursor. *Powder technology, 205*(1), 289-291.

Wang, W., Dong, J., Ye, X., Li, Y., Ma, Y., & Qi, L. (2016). Heterostructured TiO2 nanorod@ nanobowl arrays for efficient photoelectrochemical water splitting. *Small, 12*(11), 1469-1478.

Wang, Y., He, Y., Lai, Q., & Fan, M. (2014). Review of the progress in preparing nano TiO 2: An important environmental engineering material. *Journal of Environmental Sciences, 26*(11), 2139-2177.

Wei, X., Xu, G., Ren, Z., Xu, C., Weng, W., Shen, G., & Han, G. (2010). Single-Crystal-like Mesoporous SrTiO3 Spheres with Enhanced Photocatalytic Performance. *Journal of the American Ceramic Society, 93*(5), 1297-1305.

Wu, G., Li, P., Xu, D., Luo, B., Hong, Y., Shi, W., & Liu, C. (2015). Hydrothermal synthesis and visible-light-driven photocatalytic degradation for tetracycline of Mn-doped SrTiO3 nanocubes. *Applied Surface Science, 333*, 39-47. doi: 10.1016/j.apsusc.2015.02.008

Wu, J., Xu, H., & Yan, W. (2016). Photoelectrocatalytic degradation Rhodamine B over highly ordered TiO 2 nanotube arrays photoelectrode. *Applied Surface Science, 386*, 1-13.

Wu, Q., & Van De Krol, R. (2012). Selective photoreduction of nitric oxide to nitrogen by nanostructured TiO2 photocatalysts: role of oxygen vacancies and iron dopant. *Journal of the American Chemical Society, 134*(22), 9369-9375.

Wu, X., & Onuki, K. (2005). Thermochemical water splitting for hydrogen production utilizing nuclear heat from an HTGR. *Tsinghua Science & Technology, 10*(2), 270-276.

Xu, J., & Wang, Y. (2013). Preparation of CuInS 2 thin films by paste coating. *Materials Letters, 99*, 90-93.

Xu, M., Gao, Y., Moreno, E., Kunst, M., Muhler, M., Wang, Wöll, C. (2011). Topological features of electronic band structure and photochemistry: new insights from spectroscopic studies on single crystal titania substrates. *Physical Review Letter, 106*, 138302.

Xu, M., Lu, Y. N., Liu, Y. F., Shi, S. Z., & Fang, F. (2006). Synthesis of monosized strontium titanate particles with tailored morphologies. *Journal of the American Ceramic Society, 89*(12), 3631-3634.

Xu, Y., & Schoonen, M. A. (2000). The absolute energy positions of conduction and valence bands of selected semiconducting minerals. *American Mineralogist, 85*(3-4), 543-556.

Yang, S., Kou, H., Wang, J., Xue, H., & Han, H. (2010). Tunability of the band energetics of nanostructured SrTiO3 electrodes for dye-sensitized solar cells. *The Journal of Physical Chemistry C, 114*(9), 4245-4249.

Yang, Y., Lee, K., Kado, Y., & Schmuki, P. (2012). Nb-doping of TiO 2/SrTiO 3 nanotubular heterostructures for enhanced photocatalytic water splitting. *Electrochemistry Communications, 17*, 56-59.

Yildiz, B., & Kazimi, M. S. (2006). Efficiency of hydrogen production systems using alternative nuclear energy technologies. *International Journal of Hydrogen Energy, 31*(1), 77-92.

Yousefi, R., Jamali-Sheini, F., Cheraghizade, M., Khosravi-Gandomani, S., S aedi, A., Huang, N. M., . . . Azarang, M. (2015). Enhanced visible-light photocatalytic activity of strontium-doped zinc oxide nanoparticles. *Materials Science in Semiconductor Processing, 32*, 152-159.

Yu, H., Yan, S., Li, Z., Yu, T., & Zou, Z. (2012). Efficient visible-light-driven photocatalytic H2 production over Cr/N-codoped SrTiO3. *International Journal of Hydrogen Energy, 37*(17), 12120-12127. doi: 10.1016/j.ijhydene.2012.05.097

Yu, J. C., Zhang, L., Li, Q., Kwong, K. W., Xu, A.-W., & Lin, J. (2003). Sonochemical preparation of nanoporous composites of titanium oxide and size-tunable strontium titanate crystals. *Langmuir, 19*(18), 7673-7675.

Yuan, Y., Giri, G., Ayzner, A. L., Zoombelt, A. P., Mannsfeld, S. C., Chen, Bao, Z. (2014). Ultra-high mobility transparent organic thin film transistors grown by an off-centre spin-coating method. *Nature communications, 5*, 3005.

Yum, J.-H., Kim, S.-S., Kim, D.-Y., & Sung, Y.-E. (2005). Electrophoretically deposited TiO 2 photo-electrodes for use in flexible dye-sensitized solar cells. *Journal of Photochemistry and Photobiology A: Chemistry, 173*(1), 1-6.

Zarbov, M., Schuster, I., & Gal-Or, L. (2004). Methodology for selection of charging agents for electrophoretic deposition of ceramic particles. *Journal of Materials Science, 39*(3), 813-817.

Zeng, H., Lv, L., Fan, R., Wang, Y., Shen, X., Chen, J., & Li, J. (2017). Photocatalytic degradation of n-propanol wastewater by TiO2 combined with Fenton reactions. *Desalination and Water Treatment, 68*, 107-113.

Zeng, K., & Zhang, D. (2010). Recent progress in alkaline water electrolysis for hydrogen production and applications. *Progress in Energy and Combustion Science, 36*(3), 307-326.

Zhang, J., Huang, M., Yanagisawa, K., & Yao, S. (2015). NaCl–H 2 O-assisted preparation of SrTiO 3 nanoparticles by solid state reaction at low temperature. *Ceramics International, 41*(4), 5439-5444.

Zhang, J., Yu, J., Zhang, Y., Li, Q., & Gong, J. R. (2011). Visible light photocatalytic H2-production activity of CuS/ZnS porous nanosheets based on photoinduced interfacial charge transfer. *Nano Letters, 11*(11), 4774-4779.

Zhang, J., Zhou, P., Liu, J., & Yu, J. (2014). New understanding of the difference of photocatalytic activity among anatase, rutile and brookite TiO2. *Physical Chemistry Chemical Physics, 16*(38), 20382-20386.

Zhang, S., Liu, J., Han, Y., Chen, B., & Li, X. (2004). Formation mechanisms of SrTiO 3 nanoparticles under hydrothermal conditions. *Materials Science and Engineering: B, 110*(1), 11-17.

Zhang, Y., Zhong, L., & Duan, D. (2015). Single-step hydrothermal synthesis of strontium titanate nanoparticles from crystalline anatase titanium dioxide. *Ceramics International, 41*(10), 13516-13524.

Zhao, W., Zhao, W., Zhu, G., Lin, T., Xu, F., & Huang, F. (2015). Black strontium titanate nanocrystals of enhanced solar absorption for photocatalysis. *CrystEngComm, 17*(39), 7528-7534.

Zou, F., Jiang, Z., Qin, X., Zhao, Y., Jiang, L., Zhi, Edwards, P. P. (2012). Template-free synthesis of mesoporous N-doped SrTiO 3 perovskite with high visible-light-driven photocatalytic activity. *Chemical Communications, 48*(68), 8514-8516.

LIST OF PUBLICATIONS AND PAPERS PRESENTED

ISI-Cited Publications

1. **Bao Lee Phoon**, Guan-Ting Pan, Thomas CK Yang, Kian Mun Lee, Chin Wei Lai, Joon Ching Juan. (2017). Facile preparation for nanocrystalline TiO_2 thin films using electrophoretic depositon for enhancing photoelectrochemical water splitting response. *Journal of Materials Science: Materials in Electronics*, 21(28), 16244-16253. *DOI:10.1007/s10854-017-7528-8*

2. **Bao Lee Phoon**, Chin Wei Lai, Guan-Ting Pan, Thomas CK Yang, Joon Ching Juan. (2018). One-pot hydrothermal synthesis of strontium titanate nanoparticles photoelectrode using electrophoretic deposition for enhancing photoelectrochemical water splitting. *Ceramics International*, 44(8), 9923-9933. *DOI:10.1016/j.ceramint.2018.03.017*

3. **Bao Lee Phoon**, Chin Wei Lai, Joon Ching Juan. (2018). A review and recent developments of strontium titanate for PEC water splitting. **(In preparation)**

Conference Proceedings

1. **Bao Lee Phoon**, Joon Ching Juan, Chin Wei Lai, & Sharifah Bee Abd Hamid. (2016, December 12-13). Fabrication of nanocrystalline TiO_2 thin films by electrophoretic deposition technique for photoelectrochemical (PEC) water splitting application. Paper presented at the International Conference on Substantial Environmental Engineering and Renewable Energy (SEERE-2016), Phuket, Thailand.

2. **Bao Lee Phoon**, Guan-Ting Pan, Thomas CK Yang, Chin Wei Lai, & Joon Ching Juan. (2017, July 25-26). Hydrothermal synthesis of strontium titanate nanoparticles for photoelectrochemical (PEC) water splitting application. Paper presented at 4th Postgraduate Colloquium for Environmental Research 2017 (POCER 2017), Swiss Garden Hotel, Malacca, Malaysia.